



Unraveling Heterogeneity in X-ray Single Particle Imaging

Dissertation

zur Erlangung des Doktorgrades an der Fakultät für Mathematik, Informatik und Naturwissenschaften Fachbereich Physik der Universität Hamburg

vorgelegt von

Abhishek Mall

Hamburg 2025

Gutachter der Dissertation: Prof. Dr. Henry Chapman

Dr. Kartik Ayyer

Zusammensetzung der Prüfungskommission: Prof. Dr. Dorota Koziej

Prof. Dr. Arwen Pearson

Dr. Marianna Rossi

Prof. Dr. Henry Chapman

Dr. Kartik Ayyer

Vorsitzende/r der Prüfungskommission: Prof. Dr. Dorota Koziej

Datum der Disputation: 13 October 2025

Vorsitzender Fach-Promotionsausschuss PHYSIK: Prof. Dr. Wolfgang J. Parak

Leiter des Fachbereichs PHYSIK: Prof. Dr. Markus Drescher

Dekan der Fakultät MIN: Prof. Dr.-Ing. Norbert Ritter

Declaration on Oath

I hereby declare and affirm that this doctoral dissertation is my own work and that I have not used any aids and sources other than those indicated.

If electronic resources based on generative artificial intelligence (gAI) were used in the course of writing this dissertation, I confirm that my own work was the main and value-adding contribution and that complete documentation of all resources used is available in accordance with good scientific practice. I am responsible for any erroneous or distorted content, incorrect references, violations of data protection and copyright law or plagiarism that may have been generated by the gAI.

Abhishek Mall

June 24, 2025

Hamburg, Germany

Dedicated to : Papa, Mummy, Sis and my younger self

Acknowledgments

My dissertation represents not only years of dedication, hard work, and the pursuit of learning but also stands as an example of the unwavering support, guidance, belief, and encouragement of many amazing individuals, including my family, friends, colleagues — and to some extent, myself. I am deeply grateful for their contributions, whether direct or indirect, without which this dissertation would not have been possible.

First and foremost, I extend my deepest appreciation to my supervisor, Dr. Kartik Ayyer, who provided me with this great opportunity — an adventure that transformed me into a better researcher. His mentorship helped me develop better scientific thinking, introducing me to the world of cool ideas and having an intriguing perspective on doing science. I am thankful for his expertise, patience, and invaluable mentorship throughout my dissertation journey. His insightful feedback and open-door policy — welcome to all kinds of questions, big or small — helped guide me through moments of doubt and inspired me to learn and grow in my research.

I am also grateful to Prof. Henry Chapman for his thoughtful critiques, suggestions, and time during my annual PhD evaluations, as well as his contributions through feedback and suggestions toward the publication of research articles that form part of this dissertation. His input has significantly enriched the work.

I would also like to thank my colleagues — Dr. Yulong Zuhang, Dr. Parichita Mazumder, Tamme Wollweber, Dr. Shen Zhou, Dr. Alba M. Jumbo Nogales, and Dr. Omkar Rambadey — who were like a work family to me. They made the many hours in the office enjoyable, filled with fun and chatter, and countless coffee-fueled discussions.

I also want to thank my friends who made life in Hamburg wonderful and life outside of Hamburg adventurous. I am especially grateful to Mukhtar Singh, Shubham Sharma, and Yogesh Mahor for the many cooking nights, hangouts, travels, and conversations that kept humor and laughter consistent in the midst of everyday routine.

A heartfelt thank you goes to Michael and Claudia for welcoming me when I first arrived in Hamburg and giving me a place to stay — a home away from home. Living with them for over a year created unforgettable memories and made them

feel like my host parents. Michael, thank you for all the chats and long discussions about anything and everything. Claudia, thank you for taking care of me and helping me whenever I called for. I would also like to thank Lakhan, who helped me learn and navigate the ways of living in Germany.

I am deeply grateful to my Grand Uncle, Prof. Dr. Dr. Ram Adhar Mall, who has always been an inspiration and a role model for how to approach life and its lessons. Though I met you later in life, your belief in me and your unwavering support for my goals and dreams have continuously motivated me and brought joy to my journey and decisions. I also want to thank Christine for taking care of you and for the warmth and love she has shown me during my visits. Celebrating Christmas with both of you has always been special.

And most importantly — I want to thank my partner, Jule. Thank you for supporting my every dream, decision, and stubborn moment. I cannot fully express how thankful and grateful I am to have you in my life and throughout this dissertation journey. I can't wait to spend an eternity with you. An extended thanks to Jule's family for their affection and caring.

And finally, I want to thank my family. Papa and Mummy — thank you for your endless love, affection, and unwavering support from the very beginning. I could not be who I am today without you. Every accolade, every moment of applause, every achievement and success in my life is dedicated to both of you. To my sister, Smita — you have been the friend I always needed at home. I am truly grateful to have you as my sister and I am proud to be your brother.

And last but not least, I want to thank myself for believing in me. With heartfelt thanks,

Abhishek Mall

Abstract

This dissertation presents methods to improve X-ray single-particle imaging (SPI) for recovering detailed 3D structures of nanoscale biomolecules — such as viruses and proteins — at synchrotrons and X-ray free-electron laser sources (XFELs). Specifically, it addresses challenges posed by structural heterogeneity in the sample of interest and high background noise akin to experiments, both of which significantly limit the achievable near-atomic resolution.

Chapter 1 provides an overview and historical context of SPI. Chapter 2 briefly introduces fundamental concepts. In Chapter 3, 4, 5 and 6, developed methods are discussed in detail. Chapter 7 summarizes the findings and outlines future directions. Additional technical information is included in the Supplementary and Appendix chapters.

In Chapter 3, a way of using SPI and combination of machine learning techniques is discussed to observe structural transition in viral capsids such as MS2 bacteriophages after aerosolization. The method classifies hundreds of thousands of single particle diffraction patterns to learn the structural landscape of the capsid morphology as a function of time spent in the aerosol phase. A previously unreported compact conformation as well as intermediate structures were discovered suggesting a likely protective mechanism in viral capsid, leading to the large observed morphology change. These findings demonstrate the power of SPI and machine learning methods in unraveling heterogeneity and studying biomolecular structural dynamics.

Chapter 4 describes an improved reconstruction algorithm for holographic-SPI at XFELs. A maximum likelihood estimation algorithm is introduced, offering better scalability and enabling finer sampling of latent parameters to achieve higher resolutions and significantly improved performance in low-signal conditions. This method employs experimental configuration where strong scattering gold nanospheres are placed in close proximity to the target object, as holographic reference objects. This approach enhances the quality of the interference patterns. Furthermore, holographic-SPI enables structural variations within the target particle to be averaged directly in real space, facilitating the recovery of an average structure across conformational states. This leads to greater robustness in handling structural heterogeneity compared to conventional SPI. With these computational advancements,

holographic-SPI demonstrates the potential to achieve sub-nanometer resolution in biomolecular imaging.

Chapter 5 builds upon previous work by introducing an experimental configuration for holographic-SPI to address challenges posed by high background noise and radiation damage resulting from prolonged exposures at synchrotrons. The method involves placing a strongly scattering 2D crystal lattice as reference object near the target object. The holographic enhancement provided by the lattice Bragg peaks enables structure retrieval even when background levels are up to 10⁵ times higher than the target object signal. This method significantly improves the signal-to-background ratio, supports practical fixed-target sample delivery, and enables high-resolution imaging under near-native conditions at synchrotron sources.

To explore and validate holographic-SPI ideas further, Chapter 6 presents two synchrotron-based experiments investigating lattice-enhanced holographic-SPI. Two types of 2D crystal reference structures were employed: (i) a self-assembled monolayer of polystyrene nanospheres and (ii) lithographically patterned crossed gratings. By leveraging coherent interference between the structured reference and the sample, modulations in Bragg peak intensities were analyzed. Although challenges remain, particularly in fabricating high-quality low-variation references, preliminary results demonstrate the feasibility of this approach and suggest promising avenues for further optimization.

The Appendix provides details on the developed code associated with Chapter 3 and 5. Supplementary material includes additional data and analysis relevant to Chapter 3.

Kurzfassung

Diese Dissertation stellt Methoden zur Verbesserung der Röntgen-Single-Particle-Imaging (SPI) vor, um detaillierte 3D-Strukturen nanoskaliger Biomoleküle – wie Viren und Proteinen – an Synchrotronen und Röntgenfreie-Elektronen-Laser-Quellen (XFELs) zu rekonstruieren. Insbesondere werden Herausforderungen behandelt, die durch strukturelle Heterogenität in der Probe sowie starkes Hintergrundrauschen, ähnlich wie in realen Experimenten, entstehen – beides Faktoren, die die erreichbare nahe-atomare Auflösung erheblich einschränken.

Kapitel 1 bietet einen Überblick und den historischen Kontext von SPI. Kapitel 2 führt kurz in grundlegende Konzepte ein. In Kapitel 3, 4, 5 und 6 werden die entwickelten Methoden ausführlich diskutiert. Kapitel 7 fasst die Ergebnisse zusammen und skizziert zukünftige Richtungen. Zusätzliche technische Informationen sind in den Kapiteln Supplement und Anhang enthalten.

In Kapitel 3 wird ein Ansatz beschrieben, bei dem SPI mit Methoden des maschinellen Lernens kombiniert wird, um strukturelle Übergänge in viralen Kapsiden – wie denen von MS2-Bakteriophagen – nach der Aerosolisierung zu beobachten. Die Methode klassifiziert Hunderttausende von Einzelpartikelbeugungsmustern, um die Strukturlandschaft der Kapsidmorphologie in Abhängigkeit von der Verweildauer in der Aerosolphase zu erfassen. Eine zuvor nicht berichtete kompakte Konformation sowie Zwischenstrukturen wurden entdeckt, was auf einen wahrscheinlichen Schutzmechanismus im viralen Kapsid hinweist und die beobachtete starke Veränderung der Morphologie erklärt. Diese Ergebnisse zeigen die Leistungsfähigkeit von SPI und Methoden des maschinellen Lernens zur Aufklärung von Heterogenität und zur Untersuchung biomolekularer Strukturdynamiken.

Kapitel 4 beschreibt einen verbesserten Rekonstruktionsalgorithmus für holographisches SPI an XFELs. Ein Maximum-Likelihood-Schätzalgorithmus wird vorgestellt, der eine bessere Skalierbarkeit bietet und eine feinere Abtastung latenter Parameter ermöglicht, um höhere Auflösungen und eine deutlich bessere Leistung bei schwachen Signalen zu erreichen. Diese Methode nutzt eine experimentelle Konfiguration, bei der stark streuende Goldnanosphären als holographische Referenzobjekte in unmittelbarer Nähe zum Zielobjekt platziert werden. Dieser Ansatz verbessert die Qualität der Interferenzmuster. Darüber hinaus ermöglicht holographisches SPI eine Mittelung struktureller Variationen innerhalb des Zielpartikels

direkt im Realraum, wodurch eine durchschnittliche Struktur über Konformationszustände hinweg wiederhergestellt werden kann. Dies führt zu einer höheren Robustheit im Umgang mit struktureller Heterogenität im Vergleich zu herkömmlichem SPI. Mit diesen rechnergestützten Fortschritten zeigt holographisches SPI das Potenzial, subnanometergenaue Auflösungen in der biomolekularen Bildgebung zu erreichen.

Kapitel 5 baut auf früheren Arbeiten auf und stellt eine experimentelle Konfiguration für holographisches SPI vor, die Herausforderungen wie hohes Hintergrundrauschen und Strahlenschäden durch längere Belichtungen an Synchrotronen adressiert. Die Methode beinhaltet das Platzieren eines stark streuenden 2D-Kristallgitters als Referenzobjekt in der Nähe des Zielobjekts. Die holographische Verstärkung durch die Gitter-Bragg-Peaks ermöglicht die Strukturrekonstruktion selbst bei Hintergrundniveaus, die bis zu 10⁵-mal höher sind als das Signal des Zielobjekts. Diese Methode verbessert das Signal-zu-Hintergrund-Verhältnis erheblich, unterstützt eine praktikable Probenzufuhr im Festkörpermodus und ermöglicht hochauflösende Bildgebung unter nahezu nativen Bedingungen an Synchrotronen.

Zur weiteren Untersuchung und Validierung der holographischen SPI-Ideen beschreibt Kapitel 6 zwei synchrotronbasierte Experimente zur Untersuchung des gitterverstärkten holographischen SPI. Es wurden zwei Arten von 2D-Kristall-Referenzstrukturen verwendet: (i) eine selbstorganisierte Monoschicht aus Polystyrol-Nanosphären und (ii) lithografisch gefertigte gekreuzte Gitterstrukturen. Durch Nutzung der kohärenten Interferenz zwischen der strukturierten Referenz und der Probe wurden Modulationen in den Intensitäten der Bragg-Peaks analysiert. Obwohl weiterhin Herausforderungen bestehen – insbesondere bei der Herstellung hochwertiger, variantenarmer Referenzen – zeigen erste Ergebnisse die Machbarkeit dieses Ansatzes und deuten auf vielversprechende Möglichkeiten zur weiteren Optimierung hin.

Der Anhang enthält Details zum entwickelten Code, der in Kapitel 3 und 5 beschrieben wird. Zusätzliches Datenmaterial und Analysen zu Kapitel 3 sind im Supplement enthalten.

Preface

When a kid is born, it is like the start of this amazing adventure, full of little steps that change them bit by bit. For the first six months or so, babies see the world with limited color-vision, poor contrast till now! Study suggests their eyes and brains are still figuring things out, and color vision sensitivity kicks in slowly [1]. Then, around age one to two, kids start getting what choices are all about. Like when they grab the red toy instead of the blue one - it is their way of saying, "Hey, I have got opinions now!" Research shows this is when they start understanding they can pick between things, showcasing self-awareness [2]. Every stage, from those shaky first steps to yelling "no" at the top of their lungs, is them growing into who they are.

Honestly, my PhD journey over the last five years felt a lot like that. When I started, I was clueless on the starting line of an adventure - like a baby squinting at a blurry, faded world. I could barely make sense of the big ideas in my field. But little by little, things got clearer, just like how colors pop into a baby's life. By year two or three, I was picking my own path - like a toddler choosing their favorite snack; taking time to build skills and confidence in something new [3]. I started seeing the cool, tricky stuff in my research that was not obvious at first glance.

It was not always smooth sailing, though. Some days, I felt stuck, like a kid throwing a fit because they can not say what they mean. But then there were these "aha!" moments - like when a kid spots a rainbow and can not stop staring. Over these five years, I have dug into some pretty neat, not-so-simple ideas in my field. It took patience, a ton of coffee, and being okay with messing up sometimes. This dissertation is the summation of all that. It is not just about the research — it is about how I grew along the way. I am like that five-year-old now, excited and ready for what is next, knowing there is still so much more to figure out and grow into.

Contents

ostrac	et	•	vii
ırzfas	ssung		ix
eface			xi
st of I	Publicat	tions	ΧV
st of (Open-So	ource Codes x	ix
st of I	Figures	XXV	iii
st of T	Fables	XX	ix
Intr	oductio	n	1
Basi	c Conce	epts	4
2.1	Biomo	olecules	4
	2.1.1	Structure and Function	5
	2.1.2	Heterogeneity and Conformational Dynamics	5
2.2	X-ray	Sources	6
	2.2.1	Synchrotrons	7
	2.2.2	X-ray Free-Electron Lasers (XFELs)	7
2.3	Nanos	cale Imaging Techniques	8
	2.3.1	X-ray Crystallography	9
	2.3.2	Cryo-Electron Microscopy (Cryo-EM)	9
	2.3.3	X-ray Single-Particle Imaging (SPI)	11
	2.3.4	Fourier Transform Holography	11
	2.3.5	Ptychography	12
	eface st of I st of I Intro Basi 2.1	st of Publicates st of Open-So st of Figures st of Tables Introduction Basic Conce 2.1 Biomo 2.1.1 2.1.2 2.2 X-ray 8 2.2.1 2.2.2 2.3 Nanos 2.3.1 2.3.2 2.3.3 2.3.4	eface st of Publications st of Open-Source Codes xx st of Figures xxx Introduction Basic Concepts 2.1 Biomolecules 2.1.1 Structure and Function 2.1.2 Heterogeneity and Conformational Dynamics 2.2 X-ray Sources 2.2.1 Synchrotrons 2.2.2 X-ray Free-Electron Lasers (XFELs) 2.3 Nanoscale Imaging Techniques 2.3.1 X-ray Crystallography 2.3.2 Cryo-Electron Microscopy (Cryo-EM) 2.3.3 X-ray Single-Particle Imaging (SPI) 2.3.4 Fourier Transform Holography

		2.3.6 Holographic SPI	13
	2.4	Reconstruction Algorithm	14
		2.4.1 Latent Variables and Forward Model	15
		2.4.2 Expectation-Maximization-Compression (EMC)	15
		2.4.3 Phase Retrieval	16
		2.4.4 Resolution	16
	2.5	Machine Learning	17
3	SPI	of Dehydrating Viral Capsids	19
	3.1	Abstract	19
	3.2	Introduction	20
	3.3	X-ray SPI Experiment	23
	3.4	Heterogeneity Analysis Workflow	24
	3.5	Structural landscape	27
	3.6	Proposed molecular mechanism	29
	3.7	Discussion	31
4	AuN	VP-enhanced Holographic-SPI	33
	4.1	Abstract	33
	4.2	Introduction	34
	4.3	Reconstruction algorithm	36
		4.3.1 Maximum-Likelihood Phase Retrieval	38
		4.3.2 Single-pixel Behavior	39
		4.3.3 Finding the most likely solution	41
	4.4	Results	42
		4.4.1 Signal level dependence of reconstruction quality	45
		4.4.2 Heterogeneity of target object	47
	4.5	Conclusions	51
5	Latt	tice-enhanced Holographic-SPI	53
	5.1	Abstract	53
	5.2	Introduction	54
	5.3	Problem Formulation	56
		5.3.1 Scattering Strength of Lattice	58
		5.3.2 Reconstruction Algorithm	59
	5.4	Results	61
	5.5	Discussion	64

6	Holo	ographic-SPI Experiment	66
	6.1	Abstract	66
	6.2	Overview	67
	6.3	Samples	67
		6.3.1 Synthesis and Deposition	68
	6.4	Results	70
	6.5	Discussion	76
7	Sum	amary and Outlook	78
8	Sup	plementary	82
	8.1	Sample Preparation	82
	8.2	Cryo-EM structure determination	83
	8.3	Classification, Discrete Heterogeneity and Polymorphism	85
		8.3.1 Classification	85
		8.3.2 Discrete Heterogeneity	85
		8.3.3 Polymorphism	87
	8.4	Phase retrieval	87
	8.5	Architecture and Training of β -VAE	89
		8.5.1 Pre-processing	89
		8.5.2 Network Parameters	89
		8.5.3 Training performance	90
		8.5.4 Choosing β and latent space dimensions	90
		8.5.5 Stability for different random initialization	92
	8.6	Particle Size Determination	92
	8.7	Local Orientation Optimizer	94
	8.8	Performance of VAE on simulated data	94
	8.9	MD Simulation	95
9	App	endix	97
	9.1	Training VAE on Simulated Data	97
	9.2	Grid Search Optimization	100
Re	eferen	ces 1	103

List of Publications

The following publications/preprints have resulted from the work presented in this dissertation:

- Abhishek Mall, Zhou Shen and Kartik Ayyer. 'High-background X-ray single particle imaging enabled by holographic enhancement with 2D crystals". IN PREPARATION, 2025.
- Abhishek Mall, Anna Munke, Zhou Shen, Parichita Mazumder, Johan Bielecki, Armando Estillore, Chan Kim, Romain Letrun, Jannik Lübke, Safi Rafie-Zinedine, Adam Round, Ekaterina Round, Michael Rütten, Amit K. Samanta, Abhisakh Sarma, Tokushi Sato, Florian Schulz, Carolin Seuring, Tamme Wollweber, Lena Worbs, Patrik Vagovic, Richard Bean, Adrian P. Mancuso, N. Duane Loh, Tobias Beck, Jochen Küpper, Filipe R.N.C. Maia, Henry N. Chapman and Kartik Ayyer. 'Observation of aerosolization-induced morphological changes in viral capsids". arXiv:2407.11687 (2024).
- Abhishek Mall and Kartik Ayyer. 'Holographic single-particle imaging for weakly scattering, heterogeneous nanoscale objects". Phys. Rev. Applied 19, 054027 (2023).

The following publications/preprints arose from experiments in which I participated, contributing during beamtime campaigns and collaborative data collection efforts:

- Zhou Shen, Margarita Samoli, Onur Erdem, Johan Bielecki, Amit Kumar Samanta, Armando Estillore, Chan Kim, Yoonhee Kim, Jayanath Koliyadu, Romain Letrun, Federico Locardi, Jannik Lübke, **Abhishek Mall**, Diogo Melo, Grant Mills, Safi Rafie-Zinedine, Adam Round, Tokushi Sato, Raphael de Wijn, Tamme Wollweber, Lena Worbs, Yulong Zhuang, Adrian P. Mancuso, Richard Bean, Henry N. Chapman, Jochen Küpper, Ivan Infante, Holger Lange, Zeger Hens and Kartik Ayyer. 'Direct observation of the exciton polaron by serial femtosecond crystallography on single CsPbBr₃ quantum dots". arXiv:2502.02343 (2025).
- Alessandro Colombo, Mario Sauppe, Andre Al Haddad, Kartik Ayyer, Morsal Babayan, Rebecca Boll, Ritika Dagar, Simon Dold, Thomas Fennel, Linos Hecht, Gregor Knopp, Katharina Kolatzki, Bruno Langbehn, Filipe R. N. C. Maia, Abhishek Mall, Parichita Mazumder, Tommaso Mazza, Yevheniy Ovcharenko, Ihsan Caner Polat, Dirk Raiser, Julian C. Schäfer-Zimmermann, Kirsten Schnorr, Marie Louise Schubert, Arezu Sehati, Jonas A. Sellberg, Björn Senfftleben, Zhou Shen, Zhibin Sun, Pamela H. W. Svensson, Paul Tümmler, Sergey Usenko, Carl Frederic Ussling, Onni Veteläinen, Simon Wächter, Noelle Walsh, Alex V. Weitnauer, Tong You, Maha Zuod, Michael Meyer, Christoph Bostedt, Davide E. Galli, Minna Patanen and Daniela Rupp. 'SPRING: an effective and reliable framework for image reconstruction in single-particle coherent diffraction imaging". arXiv:2409.07413 (2024).
- Zhou Shen, Paul Lourdu Xavier, Richard Bean, Johan Bielecki, Martin Bergemann, Benedikt J. Daurer, Tomas Ekeberg, Armando D. Estillore, Hans Fangohr, Klaus Giewekemeyer, Mikhail Karnevskiy, Richard A. Kirian, Henry Kirkwood, Yoonhee Kim, Jayanath C.P. Koliyadu, Holger Lange, Romain Letrun, Jannik Lübke, Abhishek Mall, Thomas Michelat, Andrew J. Morgan, Nils Roth, Amit K. Samanta, Tokushi Sato, Marcin Sikorski, Florian Schulz, Patrik Vagovic, Tamme Wollweber, Lena Worbs, Filipe Maia, Daniel A. Horke, Jochen Küpper, Adrian P. Mancuso, Henry N. Chapman, Kartik Ayyer and N. Duane Loh. 'Resolving nonequilibrium shape variations among millions of gold nanoparticles". ACS NANO 2024 18 (24), 15576-15589 (2024).

- Clément E. Blanchet, Adam Round, Haydyn D.T. Mertens, Kartik Ayyer, Melissa Graewert, Salah Awel, Daniel Franke, Katerina Dörner, Saša Bajt, Richard Bean, Tânia F. Custódio, Raphael de Wijn, E. Juncheng, Alessandra Henkel, Andrey Gruzinov, Cy M. Jeffries, Yoonhee Kim, Henry Kirkwood, Marco Kloos, Juraj Knoška, Jayanath Koliyadu, Romain Letrun, Christian Löw, Jana Makroczyova, Abhishek Mall, Rob Meijers, Gisel Esperanza Peña Murillo, Dominik Oberthür, Ekaterina Round, Carolin Seuring, Marcin Sikorski, Patrik Vagovic, Joana Valerio, Tamme Wollweber, Yulong Zhuang, Joachim Schulz, Heinrich Haas, Henry N. Chapman, Adrian P. Mancuso and Dmitri Svergun. 'Form factor determination of biological molecules with X-ray free electron laser small-angle scattering (XFEL-SAS)". Communications Biology 6, 1057 (2023).
- Fabian Trost, Kartik Ayyer, Mauro Prasciolu, Holger Fleckenstein, Miriam Barthelmess, Oleksandr Yefanov, J. Lukas Dresselhaus, Chufeng Li, Saša Bajt, Jerome Carnis, Tamme Wollweber, **Abhishek Mall**, Zhou Shen, Yulong Zhuang, Stefan Richter, Sebastian Karl, Sebastian Cardoch, Kajwal Kumar Patra, Johannes Möller, Alexey Zozulya, Roman Shayduk, Wei Lu, Felix Brauße, Bertram Friedrich, Ulrike Boesenberg, Ilia Petrov, Sergey Tomin, Marc Guetg, Anders Madsen, Nicusor Timneanu, Carl Caleman, Ralf Röhlsberger, Joachim von Zanthier and Henry N. Chapman. 'Imaging via correlation of x-ray fluorescence photons'. Physical Review Letters 130, 173201 (2023).
- Yulong Zhuang, Salah Awel, Anton Barty, Richard Bean, Johan Bielecki, Martin Bergemann, Benedikt J. Daurer, Tomas Ekeberg, Armando D. Estillore, Hans Fangohr, Klaus Giewekemeyer, Mark S. Hunter, Mikhail Karnevskiy, Richard A. Kirian, Henry Kirkwood, Yoonhee Kim, Jayanath Koliyadu, Holger Lange, Romain Letrun, Jannik Lübke, Abhishek Mall, Thomas Michelat, Andrew J. Morgan, Nils Roth, Amit K. Samanta, Tokushi Sato, Zhou Shen, Marcin Sikorski, Florian Schulz, John C.H. Spence, Patrik Vagovic, Tamme Wollweber, Lena Worbs, P. Lourdu Xavier, Oleksandr Yefanov, Filipe R.N.C. Maia, Daniel A. Horke, Jochen Küpper, N. Duane Loh, Adrian P. Mancuso, Henry N. Chapman and Kartik Ayyer. 'Unsupervised learning approaches to characterizing heterogeneous samples using X-ray single-particle imaging". IUCRJ 9, 204–214 (2022).

The following resulted publications were produced during my master's dissertation/collaborative research projects:

- Mahesh Bhupati*, **Abhishek Mall***, Anshuman Kumar and Pankaj K. Jha. 'Deep learning-based variational autoencoder for classification of quantum and classical states of light". Advanced Physics Research 4(2), 2400089 (2025).
- Saurabh Dixit, Nihar Ranjan Sahoo, **Abhishek Mall** and Anshuman Kumar. 'Mid infrared polarization engineering via sub-wavelength biaxial hyperbolic van der Waals crystals". Scientific Reports 11, 6612 (2021).
- Abhishek Mall, Abhijeet Patil, Amit Sethi and Anshuman Kumar. 'A cyclical deep learning-based framework for simultaneous inverse and forward design of nanophotonic metasurfaces". Scientific Reports 10, 19427 (2020).
- Abhishek Mall, Abhijeet Patil, Dipesh Tamboli, Amit Sethi and Anshuman Kumar. 'Fast design of plasmonic metasurfaces enabled by deep learning". JOURNAL OF PHYSICS D: APPLIED PHYSICS 53(49), 49LT01 (2020).

List of Open-Source Codes

The following open-source code have been developed as part of the work presented in this dissertation:

- Chapter 3 The code for the β -VAE: https://github.com/AyyerLab/StrucNN/tree/master/ms2vae.
- Chapter 4 The data generation and the optimization algorithm: https://github.com/AyyerLab/RefSPI-MaxLP.
- Chapter 5 The data generation and the optimization algorithm: https://github.com/AyyerLab/Lattice-Ref/tree/orient.

List of Figures

X-ray SPI Experiment. (a) MS2 bacteriophage particles, \sim 27 nm in diameter, were aerosolized using an electrospray and focused with an aerodynamic lens stack to the interaction region within the X-ray beam of $250 \times 250 \,\mathrm{nm^2}$ focus. The top inset shows a representative cryo-electron microscopy (cryo-EM) micrograph of the particles. (b) The 3D structure of MS2 capsid determined by cryo-EM (resolution $0.49 \,\mathrm{nm}$), served as the control for the subsequent X-ray SPI experiment. (c) The same cryo-EM structure was low-pass filtered to the resolution of the conventional X-ray SPI structure. (d) The structure retrieved from diffraction data (6.1 nm resolution) using the conventional analysis pipeline is notably different from 21 3.2 Analysis Pipeline. (a) Schematic of diffraction data analysis workflow. All steps other than the unsupervised learning ones are part of the standard SPI workflow. (b) Detailed flow chart of the unsupervised learning step to generate the structural latent space and associated 3D Fourier intensity volumes. The pipeline involves training a β -VAE with a local orientation optimizer. Every 20th epoch, the optimizer outputs an improved estimate for the orientation (Ω) given the 3D Fourier volumes, dataset, and the current estimate of the orientations. (c) Schematic representation of the β -VAE network. The model takes 2D class-average intensities and orientations as input and encodes them into a latent space via an encoder network. This latent space coordinate (Z) is subsequently utilized by a decoder network to reconstruct 3D Fourier volumes. . .

3.1

3.3	Structural Landscape. (a) The latent space learned by the β -	
	VAE colored by the estimated diameter (d) of individual patterns.	
	The plot highlights two distinct trajectories selected to capture	
	the structural variation phenomenon within the latent space. The	
	retrieved electron density of MS2 particles via phase retrieval of	
	Fourier volumes generated by decoder network of $\beta\textsc{-VAE}$ network is	
	shown in the grid. (b) The dotted <i>Gray</i> trajectory, following from top	
	to bottom in (a), depicts the shape-size variation in the ensemble of	
	capsids. (c) The <i>Green</i> trajectory, progressing from left to right in (a),	
	corresponds to different shape realizations for a fixed size of capsid.	
	Red-white-blue colored radially. (d) Encapsulated overlay of the	
	3D structure of the MS2 capsid from the low-pass filtered cryo-EM	
	reconstruction (gray) and the dehydrated X-ray SPI reconstruction	
	(green). The overlap highlights the altered conformations in the	
	vicinity of the 5-fold and 3-fold sites	28
3.4	Dehydrated capsid model. (a-b) The pentameric (5-A/B) and hex-	
	americ (3-A/B and 3-C/C) faces of the T=3 icosahedral capsid shell	
	from the 2MS2 PDB structure. At the 5-fold axis FG loops of B (B-FG	
	loop, green, a), and at the 3-fold axis FG-loops of A (A-FG loop, sky	
	blue, b) and C (C-FG loop, red) are crucial for capsid assembly and	
	curvature. (c) The A-FG loop and C-FG loop exhibit significant	
	fluctuations compared to B-FG loop (residues 66-82, shaded region).	
	The Root Mean Square fluctuation (RMSF) was calculated from a	
	20 ns vacuum MD-trajectory of A/B and C/C dimers. (d) Trans-	
	formed hexameric building block designed/modeled from the X-ray	
	SPI map. At the 3-fold axis, C/C dimers move toward the capsid	
	center. (e) Map generated from transformed capsid model (at 6.1	
	nm resolution). The left half is in a similar representation as the	
	experimental X-ray SPI map (Fig. 3.1d) for visual comparison	30
4.1	Attached Deference Object (a) Simulated diffraction nottons	
4.1	Attached Reference Object. (a) Simulated diffraction pattern contributed for a random object in a normal single-particle imaging	
	(SPI) case with 4810 photons. (b) Diffraction pattern from the same	
	particle with a small AuNP attached (10,000 photons). If background is present, structural information can be discorned at higher scatter	
	is present, structural information can be discerned at higher scatter-	
	ing angles in the holographic case. Insets show the true projected	27
	electron density of the objects	36

4.2	pixel for a holographic-SPI diffraction data. (a)-(d) Average number of photons vs relative phase shifts of gold sphere with respect to the target object. The ideal intensity on the same pixel is represented by the orange line. (e) & (f) Log-likelihood landscapes obtained from diffraction data for case (a) & (d), respectively. The '×' denotes the true value of $F(\mathbf{q})$ maximizing the log-likelihood. The grid lines (1 st - orange and 2 nd - blue) depict the size of pattern search grid in consecutive iterations
4.3	Performance. Simulation results for homogeneous target object attached to a spherical AuNP as reference. (a) Magnitude of reconstructed Fourier model for high signal diffraction data with MaxLP method (10 ⁵ ph/frame). (b) Same for low signal diffraction data (2000 ph/frame). Both datasets had 10 ⁴ frames. Dashed rings highlight the FRC=0.5 cutoff. (c) Comparison of Fourier ring correlation (FRC) between reconstructions and ground truth with different signal level diffraction data. Maximum-likelihood Phaser (MaxLP), Divide and Concur (DivCon), High Signal (H.S.) and Low Signal (L.S.). (d) Normalized error (difference between successive iterations) vs iteration number showing faster convergence for higher signal levels as observed in conventional SPI as well [4].
4.4	Latent Parameters. Error distribution for reconstructed latent parameters for homogeneous target object attached with a spherical AuNP as reference for low (L.S.) and high signal (H.S.) levels. (a) In-plane orientation, (b) diameter of gold sphere, (c) & (d) relative displacements between center of target object and reference in <i>x</i> -and <i>y</i> - direction. The vertical lines in (b) and the grid lines in (c) and (d) show half the sampling rate, which sets a lower bound on the width of the distributions
4.5	Signal Level Dependence. Evaluation metrics of Maximum-likelihood phaser (MaxLP) for different photon signal levels. (a) q value when FRC = 0.5 vs number of photons/frame. The horizontal dashed line corresponds to a resolution of 1 real-space pixel. Standard deviation values for (b) diameter errors, (c) orientation errors, and (d) shift errors in x - and y - direction. The horizontal dashed lines in (b)-(d) indicate half the sampling rate.

4.6 **Structural Heterogeneity.** Simulation results for structural heterogeneity in the target object (a) Average structure of target object which exists in one of two discrete states (State A & State B, shown in inset). (b) Reconstructed real-space target object with an AuNP sphere attached using MaxLP. (c) Reconstructed real-space target object without reference attached. (d) Average structure of target object which exists in a continuous distribution of states. Inset shows the target object with random sub-unit where arrow depicts the free direction of motion for sub-unit in each shot. (e) Reconstructed real-space target object with an AuNP sphere attached using MaxLP. (f) Reconstructed real-space target object without reference attached. (g) Comparison of Fourier ring correlation (FRC) between holographic-SPI and normal-SPI for the different scenarios. 49

5.1 Holographic SPI. (a) Schematic of the holographic SPI setup. A 2D crystal lattice serves as the *reference*, while Ribosome particles (blue) are the target objects. The lattice is positioned on one side of the substrate, with target particles randomly distributed on the opposite side. The measured far-field diffraction pattern on the detector results from the coherent sum of Bragg peaks from several illuminated unit cells of the lattice and the scattering signal from a single target particle. (b) Far-field intensity modulation shown on a logarithmic scale. These modulations reflect Bragg peaks perturbed by the target object signal within the illumination area. The modulation, ΔI , is defined as the difference between the intensity from the lattice alone, $I=|F_{\rm L}({\bf q})|^2$ and the intensity with both the lattice and the target object $I = |F_L(\mathbf{q}) + \varphi \cdot F_o(R^\top \mathbf{q})e^{i2\pi \mathbf{q} \cdot \mathbf{s}}|^2$, for a given translation shift within unit cell, in-plane orientation, and incident fluence. 5.2 Scattering Strength of Lattice. The plot illustrates the uncertainty in estimating the scattering amplitude of $F_o(\mathbf{q})$, quantified by $\sqrt{\mathrm{tr}(C)}$ (the square root of the combined amplitude and phase variances of $F_o(\mathbf{q})$) as a function of the scattering strength of the 2D crystal lattice, with a fixed background $B^2(\mathbf{q})$. Results are shown for three different scattering amplitudes of $F_o(\mathbf{q})$. Solid lines depict analytical estimates based on the inverse curvature of the objective function, while dots represent uncertainties obtained from simulated data through curve fitting.

58

- **Performance.** (a) Ground truth 2D projection of the Ribosome 5.3 electron density. (b) Unit cell of the 2D crystal lattice, modeled as random noise. (c) Scattering intensity as a function of q for the 2D lattice (blue), Ribosome target object (red), and background (yellow). The background exceeds the signal of Ribosome by more than 10^5 , while the lattice intensity is comparable to or greater than the background. (d) Reconstructed electron density of the Ribosome (scale bar: 10 nm). (e) Fourier ring correlation (FRC) between the reconstruction and the ground truth $F_o(q)$. Green lines indicate FRC values averaged over 8 random-start reconstructions; the shaded region represents the standard deviation across runs. (f) Ratio of estimated to true incident fluence, φ . (g) Distribution of estimation errors for in-plane orientation angle θ across random runs. (h) Distribution of translational shift errors in the x and y directions for the target object within the unit cell (unit cell size: 100 nm). The performance is evaluated for exposure time $t=1, \ldots, \ldots$
- 5.4 **Evaluation of Reconstructions.** (a) Fourier ring correlation (FRC) values at $q=0.26\,\mathrm{nm^{-1}}$ vs background B^2 , for various exposure times (t). Each data point represents the maximum FRC value from eight random-start reconstruction runs. The horizontal solid line at FRC = 1 denotes the theoretical limit corresponding to infinite exposure time, $t\to\infty$. (b) Contour plot of FRC values (color scale) as a function of B^2 and t, both on logarithmic scales. Green circles indicate regions where FRC ≥ 0.5 , orange crosses mark regions with $0 < \mathrm{FRC} < 0.5$, and the black line traces the threshold boundary at FRC = 0.5. The sawtooth pattern along the bottom edge represents the approach to infinite exposure time $t\to\infty$ where FRC reaches 1. 63

6.1 **PS Monolayer and Sample Preparation.** (a) Langmuir-Blodgett setup used to form a monolayer of polystyrene (PS) nanospheres at the air-water interface and transfer it onto a Si₃N₄ substrate. (b) Si₃N₄ substrates with varying transparent window sizes, featuring a PS nanosphere monolayer on one side and dispersed target particles on the opposite side. (c) Custom sample holder for mounting the Si₃N₄ substrates, enabling fixed-target delivery of the lattice and target particles into the X-ray beam. (d, e) SEM images of PS nanosphere monolayers with diameters of 100 nm and 200 nm, respectively. (f) SEM image of 80 nm gold nanoparticles (AuNPs). . 69

6.2 **Diffraction Data.** (a) Average scattering background from the beamline and the air-exposed Si₃N₄ window setup without samples. (b) Powder diffraction pattern, obtained by integrating all diffraction images collected from various regions of interest for a 200 nm PS nanosphere lattice. The central spot corresponds to the maximum intensity. (c) Preliminary evaluation of a dataset collected from a 200 nm PS lattice with 80 nm AuNPs as target objects. Single 30-second exposure from a 2D crystal of 200 nm PS nanospheres, showing holographic modulation induced by the AuNPs. Dark regions are masked due to strong background scattering from the beamline. . . 71

Holographic Enhancement. (a) Average intensity from 500 aligned 6.3 diffraction patterns. Holographic interference causes intensity variation between otherwise symmetry-related peaks. This is visually most apparent in weak peaks as shown in green circles. (b) Simulation of 200 nm PS with 80 nm AuNPs as target objects. Intensity vs q for single 80 nm AuNP vs 25 PS spheres (200 nm). The vertical dotted lines are positions of different order of Bragg peaks. 72

6.4	Crossed Grating Setup and Diffraction Data. (a) Schematic of	
	the experimental setup: two crossed gratings generate a periodic	
	exit wave that is subsequently modulated by the sample. The inset	
	shows the fixed-target sample delivery configuration and grating	
	specifications. (b) SEM image of one of the EUV interference lithog-	
	raphy gratings, highlighting a stacking fault at the intersection	
	of two regions. Inset: average background scattering from the	
	beamline and the air-exposed dual-grating window setup without	
	a sample. (c) Single 10-second exposure showing diffraction from	
	an individual AuNP with crossed gratings. (d) 100-second exposure	
	of an AuNP dimer under the same configuration. In both (c) and	
	(d), the diffuse signal is sufficiently strong to reveal the particles	74
6.5	Imperfections in Gratings. Scan of 2D Grating with empty SiN	
	membrane with exposure time of 2 sec. A total of around 5000	
	frames were collected for characterizing (a) Brightness scaling (b)	
	Relative bar width (0.25 on average) (c) Sharpness of average profile,	
	which reflects the degree of variations within the focal spot	75
8.1	FSC Curve. FSC curve of the cryo-EM reconstruction generated	
	using cryoSPARC [5] for the cryo-EM reconstruction of the MS2	
	capsid from the same batch as used for the X-ray SPI experiment.	
	The average resolution of 0.49 nm was estimated based on FSC =	
	0.143 threshold [6] (black dashed line).	84
8.2	Classification. (a) Examples from the 50 2D intensity models	
	obtained from the initial EMC classification. (Dashed pink grid)	
	Models rejected prior to generating the training dataset for the	
	$\beta\textsc{-VAE}.$ (Bottom row) Examples of the 2D intensity models used for	
	the dataset generation. (b) Histogram of the fitted diameters for	
	the 2D intensity classes dataset (10,000 classes). Different structure	
	types are manually marked in the distribution as icosahedral (red),	
	octahedral (blue), and others, including dimers, outliers, etc. (green).	
	(c) The corresponding examples of 2D intensity models for each	
	structure class. (Top row) Examples of classes with panel gaps and	
	detector artifacts, which had fitted diameters >40 nm	86

8.3	Discrete Heterogeneity. (a) Examples from the diffraction dataset of 2D intensity models and corresponding electron density projections (inset) via phase retrieval; the scale bar is 30 nm. (b) 3D										
	structure of the MS2 capsid reconstructed from the octahedral data.	87									
8.4	Phase retrieval transfer function (PRTF). (a) Smoothed phase retrieval transfer function (PRTF) vs q . The solid lines represent the azimuthal average PRTF conventionally used to determine the resolution of the structure. The typical $1/e$ cutoff is shown in gray. The resolution at the cutoff for both capsid structures was estimated to be ≈ 6.1 nm. (b) Slice at 001-plane through the Fourier volume of the MS2 capsid for icosahedral (top) and octahedral (bottom) structures retrieved using $Dragonfly$ [7]. Fig. 3.1d & Fig. 8.3b shows the corresponding phased electron density	88									
8.5	Training of <i>β</i> -VAE. (a) Comparison between input 2D intensity data and the corresponding output (reconstruction) by <i>β</i> -VAE. (b) Loss evolution during <i>β</i> -VAE training exhibited a decline over the 1000 epochs. However, the decrease was not significant later in training, prompting the decision to terminate further training. The depicted loss encompasses both the Mean Squared Error (MSE) loss for reconstruction and the Kullback-Leibler (KL) divergence loss. (c) <i>β</i> -VAE Loss <i>versus β</i> values. The plot illustrates a rise in loss as <i>β</i> values increase. The optimal trade-off between minimizing loss and providing sufficient regularization occurred at β = 0.5 (red dashed line). (d) Latent space representation of the <i>β</i> -VAE color labeled with $\sigma = \sqrt{\sigma_1^2 + \sigma_2^2}$	91									
8.6	Latent Space. Latent space representation of the β -VAE for different random initializations of weight and bias parameters. The low-dimensional embedding varies due to the random start, converging to nearby minima. However, it maintains the same information for shape and size variations	92									
8.7	Particle Size Distribution. Histogram depicting the particle size distribution, represented by fitted diameter values, d (nm). These values were obtained through spherical particle model fitting on the Fourier volumes reconstructed using the <i>decoder</i> network of the optimized β -VAE	93									

8.8	Root mean square deviation (RMSD). Root mean square devia-	
	tion (RMSD) vs Epoch. The RMSD values were evaluated between	
	the orientation estimates at two consecutive updates of the Local	
	Optimizer. The update is performed every 20^{th} epoch of the training.	95
8.9	Simulated Dataset. (a) Comparison between the input 2D intensity	
	data and the corresponding VAE reconstruction on the simulated	
	dataset. (b) Latent space representation of the VAE; the red points	
	indicate the data sample shown in (a), with coordinates provided	
	in the inset. (c) Ground truth distribution of size and roundness	
	parameters used to generate the simulated dataset of icosahedra	
	particles. (d, e) Latent space representations of VAE color-coded by	
	roundness and size, respectively	96

List of Tables

8.1	Architecture of β -VAE .												93

1

Introduction

One night, you spotted an alien ship landing quietly in a dense forest. Curious but cautious, you followed its faint trail, keeping low to avoid being seen. In a hidden clearing, you watched as the aliens placed a parasitic, shape-shifting sculpture on the ground. It glowed faintly—an ominous object that looked like a weapon to destroy the world.

Taking the sculpture or trying to grab it was too risky—it could alert the aliens and put you in serious danger. Instead, you chose to document what you saw. You snapped as many photos as possible, but the darkness made it impossible to use a bright flash without drawing attention. The images turned out blurry, with fuzzy outlines and distorted details. To make matters worse, the sculpture kept subtly changing shape, so each photo captured a slightly different version of it.

Now, back at home, you face a daunting challenge: reconstruct the full 3D structure of the sculpture. Using these grainy, inconsistent images, you must piece together a clear 3D model—capturing every detail—to reveal what this object truly is and the threat it may pose.

This metaphor captures the essence of X-ray single-particle imaging (SPI) - a powerful technique capable of reconstructing full 3D structures of nanoparticles from millions of noisy, randomly oriented diffraction snapshots [4, 8–10]. By employing ultrashort, ultra-intense X-ray pulses from X-ray free-electron lasers (XFELs)[11, 12], SPI records each diffraction pattern from an individual particle just before the sample is destroyed - a process known as "diffraction-before-destruction"[13].

The ability to visualize biomolecular structures at high resolution has profoundly advanced the field of structural biology [14–16]. Techniques such as

X-ray crystallography, cryogenic electron microscopy (cryo-EM), and nuclear magnetic resonance (NMR) spectroscopy have enabled researchers to uncover intricate biomolecular architectures [17–19]. A core principle in structural biology is that the function of a biomolecule is intrinsically tied to its structure - even subtle conformational changes can affect its interactions or biological activity within the environment [20, 21]. Capturing both static structures and dynamic behaviors is therefore essential for understanding biological mechanisms under physiologically relevant conditions.

The profound impact of structural insights has been recognized through prestigious scientific honors, such as Nobel Prizes awarded for breakthroughs in imaging and structure determination methods that have significantly enhanced our ability to observe biomolecular forms and motions [22–24]. Despite these advancements, the pursuit continues. Crystallography relies on highly ordered crystals, posing challenges in studying flexible, transient, or heterogeneous systems [25–27]. Cryo-EM, while avoiding crystallization, necessitates freezing target single particles, which can obscure ultrafast dynamic processes occurring at physiological temperatures [28, 29]. SPI fills a crucial gap by capturing structures without the need for crystallization or freezing. It offers *in situ* condition possibilities and tolerates sample variability, enabling the observation of biomolecules in action through time-frozen snapshots [9, 12, 30].

However, the SPI technique encounters several formidable challenges. Firstly, the signal-to-background ratio is often poor, especially for small or weakly scattering particles [31, 32]. Background scattering from aerosol carriers, liquid jets, beamline optics, and detector artifacts can overpower the already weak signal, which rapidly decays at high scattering angles [9, 31, 33]. Secondly, while radiation damage is mitigated by femtosecond pulses, it still poses a concern for long exposures and synchrotron-based experiments [34]. Thirdly, structural heterogeneity within biological samples blurs averaged reconstructions, necessitating sophisticated classification techniques [4, 8].

This thesis addresses these challenges by integrating experimental innovation with computational advancements. Specifically, it presents three distinct contributions to the field:

Structural dynamics in viral systems (Chapter 3) explores how aerosolized MS2 bacteriophage viruses undergo changes in shape and size during dehydration. Using Bayesian methods and unsupervised learning, we analyze SPI data to uncover a continuous landscape of viral capsid shapes and sizes. This reveals a spectrum of structures, ranging from fully hydrated icosahedral forms to previously uncharac-

terized asymmetric capsids. These findings illuminate biomolecular mechanisms that protect viral genomes under environmental stress. This work demonstrates how SPI in combination with machine learning techniques can resolve structural ensembles in the context of conformational dynamics.

Holographic-SPI to retrieve weak signals (Chapter 4) describes how to overcome the limitations imposed by background noise from various sources through reference-enhanced SPI, a technique that involves attaching a known, strongly scattering reference particle (such as a gold nanoparticle or a 2D crystal lattice) to the target object. This holographic interference boosts the signal, enabling orientation recovery and phase retrieval, even in low signal conditions [35]. The chapter presents a novel algorithm based on maximum-likelihood pattern search that efficiently scales with dataset size and resolves both orientations and multiple latent parameters. This robust reconstruction approach offers high-resolution imaging in low-signal limits, even for heterogeneous samples.

High-resolution SPI at synchrotron sources (Chapter 5 & 6) when XFELs are limited in availability for routine SPI, highlighting the need to adapt SPI techniques for use with synchrotron sources which is considered impossible. However, synchrotrons provide lower flux and require longer exposure times, which can lead to radiation damage in biological target samples. These chapters introduce a fixed-target, lattice-enhanced holographic SPI configuration. The approach employs a nano-fabricated two-dimensional crystal on a thin substrate to generate strong Bragg peaks that interfere with the weak sample signal. This customized holographic framework enables the reliable extraction of weak biomolecular signals, even in backgrounds up to 10⁵ times stronger than the sample signal. This advancement significantly extends the capabilities of routine structural biology at synchrotron facilities. [36].

These studies collectively demonstrate how SPI can pave the way for high-resolution, ultrafast dynamic SPI, making it a valuable tool in structural biology. Due to its compatibility with heterogeneous, flexible, and hard-to-crystallize systems, SPI provides a complementary approach for capturing ultrafast structural dynamics and uncovering functional mechanisms at room temperature. Recent advances in sample delivery, background suppression, and machine learning–based analysis pipelines are accelerating SPI's progress toward achieving sub-nanometer resolution.

By addressing key challenges in signal detection, resolution enhancement, and sample heterogeneity, this dissertation contributes to the broader goal of realizing the full potential of SPI but as a mainstream method for dynamic, high-resolution, room-temperature biomolecular imaging.

Basic Concepts

 ≺ This chapter provides a concise overview of the fundamental concepts and background information essential for understanding the experimental and computational work in this dissertation. For a more in-depth understanding, relevant sources are cited accordingly.

2.1 Biomolecules

Biomolecular assemblies—such as viruses and protein complexes—are among the smallest yet most intricate systems in nature. These nanoscale entities, typically ranging from tens to hundreds of nanometers, are composed of repeating subunits that self-assemble into highly organized and functional architectures [37]. Their structural organization underpins critical biological processes, including replication, enzymatic catalysis, and host-pathogen interactions [38, 39].

Understanding the structural and dynamic properties of these assemblies in their native environments is essential for advancing virology, structural biology, and biotechnology [40, 41]. For instance, probing the conformational dynamics of viral capsids or protein machines reveals how these systems adapt to environmental cues, maintain stability, and facilitate function. Such insights are crucial for developing antiviral therapies, designing vaccines, and engineering synthetic biomolecular systems [42].

2.1.1 Structure and Function

The function of biomolecules is intrinsically linked to their structure, which follows a hierarchical organization. Primary sequences of proteins and nucleic acids fold into secondary motifs—such as α -helices and β -sheets—which further assemble into stable tertiary and quaternary structures. These higher-order assemblies are maintained by non-covalent interactions that simultaneously confer stability and flexibility necessary for biological activity [37, 38].

Viruses exemplify this principle: their genomes are encased within protein capsids that often adopt symmetric architectures, like icosahedral symmetry, to optimize packaging efficiency and mechanical stability [42, 43]. For example, the MS2 bacteriophage forms a T=3 icosahedral capsid from 180 identical coat protein subunits arranged into A/B and C/C dimers [44, 45]. These dimers assemble into pentamers and hexamers around the 5-fold and 3-fold symmetry axes, respectively, creating a robust shell that interacts with both the viral genome and host receptors [46–48].

Similarly, protein complexes such as the bacterial ribosome operate as molecular machines composed of structured RNA and proteins. The ribosome comprises two subunits (30S and 50S), each formed from ribosomal RNA (rRNA) and dozens of proteins, precisely organized to coordinate protein synthesis [49–52].

Non-covalent interactions provide both structural cohesion and adaptability. Viral capsids, for example, exhibit tightly packed subunit interfaces that permit localized conformational changes in response to environmental stimuli such as pH or ionic strength [53, 54]. Understanding how symmetry, robustness, and adaptability are balanced within these assemblies provides valuable insights for antiviral strategy and synthetic nanostructure design [41].

2.1.2 Heterogeneity and Conformational Dynamics

Biomolecules are inherently dynamic, transitioning between multiple conformational states that correspond to local minima in a complex energy landscape [55, 56]. These structural transitions span diverse temporal and spatial scales, from picosecond side-chain fluctuations to global rearrangements over milliseconds or longer [39, 57–59].

In viruses, such flexibility underlies essential processes like capsid breathing, genome release, and response to environmental stress [48, 54]. For instance, the FG-loops near the 3-fold axes in MS2 bacteriophage adjust pore size and curvature during dehydration or ionic changes, influencing both assembly and infectivity [45,

60-63].

Protein complexes also rely on conformational plasticity. During bacterial translation, the ribosome's small subunit undergoes coordinated shifts that enable tRNA and mRNA translocation, facilitated by subtle movements of RNA helices and protein domains [50, 51, 64, 65].

This structural heterogeneity arises from thermal fluctuations, allosteric regulation, or incomplete assembly and enables precise control of functional transitions [41, 66, 67]. Molecular dynamics (MD) simulations, which track atomic motion over time, have proven instrumental in characterizing these conformational pathways [68, 69].

Capturing the interplay between structural order and dynamic flexibility is essential for understanding how biomolecular assemblies carry out complex, regulated tasks. The study of these behaviors increasingly relies on advanced structural techniques capable of probing both static and transient states under near-native conditions—a need that has driven the development of powerful X-ray imaging sources.

2.2 X-ray Sources

High-resolution X-ray imaging has been foundational to structural biology, enabling atomic-level visualization of biomolecules. The discovery of X-rays by Wilhelm Röntgen in 1895 and the subsequent demonstration of X-ray diffraction by Max von Laue laid the groundwork for X-ray crystallography, a method later formalized by William and Lawrence Bragg [70–72].

Early X-ray tubes, which produced radiation through electron-target collisions, were limited in brightness and tunability [73]. The introduction of synchrotron radiation in the 1970s revolutionized the field by delivering high-intensity, tunable, and collimated X-ray beams suitable for a wide range of biological investigations [74]. More recently, X-ray free-electron lasers (XFELs) have advanced the field further, generating ultrashort pulses with unprecedented brightness and coherence, ideal for studying fast structural dynamics [11, 75, 76].

These technological innovations have transformed X-ray imaging into a versatile platform for probing biological systems with increasing spatial and temporal resolution. In the following subsections, we examine the characteristics and applications of synchrotron and XFEL sources in structural biology.

2.2.1 Synchrotrons

Synchrotrons produce intense, tunable X-rays by accelerating electrons to nearlight speeds in a circular storage ring and steering them through magnetic fields. As electrons are deflected by bending magnets, wigglers, or undulators, they emit synchrotron radiation—characterized by high brightness, broad spectral range, and low divergence [74, 77].

Undulators, a key component of third-generation synchrotrons, generate quasi-monochromatic, highly coherent X-ray beams that are optimal for techniques such as macromolecular crystallography, small-angle X-ray scattering (SAXS), and coherent diffraction imaging (CDI) [78–80]. The performance of these sources is quantified by spectral brightness:

$$B(\lambda) = \frac{F(\lambda)}{(2\pi)^2 \varepsilon_x \varepsilon_y} \tag{2.1}$$

where $F(\lambda)$ is the photon flux, and ε_x , ε_y are the horizontal and vertical beam emittances. Lower emittance values improve beam sharpness and intensity, directly enhancing imaging resolution [74].

Modern synchrotron facilities (3^{rd} and 4^{th} Generation) —including APS (USA), ESRF (France), PETRA III (Germany), and SPring-8 (Japan)—employ advanced magnet lattices and storage ring designs to achieve low emittance and high stability [81–84]. These sources support a broad array of biological applications, from high-resolution protein crystallography to in situ tomography and studies of large macromolecular complexes [85, 86].

However, synchrotron pulses typically have durations in picoseconds to nanoseconds range, limiting their ability to resolve ultrafast processes. To overcome this limitation, XFELs offer a complementary approach with femtosecond-scale time resolution.

2.2.2 X-ray Free-Electron Lasers (XFELs)

XFELs represent the state-of-the-art in X-ray generation, producing ultrashort, coherent pulses with peak brightness up to 10^9 times greater than synchrotrons [87, 88]. Unlike storage rings, XFELs use linear accelerators to propel electron bunches through long undulators. Within the undulators, the self-amplified spontaneous emission (SASE) process converts electron energy into highly coherent X-ray radiation.

The exponential gain in X-ray intensity along the undulator is governed by the

FEL gain length L_G :

$$L_G = \frac{\lambda_u}{4\pi\sqrt{3}\,\rho_{\rm FEL}}\tag{2.2}$$

where λ_u is the undulator period and ρ_{FEL} is the FEL parameter, indicating the efficiency of energy transfer from electrons to photons [89].

XFELs enable the technique of "diffraction-before-destruction," in which ultrashort pulses capture structural information before radiation damage occurs [12, 30, 90]. This approach has revolutionized structural biology by facilitating serial femtosecond crystallography (SFX) and single-particle imaging (SPI), especially for weakly scattering or radiation-sensitive specimens [91–93].

Flagship XFEL facilities include the Linac Coherent Light Source (LCLS) in the USA and the European XFEL in Germany [94, 95]. These platforms support time-resolved studies of ultrafast phenomena in nanoscale systems. Despite their capabilities, XFEL experiments require precise synchronization, advanced sample delivery systems, and complex beam diagnostics [11, 75].

Together, synchrotrons and XFELs provide complementary capabilities for structural biology, spanning from equilibrium imaging of static structures to time-resolved studies of molecular dynamics. These sources form the foundation for cutting-edge imaging techniques, which are explored in the next section.

2.3 Nanoscale Imaging Techniques

Advances in nanoscale imaging have transformed structural biology, enabling visualization of biomolecules with molecular to near-atomic resolution. Techniques such as X-ray crystallography, cryogenic electron microscopy (cryo-EM), X-ray single-particle imaging (SPI), Ptychography and holographic methods provide complementary views of biological structures, accommodating various levels of structural order, sample heterogeneity, and temporal dynamics [86, 96].

Each technique offers distinct advantages: crystallography remains powerful for highly ordered systems, cryo-EM excels at imaging heterogeneous and large complexes, while SPI, Ptychography and holographic methods extend imaging capabilities to non-crystalline and transient structures. Collectively, these methods have illuminated thousands of biomolecular architectures and continue to expand our understanding of structure-function relationships [97].

2.3.1 X-ray Crystallography

X-ray crystallography has long been a foundational technique for determining atomic structures of biomolecules. It relies on the elastic scattering of X-rays from a crystalline lattice. Constructive interference of the scattered waves produces diffraction patterns governed by Bragg's law:

$$n\lambda = 2d\sin\theta \tag{2.3}$$

where n is an integer, λ is the X-ray wavelength, d is the interplanar spacing, and θ is the incidence angle [72]. These patterns are used to reconstruct electron density maps, from which atomic models are built [98].

Synchrotron-based crystallography has enhanced this method by providing intense, tunable beams, enabling the use of advanced phasing strategies and the resolution of increasingly complex structures [49, 99, 100]. The measured diffraction intensities $I(\mathbf{q})$ are proportional to the square of the structure factor:

$$F(\mathbf{q}) = \sum_{j} f_{j}(\mathbf{q}) e^{2\pi i \, \mathbf{q} \cdot \mathbf{r}_{j}}$$
(2.4)

where $f_j(\mathbf{q})$ is the atomic form factor and \mathbf{r}_j is the position of atom j in the unit cell.

A key limitation of crystallography is its reliance on well-ordered crystals, which are often difficult to obtain for flexible or membrane-associated biomolecules. XFEL-enabled serial femtosecond crystallography (SFX) addresses this by using ultrashort pulses to collect diffraction from micro- or nanocrystals before radiation damage sets in [12, 101]. This "diffraction-before-destruction" approach has opened pathways for time-resolved studies of dynamic molecular transformations.

Crystallography remains highly valuable when integrated with complementary methods—such as cryo-electron microscopy, NMR spectroscopy, and computational modeling—to yield a holistic view of biomolecular structure and function [102].

2.3.2 Cryo-Electron Microscopy (Cryo-EM)

Cryogenic electron microscopy (cryo-EM) enables high-resolution imaging of biomolecules in their native, hydrated states - without requiring crystallization [103, 104]. Samples are rapidly vitrified by plunging into liquid ethane, preserving their structural integrity in a thin film of amorphous ice. Electron beams are transmitted through these frozen samples, and the resulting scattering patterns are captured to

produce high-contrast micrographs.

The technique gained momentum with the development of vitrification methods by Dubochet and colleagues in the 1980s. Subsequent breakthroughs in detector technology and image processing, particularly in the 2010s, triggered the so-called "resolution revolution," enabling routine structure determination at 2–4 Å resolution [18].

Cryo-EM encompasses multiple imaging modes, including single-particle analysis (SPA), cryo-electron tomography (cryo-ET), and micro-electron diffraction (MicroED) [105, 106]. Among these, SPA is most widely used for high-resolution structure determination. It involves capturing thousands of 2D projections of identical particles in random orientations, which are then computationally aligned and averaged to reconstruct a 3D electron density map [107].

In many respects, cryo-EM SPA resembles inline holography, as it records the interference of elastically scattered electron waves with an unscattered reference beam. The resulting image contrast is modulated by the microscope's contrast transfer function (CTF), which encodes phase information crucial for structural recovery [108, 109]. Accurate CTF estimation and correction are essential steps in reconstruction pipelines.

A central computational challenge in SPA is the reconstruction of a 3D structure from noisy 2D projections, where both particle orientations and underlying structures are unknown. This gives rise to a latent variable problem, in which the model must simultaneously infer hidden viewing parameters and optimize the 3D volume [5, 110]. This problem is typically formulated as an inverse estimation task, where the goal is to minimize the discrepancy between the measured images I_i and projections $P_{\theta_i}(V)$ of a candidate 3D volume V:

$$\mathcal{L}(\theta) = \sum_{i=1}^{N} |P_{\theta_i}(V) - I_i|^2$$
 (2.5)

State-of-the-art software such as RELION [110], cryoSPARC [5], and EMAN2 [111] use Bayesian inference, maximum likelihood estimation, and deep learning to refine reconstructions, resolve heterogeneity, and identify conformational states within particle ensembles.

Recent innovations, such as time-resolved cryo-EM, now enable visualization of transient molecular events, providing deeper insight into dynamic biological processes [29, 107]. Despite challenges like radiation sensitivity and sample variability, cryo-EM remains a cornerstone of structural biology.

2.3.3 X-ray Single-Particle Imaging (SPI)

X-ray single-particle imaging (SPI) offers a non-crystallographic route to structural information. It involves collecting diffraction patterns from many isolated, randomly oriented particles—such as proteins or viruses—and reconstructing their 3D electron density through computational algorithms [4, 7, 112]. Conceptually, SPI shares common ground with cryo-EM in that both adopt a single-particle analysis (SPA) approach: multiple 2D projections of identical particles are used to infer a 3D structure. However, SPI employs X-rays instead of electrons, leveraging their shorter wavelengths and coherence properties for high-resolution imaging.

XFELs are particularly well-suited for SPI due to their high brightness and coherence, enabling collection of structural data before radiation damage occurs [8, 30, 92, 113]. The scattered intensity from a particle is proportional to the square modulus of its Fourier transform:

$$F(\mathbf{q}) = \int \rho(\mathbf{r}) e^{-2\pi i \, \mathbf{q} \cdot \mathbf{r}} d^3 \mathbf{r}$$
 (2.6)

Phase retrieval algorithms—such as Hybrid Input-Output (HIO) [114] and Difference Map [115]—are used to reconstruct the missing phase information from measured intensities, enabling recovery of 3D structures.

SPI also benefits from the spatial and temporal coherence of XFEL pulses, which are essential for producing high-contrast speckle patterns in coherent diffraction imaging (CDI) [116, 117]. While radiation damage challenge has been addressed for biological samples [118, 119], the use of femtosecond XFEL pulses allows imaging before significant atomic displacement occurs [90, 120]. This has made SPI a key technique for studying radiation-sensitive and heterogeneous specimens with high spatial and temporal resolution.

2.3.4 Fourier Transform Holography

Fourier Transform Holography is a lensless imaging technique that reconstructs an object's complex wavefront by recording its far-field interference with a reference wave. In contrast to iterative phase retrieval approaches used in coherent diffraction imaging (CDI), it offers a direct, non-iterative route to phase recovery by encoding spatial information into a measurable hologram [121, 122].

In the context of X-ray imaging, it employs highly coherent soft or hard X-ray sources, such as synchrotrons or XFELs, to probe nanoscale objects. A typical experimental setup involves placing the sample near a reference scatterer—often a

pinhole or a thin metallic film—on a substrate. The interference between waves scattered by the object and the reference is captured in the far field and numerically back-propagated to retrieve the object image [122]. This configuration bypasses complex optics and is well suited to imaging non-crystalline, weakly scattering biological samples.

A more recent development is free-flying Fourier holography, which eliminates the need for fixed substrates by allowing both the sample and reference scatterer to co-propagate in free flight [123]. It demonstrated this technique by introducing a nanoparticle reference alongside a biomolecular target, both suspended in a vacuum beam and illuminated by XFEL pulses. This innovation permits single-shot holographic imaging of isolated particles without mechanical supports.

Fourier transform holography presents a promising approach for single-particle imaging of small biological targets. It offers robustness to noise, non-iterative reconstruction, and flexibility in experimental geometry, all of which make it a powerful addition to the X-ray imaging toolkit.

2.3.5 Ptychography

Ptychography is a scanning coherent diffraction imaging (CDI) technique that enables high-resolution, quantitative phase and amplitude imaging of extended and non-crystalline samples. In this method, a coherent X-ray beam (the "probe") is scanned across the specimen in overlapping regions. At each position, a far-field diffraction pattern is recorded, and the set of these patterns is used to reconstruct both the complex transmission function of the sample and the illumination probe [124, 125].

A defining feature of ptychography is variable-position imaging: the probe is systematically translated across the sample with partial spatial overlap between adjacent scan positions. This redundancy in the dataset provides robust constraints during phase retrieval, improving convergence and resilience to noise [126]. Unlike holography, which relies on the addition of a known reference wave to recover phase information, ptychography reconstructs the phase by exploiting the multiplicative interaction between the probe function and the sample at each scan point.

Mathematically, the intensity measured at each scan position \mathbf{r}_i corresponds to the modulus squared of the Fourier transform of the exit wave:

$$I_i(\mathbf{q}) = \left| \mathcal{F} \left[P(\mathbf{r} - \mathbf{r}_i) \cdot O(\mathbf{r}) \right] \right|^2$$
(2.7)

where $P(\mathbf{r})$ is the complex probe function, $O(\mathbf{r})$ is the object transmission

function, and \mathcal{F} denotes the Fourier transform. By iteratively solving for both P and O using algorithm [126] or maximum likelihood optimization [127], a high-resolution image of the object can be reconstructed.

X-ray ptychography has been successfully applied in biological imaging to visualize subcellular structures, hydrated specimens, and cryo-preserved macromolecules with nanometer-scale resolution [128, 129]. Its combination of high spatial resolution, quantitative contrast, and compatibility with thick, weakly scattering specimens makes it a powerful technique.

2.3.6 Holographic SPI

Holographic SPI builds upon SPI by introducing a known, strongly scattering reference—such as a gold nanoparticle—positioned near the target biomolecule. This reference produces an interference pattern with the scattered wave from the sample, effectively encoding relative phase information into the far-field diffraction pattern [35, 36, 122].

Unlike ptychography, which uses a multiplicative interaction between the probe and object across overlapping scan positions, holographic SPI is fundamentally additive: the complex exit wave is a coherent sum of the target and reference contributions. This additive formulation allows the resulting diffraction pattern to directly encode cross-interference terms that carry phase-sensitive information about the weakly scattering object.

A distinctive advantage of holographic SPI is that it naturally provides multiple views of both the reference and target object. This redundancy forms a rich dataset that significantly enhances signal-to-noise ratio and supports robust phase retrieval without requiring an explicit support constraint, which is typically essential in conventional SPI [36]. Optimization algorithms can exploit these multiple views to iteratively reconstruct the complex-valued Fourier transform of the object, even under noisy or undersampled conditions.

Conceptually, holographic SPI is a hybrid of three imaging paradigms: X-ray SPI, Fourier transform holography, and ptychography. From SPI, it inherits the ability to image isolated particles without crystallization; from fourier transform holography, the use of a reference to enable phase recovery; and from ptychography, the principle that phase information can be retrieved from multiple views of the same object, although here those views are obtained holographically, rather than through scanning. The holographic principle ensures that the exit wave encapsulates complete structural information of the target object, and its reconstruction is

facilitated by the interference with the known reference wave.

The total electron density of the sample-reference system is expressed as:

$$\rho(\mathbf{r}) = \rho_o(\mathbf{r}) + \rho_{Ref}(\mathbf{r} - \mathbf{t}) \tag{2.8}$$

The measured diffraction intensity becomes:

$$I(\mathbf{q}, \mathbf{t}) = |F_o(\mathbf{q}) + F_{Ref}(\mathbf{q})e^{i2\pi\mathbf{q}\cdot\mathbf{t}}|^2$$
(2.9)

Expanding this yields the crucial interference term:

$$I(\mathbf{q}, \mathbf{t}) = |F_o(\mathbf{q})|^2 + |F_{Ref}(\mathbf{q})|^2 + 2\operatorname{Re}\left[F_o(\mathbf{q})F_{Ref}^*(\mathbf{q})e^{i2\pi\mathbf{q}\cdot\mathbf{t}}\right]$$
(2.10)

When the reference dominates scattering ($|F_{Ref}| \gg |F_o|$), the signal-to-noise ratio (SNR) simplifies to:

$$SNR(\mathbf{q}) \approx 2|F_o(\mathbf{q})| \tag{2.11}$$

This reflects a twofold SNR advantage over standard SPI [35], significantly boosting detectability of weakly scattering biological specimens. Holographic SPI, through this fusion of techniques, provides a powerful framework for imaging isolated biomolecules with high sensitivity and phase fidelity.

2.4 Reconstruction Algorithm

SPI seeks to reconstruct the 3D electron density, $\rho(\mathbf{r})$, of nanoscale biological specimens from a collection of noisy 2D diffraction patterns. Each pattern captures the squared modulus of the particle's Fourier transform, projected at an unknown orientation and subject to varying X-ray fluence. The reconstruction process therefore involves solving a high-dimensional latent variable inference problem, followed by phase retrieval to recover real-space structure.

The overall workflow consists of (1) modeling hidden variables such as particle orientation and pulse fluence, (2) applying the Expectation-Maximization-Compression (EMC) algorithm to estimate the 3D intensity distribution in reciprocal space, and (3) retrieving the phase to reconstruct real-space electron density.

2.4.1 Latent Variables and Forward Model

Each recorded diffraction pattern is influenced by several latent parameters that must be inferred:

- Orientation $\Omega \in SO(3)$: the unknown 3D rotation of the particle at the time of X-ray exposure.
- **Fluence** φ : the variable intensity of the incident X-ray pulse for each pattern.
- **Detector mapping**: transformation of detector pixels to points in reciprocal space on the Ewald sphere [7].

In holographic SPI, additional latent parameters include the reference particle's properties, such as size or position relative to the object.

The measured photon counts K_{dt} at detector pixel t for pattern d are modeled as Poisson-distributed with mean $\varphi_d W_{rt}$, where W_{rt} is the model intensity at orientation r:

$$P(K_{dt}|W_{rt},\varphi_d) = \frac{(\varphi_d W_{rt})^{K_{dt}} e^{-\varphi_d W_{rt}}}{K_{dt}!}$$
(2.12)

This probabilistic framework supports joint inference over model intensities, orientations, and fluence values.

2.4.2 Expectation-Maximization-Compression (EMC)

The EMC algorithm [4, 7] is an iterative method designed to estimate the 3D reciprocal-space intensity distribution from randomly oriented 2D snapshots. It alternates among three core steps:

- **E-step (Expansion)**: Project the current 3D intensity model onto detector planes for all sampled orientations.
- **M-step (Maximization)**: Update the orientation probabilities and model parameters by maximizing the expected log-likelihood of the observed data.
- **C-step (Compression)**: Integrate the updated projections back into a single 3D intensity model, maintaining consistency.

The overall model update at iteration (t + 1) can be expressed as:

$$W^{(t+1)} = C \circ M \circ E \left[W^{(t)} \right] \tag{2.13}$$

Fluence correction is incorporated by estimating a per-pattern scale factor:

$$\varphi_d^{\text{new}} = \frac{\sum_{r,t} P_{dr} K_{dt}}{\sum_{r,t} P_{dr} W_{rt}}$$
 (2.14)

The updated intensity model becomes:

$$W_{rt}^{\text{new}} = \frac{\sum_{d} P_{dr} K_{dt}}{\sum_{d} P_{dr} \varphi_{d}}$$
 (2.15)

This approach allows robust inference even under noisy and highly variable imaging conditions, making EMC a powerful algorithm for SPI data analysis.

2.4.3 Phase Retrieval

Once the 3D Fourier intensity model has converged, the next step is to recover the real-space electron density $\rho(\mathbf{r})$ by solving the phase problem—i.e., recovering the phase of the complex-valued Fourier transform from its squared modulus.

Phase retrieval is an ill-posed inverse problem and is typically addressed using iterative algorithms such as: (i) Hybrid Input-Output (HIO) [114], Difference Map (DM) [115] and Shrinkwrap [130].

These algorithms alternate between real-space and reciprocal-space projections, enforcing known constraints—such as positivity, compact support, and measured amplitudes—to iteratively refine the electron density.

2.4.4 Resolution

Resolution quantifies the level of structural detail recovered in the 3D reconstruction. In SPI, resolution depends on the signal-to-noise ratio and angular coverage of the diffraction data. Two common metrics are used for its estimation:

Fourier Shell Correlation (FSC): FSC compares the agreement between two independently reconstructed volumes in Fourier space:

$$FSC(q) = \frac{\sum_{\mathbf{q} \in \text{shell}} F_1(\mathbf{q}) \cdot F_2^*(\mathbf{q})}{\sqrt{\sum |F_1(\mathbf{q})|^2 \cdot \sum |F_2(\mathbf{q})|^2}}$$
(2.16)

The resolution is defined as the spatial frequency q at which the FSC drops below a threshold, commonly 0.143 or 0.5 [131].

Phase Retrieval Transfer Function (PRTF): PRTF evaluates phase consistency across independent reconstructions:

$$PRTF(q) = |\langle e^{i\phi(q)} \rangle| \tag{2.17}$$

where $\phi(q)$ is the recovered phase at spatial frequency q, and the average is taken over multiple reconstructions. PRTF values range from 0 (random) to 1 (perfectly consistent). Resolution is typically defined at the point where the PRTF falls below 0.5 or 1/e [13].

Together, FSC and PRTF provide quantitative measures of reconstruction fidelity, guiding the interpretation and validation of SPI results.

2.5 Machine Learning

Machine learning (ML) has emerged as a transformative approach for analyzing the vast and noisy datasets generated in SPI experiments. The high-throughput nature of modern XFEL and synchrotron facilities produces millions of diffraction patterns—many of which are noisy, heterogeneous, or corrupted by background. ML techniques are increasingly used to address challenges in pattern classification, denoising, heterogeneity modeling, and structural inference [132–136].

These data-driven approaches offer flexibility, scalability, and robustness in processing large-scale SPI datasets. By learning underlying data distributions, ML methods can extract structural insights that are difficult to access through purely algorithmic pipelines.

Classification

Accurate identification of usable diffraction patterns is a critical preprocessing step in SPI. Experimental datasets often contain a mix of single-particle hits, aggregates, multiple hits, and empty frames. Supervised learning models—particularly convolutional neural networks (CNNs)—have shown strong performance in classifying patterns into meaningful categories [137–139].

Beyond binary hit-finding, fine-grained classification techniques group patterns by properties such as orientation, sample composition, or scattering strength. Dimensionality reduction methods—such as principal component analysis (PCA) and t-distributed stochastic neighbor embedding (t-SNE)—are often used to visualize and cluster high-dimensional diffraction data [136, 140].

Unsupervised Learning and Heterogeneity Modeling

A major advantage of unsupervised learning in SPI is its ability to model continuous conformational variability and sample heterogeneity. Probabilistic models such as variational autoencoders (VAEs) enable low-dimensional representations of structural variation without requiring labeled data [36, 136, 141].

In a VAE framework [142], an encoder maps each diffraction pattern to a point in a latent space, while a decoder reconstructs the corresponding scattering distribution. Each point in the latent space represents a distinct structural state, allowing smooth interpolation between conformations. These models have been used to map conformational landscapes of flexible biomolecules such as viral capsids [132].

Incorporating physical constraints—such as known symmetry, Fourier transform properties, or estimated orientations—can improve reconstruction fidelity. Some models jointly learn latent coordinates and reconstruct full 3D intensity volumes in Fourier space. This enables direct recovery of heterogeneous 3D structures from unaligned, noisy data.

Emerging Methods

Recent work has explored amortized inference approaches to speed up the reconstruction process and reduce memory usage [143, 144]. These methods replace iterative optimization with fast, learned mappings from diffraction data to model parameters.

As SPI experiments continue to scale in size and complexity, ML-driven methods are expected to play an increasingly central role in structure determination. By integrating machine learning with traditional reconstruction pipelines, one can efficiently handle heterogeneous datasets, identify rare conformational states, and push the limits of resolution and throughput in SPI.

3

SPI of Dehydrating Viral Capsids

≺ The majority of the content in this chapter is adapted from the manuscript titled *Observation of Aerosolization-induced Morphological Changes in Viral Capsids* [132], co-authored by Anna Munke, Zhou Shen, Parichita Mazumder, Johan Bielecki, Juncheng E, Armando Estillore, Chan Kim, Romain Letrun, Jannik Lübke, Safi Rafie-Zinedine, Adam Round, Ekaterina Round, Michael Rütten, Amit K. Samanta, Abhisakh Sarma, Tokushi Sato, Florian Schulz, Carolin Seuring, Tamme Wollweber, Lena Worbs, Patrik Vagovic, Richard Bean, Adrian P. Mancuso, Ne-Te Duane Loh, Tobias Beck, Jochen Küpper, Filipe R.N.C. Maia, Henry N. Chapman, and Kartik Ayyer. ≻

Authors Contributions:

K.A. conceived the project. Samples were prepared by A.Mu. Cryo-EM data collection and analysis was performed by A.Mu. with the assistance of C.S.. All authors except C.S. performed the XFEL experiment. P.M. performed the molecular dynamics simulations. The diffraction data was analysed by A.Ma., S.Z. and K.A. with the help of P.M. and T.W. K.A., A.Ma. and P.M. wrote the manuscript with input from all authors.

3.1 Abstract

Single-stranded RNA viruses co-assemble their capsid with the genome and variations in capsid structures can have significant functional relevance. In particular, viruses need to respond to a dehydrating environment to prevent genomic degradation and remain active upon rehydration. Theoretical work has predicted

low-energy buckling transitions in icosahedral capsids which could protect the virus from further dehydration. However, there has been no direct experimental evidence, nor molecular mechanism, for such behavior. Here we observe this transition using X-ray single particle imaging of MS2 bacteriophages after aerosolization. Using a combination of machine learning tools, we classify hundreds of thousands of single particle diffraction patterns to learn the structural landscape of the capsid morphology as a function of time spent in the aerosol phase. We found a previously unreported compact conformation as well as intermediate structures which suggest an incoherent buckling transition which does not preserve icosahedral symmetry. Finally, we propose a mechanism of this buckling, where a single 19-residue loop is destabilized, leading to the large observed morphology change. Our results provide experimental evidence for a mechanism by which viral capsids may protect themselves from dehydration upon aerosolization. In the process, these findings also demonstrate the power of single particle X-ray imaging and machine learning methods in studying biomolecular structural dynamics.

3.2 Introduction

Viral capsids assemble optimally to prioritize the protection and efficient packaging of the genome [53, 60]. It ensures the survival of the virus and facilitates interactions with a host to maintain infectivity. Most spherical viruses in nature assemble their capsids with icosahedral symmetry, characterized by a triangulation number (T): the number of structural subunits forming the triangular facets of the icosahedron [42]. For instance, the MS2 bacteriophage, a 27 nm single-stranded RNA virus infecting *Escherichia coli* bacteria (*E. coli*), is a non-enveloped virus with a T=3 icosahedral capsid structure [44]. With non-genomic RNA, the capsid protein can also assemble into T=4 as well as hybrid capsids between these two triangulation numbers [145]. Furthermore, covalent dimerization of the coat protein in MS2 can lead to an octahedral structure under certain buffer conditions [146].

The variability in capsid structures and symmetry breaking in icosahedral capsids can potentially affect infectivity, and has been well-studied in the context of viral maturation [60]. The shape of the capsids is determined by elastic properties such as stretching and bending energies, spontaneous curvature, and chirality. The transition from smooth to faceted shapes in icosahedral capsid shells corresponds to a soft-mode buckling transition, driven by bending stiffness [147]. Continuum elasticity theory attributes shape transitions in capsids with non-icosahedral symmetries to a trade-off between stretching and bending energies [148]. Moreover, the

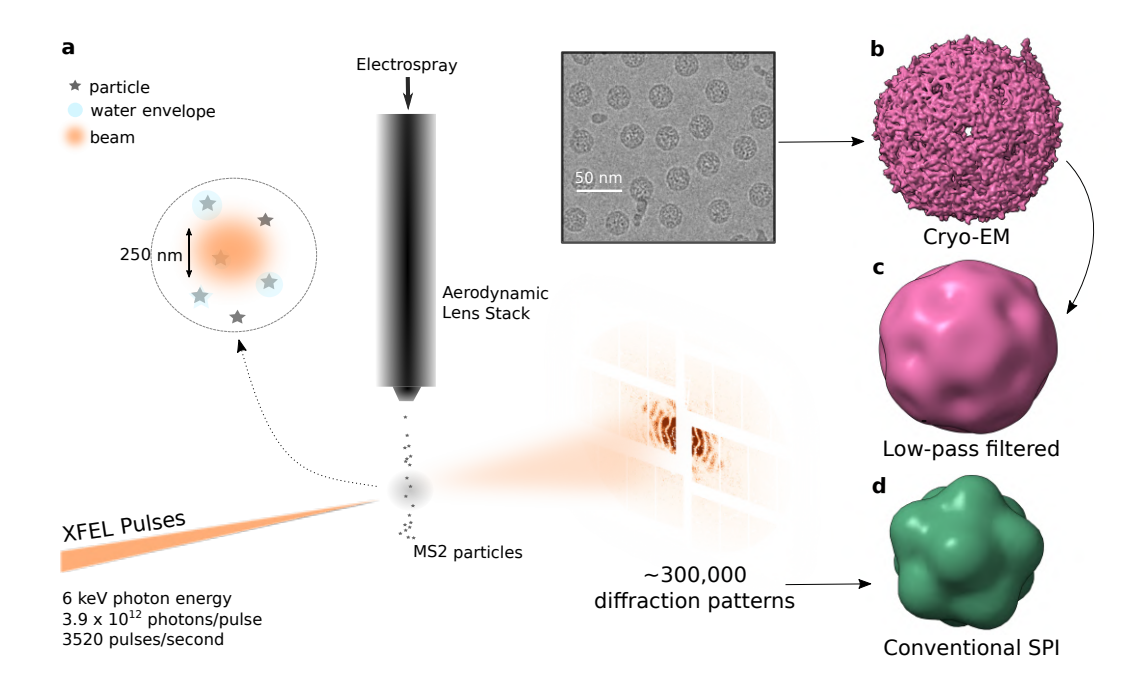


Figure 3.1: **X-ray SPI Experiment.** (a) MS2 bacteriophage particles, \sim 27 nm in diameter, were aerosolized using an electrospray and focused with an aerodynamic lens stack to the interaction region within the X-ray beam of $250\times250\,\mathrm{nm}^2$ focus. The top inset shows a representative cryo-electron microscopy (cryo-EM) micrograph of the particles. (b) The 3D structure of MS2 capsid determined by cryo-EM (resolution $0.49\,\mathrm{nm}$), served as the control for the subsequent X-ray SPI experiment. (c) The same cryo-EM structure was low-pass filtered to the resolution of the conventional X-ray SPI structure. (d) The structure retrieved from diffraction data (6.1 nm resolution) using the conventional analysis pipeline is notably different from the cryo-EM structure in (c).

elastic responses to external forces elucidate the mechanical stability and rupture behavior of both empty and filled viral capsids [149].

Understanding the intricate and non-trivial variations in viral capsid structure is essential for unraveling the fundamental processes driving viral infectivity and hardiness. In this study, we approach this problem using the emerging technique of single particle imaging (SPI) at an X-ray Free Electron Laser (XFEL) source. This is a powerful method for probing the structures of nanoscale systems [10, 113, 134]. In these experiments, extremely bright, ultrashort and coherent X-ray pulses from XFELs interact with copies of isolated single particles in random orientations one at a time. This process generates millions of diffraction patterns, each from a single viral particle. Machine learning approaches, including unsupervised methods [136, 150], are employed to identify diffraction patterns scattered from the target object amid contaminants, aggregates and outliers. This is followed by orientation

determination and phase retrieval to obtain the electron density of the average particle [7, 133, 151]. Since each measurement is made on an individual particle, one additionally has the opportunity to classify them and obtain not only the average structure, but also the landscape of structural variations [10, 134, 136, 152].

The short pulses of an XFEL also enable time-resolved SPI experiments to investigate ultrafast phenomena and structural dynamics in ensembles of particles at the nanoscale. This progression has enabled the exploration of ultrafast photo-induced dynamics [153], resolving the non-equilibrium shape distributions [134], retrieving the 3D morphology of polyhedral particles [154], melting to explosive disintegration of nanoparticles [155], demonstrating diffraction before destruction at the protein scale [156] and retrieving structures of heterogeneous nanoparticles [10].

In this work, we explore and analyze the structural dynamics of MS2 bacteriophage viruses after aerosolisation. In the process of being transported to the XFEL beam, the aerosol droplets are continuously drying, simulating the natural dehydration process [157–159]. Dehydrated viruses have been the target of studies since the earliest days of macromolecular structural studies [160]. These studies used electron microscopy [161] and crystallography [162] to study dried virus crystals, reporting a reduction in the diameter compared to the hydrated case, but still with a symmetric structure. This still left the question open about the structure of the intermediate stages during dehydration, and the possibility that asymmetries and heterogeneity introduced by the drying process were averaged over. Another approach applied to study dehydrated viruses is using atomic force microscopy (AFM) [163, 164]. These studies showed mostly icosahedral structures and in certain cases, structures resembling those that have been produced in wet conditions under high salt concentrations.

In the current experiment, the aerosolized particles are probed using the XFEL at random degrees of dehydration to produce single particle diffraction patterns. Using a combination of maximum likelihood and deep learning techniques, we map the collected diffraction data from the ensemble of MS2 capsids to a continuous structural landscape. One can then observe viral capsid structures ranging from the fully-hydrated state to a previously unobserved capsid form with full coverage of intermediate structures. This data then enabled us to hypothesize a molecular mechanism for the observed conformational changes, which seems to apparently protect the genome from further dehydration. In the process, we also show how the combination of machine learning methods with high-throughput SPI measurements at XFELs can be used to understand the conformational landscape and dynamics of biomolecules in a fairly general manner.

3.3 X-ray SPI Experiment

Data was collected at the SPB/SFX (single particles, clusters and biomolecules & serial femtosecond crystallography) instrument [165] of the European XFEL using $6\,\mathrm{keV}$ photons focused into a $250\times250\,\mathrm{nm^2}$ spot. Individual x-ray pulses were generated with $3.8\,\mathrm{mJ}$ of energy on average (3.94×10^{12} photons/pulse). The pulses were delivered in 352-pulse trains with an intra-train repetition rate of 1.1 MHz and trains arriving every 0.1 s, leading to a maximum data collection rate of 3520 frames/second. A detector built specifically for this burst mode operation, the Adaptive Gain Integrating Pixel Detector (AGIPD) [166], was placed 700 mm downstream of the interaction region to collect the diffraction patterns for each pulse individually up to a scattering angle of 13° at the corner of the detector.

MS2 bacteriophage particles in an aqueous buffer (sample preparation details in Supplementary Section 1) were aerosolised and sequentially injected into the X-ray beam interaction region using an electrospray-ionization aerodynamic-lens-stack sample delivery system [167], as shown in Fig. 3.1a. Diffraction patterns were collected at an average rate of 3520 frames/second for an integrated collection time of $3.6\,\mathrm{h}$ with a hit ratio of around 0.7%. Frames with diffraction from particles were detected by setting a threshold on the scattered signal. A total of $287\,168$ potential hit diffraction patterns were identified containing 4873 photons per pattern on average in the resolution range of $48\,\mathrm{nm}$ to $3\,\mathrm{nm}$. The average non-hit frame contained 1014 photons in the same range.

The highly noise-tolerant EMC algorithm [4] can be used to categorize and orient diffraction frames with only a few photons [133, 168, 169]. We employed the *Dragonfly* software [7], to perform two-dimensional (2D) classification using this algorithm. This procedure generated multiple 2D intensity models of diffraction patterns in the detector plane [10] by determining the in-plane rotation angle and relative incident fluence of each diffraction pattern. These 2D reciprocal space intensity models capture the average of aligned copies of a subset of patterns from the entire dataset, following which class averages were manually selected corresponding to single particles, indicated by high fringe contrast and a convex envelope. This procedure was then repeated, each time rejecting the various contaminants like aggregates and other outliers (details in Supplementary Section 3).

The final selection contained intensity models revealing distinctive diffraction features corresponding to an icosahedral particle with good contrast and sharp streaks. The subset of diffraction frames associated with this intensity model was selected to reconstruct a three-dimensional (3D) Fourier model using *Dragonfly*.

Icosahedral symmetrization was applied due to the subset having only 7249 patterns. Subsequently, it was phased to retrieve the electron density of the MS2 capsid, as shown in Fig. 3.1d, with an estimated resolution of $6.1 \, \mathrm{nm}$ (phase retrieval parameters in Supplementary Section 4).

Even at this resolution, this structure is markedly different from the one obtained using cryo-electron microscopy (cryo-EM) on the same sample batch shown in Fig. 3.1b. This structure at $0.49\,\mathrm{nm}$ resolution provides insight into the conformation of the hydrated, flash-frozen capsid, which is a near-spherical particle with icosahedral symmetry (see Supplementary Section 2 for details). This baseline structure, along with the similar crystallographic structure of the capsid (PDB: 2MS2) [45] serves as a reference for interpreting structural changes induced by aerosolisation. The low-pass filtered version shown in Fig. 3.1c shows differences at both the 5-fold and 3-fold sites, with the X-ray structure indenting inwards at the 3-fold sites.

The fact that only a limited number of patterns (only 2.5%) went into the final 3D structure with the conventional X-ray SPI analysis pipeline raises the question of the structures of the rejected particles and the source of the heterogeneity. As the particles traverse through the low-humidity environment aerodynamic lens and then the vacuum environment of the interaction region, the surrounding water envelope is continuously evaporating. We explore the possibility of whether the rejected patterns contain information about the transition from the hydrated state to the final structure depicted in Fig. 3.1d.

3.4 Heterogeneity Analysis Workflow

Figure 3.2a shows the analysis workflow for learning the structural landscape of aerosolized MS2 capsids. By using a much larger fraction of the data, we can reconstruct not just a single homogeneous object, but a whole family of structures, and then to study the variations in that family. We first used the same 2D classification approach as for the single reconstruction above. In order to effectively train and utilize the deep learning method discussed below, we expanded the total number of intensity models by performing multiple runs of 2D classification. In each of the 100 independent bootstrapping runs, 20% of the diffraction frames (from a total of $170\,355$) were randomly selected and classified into 100 distinct 2D intensity models, resulting in $10\,000$ intensity models.

Upon scrutinizing the 2D intensity models, distinctive patterns emerged, including some with strong streaks in the detector plane from faceted particles but

also nearly circular diffraction rings from rounded objects. These observations hinted at particle shapes spanning from icosahedral to almost perfectly round. We applied size filtering on the 2D intensity dataset to retrieve distribution of different discrete heterogeneity in the MS2 particles. The effective size of the particles was determined from each intensity average using a spherical diffraction model [170] (see Supplementary Section 6).

We curated a dataset of 2558 2D intensity models from 79711 diffraction frames, representing particles with different capsid morphologies, but excluding models from dimers, aggregates and other contaminants whose nominal size was outside the 23-31 nm size range. To understand the structural landscape of the remaining particles, we employed an unsupervised deep learning approach – a variational autoencoder (VAE) network [142]. Inspired by the pioneering cryoDRGN approach using a VAE network to study heterogeneity in single-particle cryo-EM datasets [171] and our prior work on continuous shape transitions in gold nanoparticles [136], we adapted the network for our MS2 virion dataset as a β -VAE, described below.

An autoencoder consists of two components, the first of which (the encoder) takes the input data and returns a low-dimensional vector, termed the latent vector. The second part (the decoder) takes this vector as input, which could even be a single number, and reconstructs the input data. Both networks are simultaneously trained to minimize the difference between the inputs and corresponding outputs. By forcing this operation to go through this bottleneck, the encoder not only learns a low dimensional latent representation of the dataset, but the decoder can then be used to generate the data for arbitrary points in the latent space. A variational autoencoder further refines this approach by replacing the latent vector by a distribution, usually represented as the mean and standard deviation of a normal distribution. During training, instead of directly passing the estimate of the latent vector to the decoder, a random vector is sampled from the normal distribution parameterized by the encoded mean and standard deviation. The decoder has to figure out how to recover the input given a Gaussian neighborhood rather than a specific point in the latent space, which accommodates noise/uncertainties in the input and drives smoothness of the latent representation.

In SPI experiments, not only are there unknown structural and orientation parameters, but the measurements are also incomplete, since they are 2D images of 3D objects. Thus, we implement a 2D encoder which takes 2D diffraction images, but the decoder reconstructs a 3D intensity distribution. The loss function then compares the input with a slice through this 3D intensity at the estimated orientation. In order to separate the effect of true structural variations from the large, but trivial,

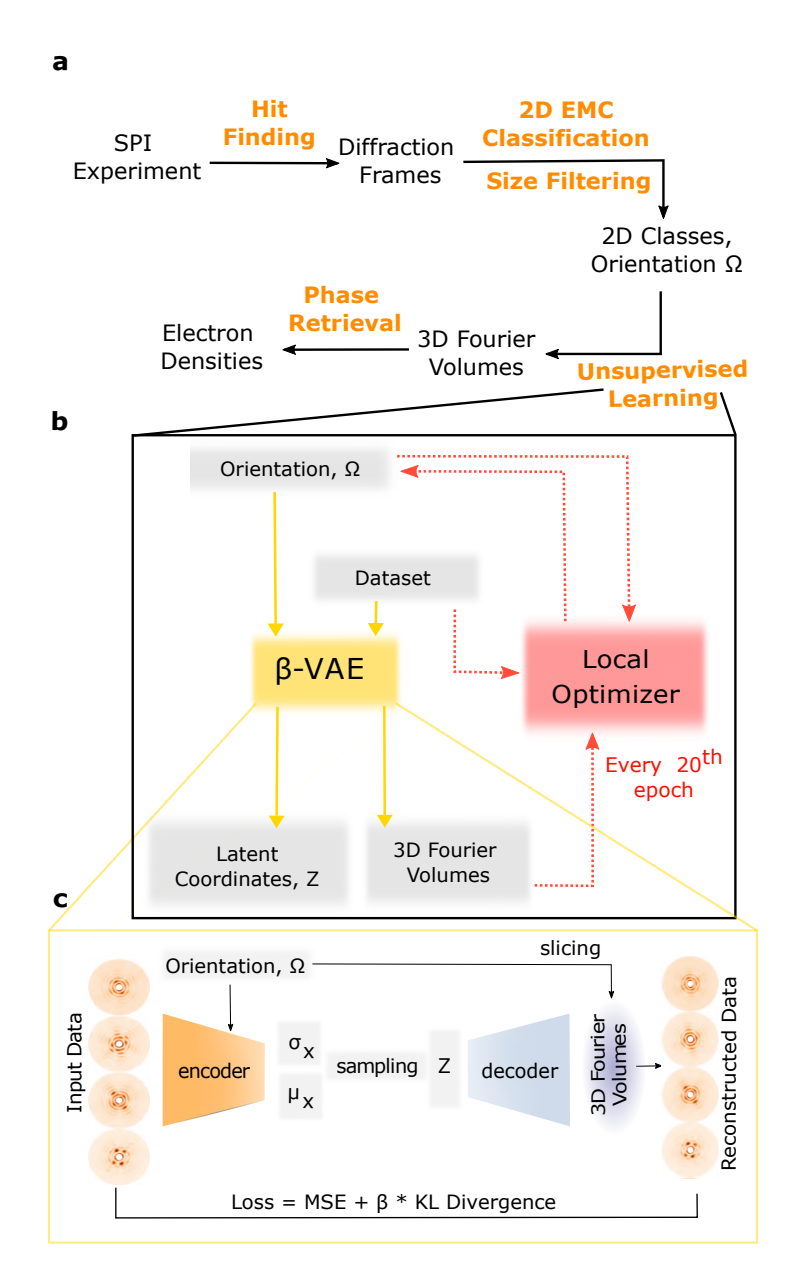


Figure 3.2: **Analysis Pipeline.** (a) Schematic of diffraction data analysis workflow. All steps other than the unsupervised learning ones are part of the standard SPI workflow. (b) Detailed flow chart of the unsupervised learning step to generate the structural latent space and associated 3D Fourier intensity volumes. The pipeline involves training a β -VAE with a local orientation optimizer. Every 20^{th} epoch, the optimizer outputs an improved estimate for the orientation (Ω) given the 3D Fourier volumes, dataset, and the current estimate of the orientations. (c) Schematic representation of the β -VAE network. The model takes 2D class-average intensities and orientations as input and encodes them into a latent space via an encoder network. This latent space coordinate (Z) is subsequently utilized by a decoder network to reconstruct 3D Fourier volumes.

variations in diffraction patterns of differently oriented particles, we include the quaternion representation of the estimated orientation (Ω) for every 2D intensity model in the dense layers of the encoder network (see Fig. 3.2c). In the decoding process, after sampling the latent vector, the decoder reconstructs a 3D Fourier volume, which is then sliced at Ω to retrieve the input intensities as reconstructed output data. Finally, the β part of the β -VAE is a method to regularize the latent space to avoid overfitting. This allows the network to use information from patterns in different orientations with slightly different structures. The description of the network architecture as well as the analysis workflow to refine the orientation estimates is detailed in Fig. 3.2b and the Supplementary Sections 5 and 7.

As an initial estimate, the orientation of each of these 2D intensity class averages was determined against a single 3D Fourier volume of the icosahedrally symmetrized MS2 bacteriophage from the conventional SPI reconstruction (Fig. 3.1d). These orientation estimates were incrementally updated using a so-called Local Optimizer, which works as follows. After a given epoch, each input data frame was used to generate a 3D Fourier volume using a single pass through the VAE. This volume was sliced multiple times, using orientations which were slightly different from the current estimate (standard deviation of $5~\rm mrad$ or 0.3°). The updated orientation for this frame was chosen to be the one which maximized the Pearson correlation coefficient with the data (see Supplementary Section 7 for details). This pipeline is shown schematically in Fig. 3.2b.

For this dataset, the β -VAE was trained over a total of 2000 epochs. In the first 1000 epochs, the Local Optimizer was turned off, and icosahedral symmetric orientation estimates were used, allowing the VAE to learn features from the dataset and stabilize itself. In the later 1000 epochs, the orientations were updated.

Once trained, the β -VAE network enables detailed analysis and systematic exploration of structural heterogeneity by examining the 3D intensity volumes reconstructed by the decoder for various points in the latent space. The effective diameter of each 3D volume was determined by fitting a sphere model, the result of which is shown in Fig. 3.3a where the two components of the latent vector mean, μ_1 and μ_2 are represented along the axes and the color and height represent the effective diameter.

3.5 Structural landscape

We highlight two paths through the structural landscape shown in Fig. 3.3a, capturing two salient features of the evolution of the capsid morphology. Firstly, the dotted

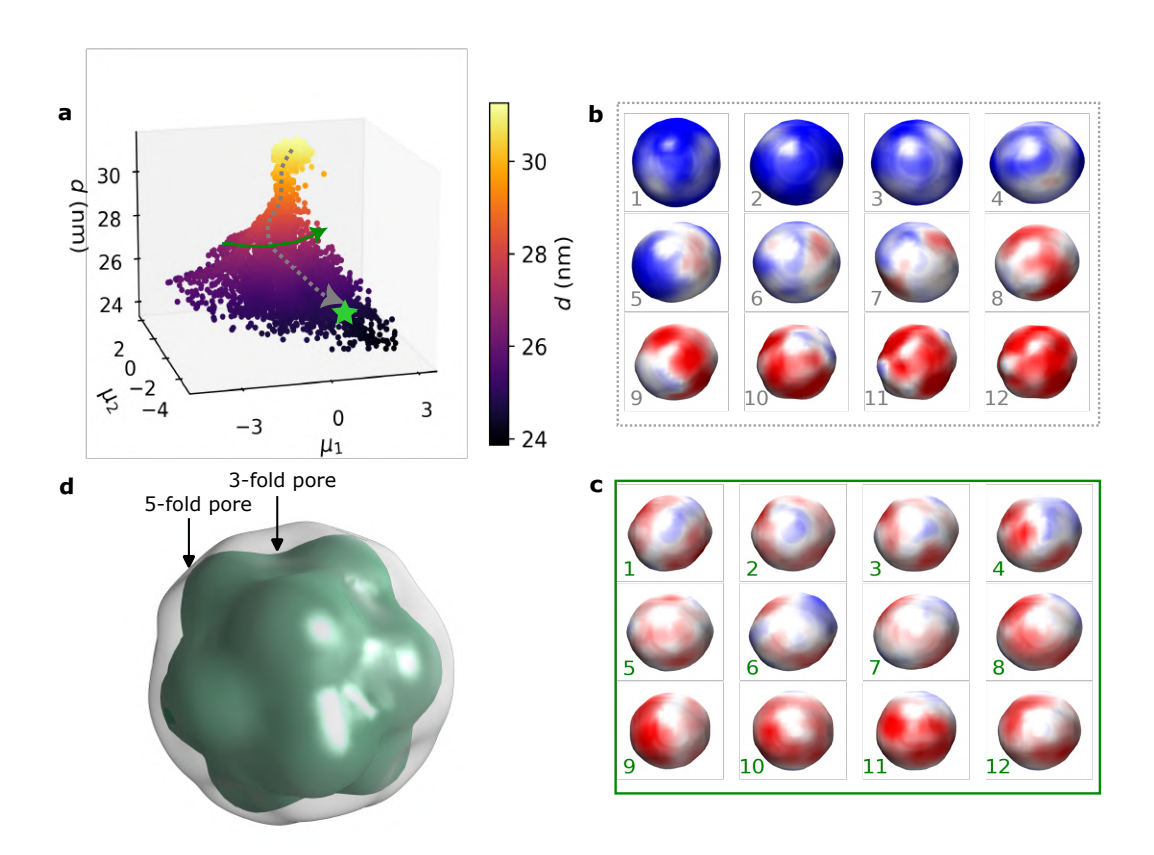


Figure 3.3: **Structural Landscape.** (a) The latent space learned by the β -VAE colored by the estimated diameter (d) of individual patterns. The plot highlights two distinct trajectories selected to capture the structural variation phenomenon within the latent space. The retrieved electron density of MS2 particles via phase retrieval of Fourier volumes generated by decoder network of β -VAE network is shown in the grid. (b) The dotted Gray trajectory, following from top to bottom in (a), depicts the shape-size variation in the ensemble of capsids. (c) The Green trajectory, progressing from left to right in (a), corresponds to different shape realizations for a fixed size of capsid. Red-white-blue colored radially. (d) Encapsulated overlay of the 3D structure of the MS2 capsid from the low-pass filtered cryo-EM reconstruction (gray) and the dehydrated X-ray SPI reconstruction (green). The overlap highlights the altered conformations in the vicinity of the 5-fold and 3-fold sites.

Gray line trajectory illustrates the variation in shape and size, as observed from top to bottom, which we ascribe to the effect of dehydration. Three-dimensional structures of the MS2 capsids along this path are depicted in Fig. 3.3b. Following this path, we note a transition from larger particles to smaller, nearly icosahedral particles as dehydration progresses. The largest particles (29-31 nm) were nearly spherical and larger than the reported 27 nm hydrated structure, representing MS2 capsids with a water envelope around them. The contour images in Fig. 3.3b and c are color-coded radially from red to white to blue in order to ease visualization of facets, curvature, and size changes. The structure in Fig. 3.1d, reconstructed without the VAE, lies at the end of this path and is highlighted by a star in the landscape.

The second, *Green*, trajectory is shown in Fig. 3.3c. Along this path, all particles had an estimated diameter of 27 nm. Here, subtle and gradual deviations from the icosahedral shape at a constant size are observed. Close examination shows structures with varying degrees of deviation from the symmetric structure, also borne out by individual diffraction patterns and class averages showing asymmetric structures. This suggests that whatever morphological change is occurring, is not a coherent change acting on all icosahedral sites simultaneously, but seems to occur independently at each site.

3.6 Proposed molecular mechanism

In order to better understand the capsid morphology change, we focus on the fully dehydrated state and compare it to the MS2 capsid structures obtained from cryo-EM and crystallography. Figure 3.3d displays an overlay visualization of the two MS2 capsid structures: the low-pass filtered cryo-EM reconstruction and the X-ray SPI reconstruction. This overlay emphasizes the locations of the pores at the 5-fold and 3-fold sites (vertex and face center respectively), which are affected during dehydration through aerosolisation. The T=3 icosahedral capsid of MS2 consists of 12 5-fold contacts at the vertices and 20 6-fold contacts at the face-centers, as seen in the cryo-EM structures in Fig. 3.1b and c. The configuration of the coat protein creates a capsid shell featuring 32 pores (about 2 nm in diameter), denoted here as 5-fold and 3-fold pores, respectively.

The crystal structure of the MS2 virus capsid [45] shows that the coat protein has three possible conformations, termed A, B and C. These proteins assemble into two types of dimers: asymmetric A/B dimers and symmetric C/C dimers. Although the A, B, and C subunits (129 residues) are almost structurally identical, they differ

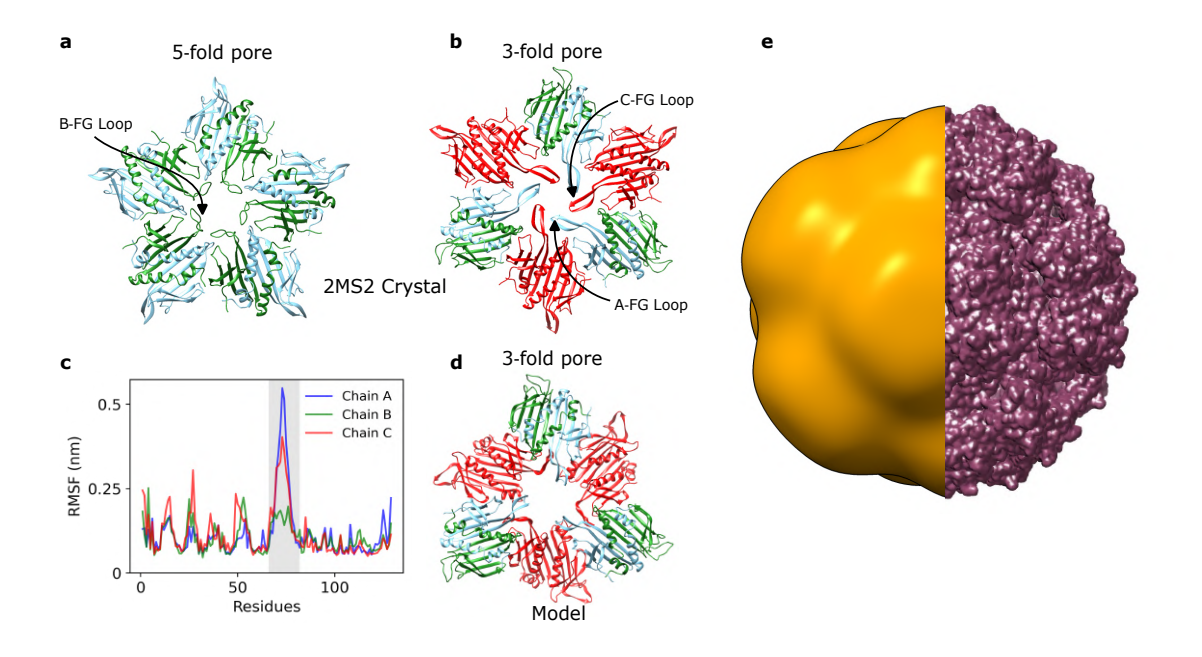


Figure 3.4: **Dehydrated capsid model.** (a-b) The pentameric (5-A/B) and hexameric (3-A/B and 3-C/C) faces of the T=3 icosahedral capsid shell from the 2MS2 PDB structure. At the 5-fold axis FG loops of B (B-FG loop, green, a), and at the 3-fold axis FG-loops of A (A-FG loop, sky blue, b) and C (C-FG loop, red) are crucial for capsid assembly and curvature. (c) The A-FG loop and C-FG loop exhibit significant fluctuations compared to B-FG loop (residues 66-82, shaded region). The Root Mean Square fluctuation (RMSF) was calculated from a 20 ns vacuum MD-trajectory of A/B and C/C dimers. (d) Transformed hexameric building block designed/modeled from the X-ray SPI map. At the 3-fold axis, C/C dimers move toward the capsid center. (e) Map generated from transformed capsid model (at 6.1 nm resolution). The left half is in a similar representation as the experimental X-ray SPI map (Fig. 3.1d) for visual comparison.

in the conformation of the FG-loop (residues 66-82), with the A and C subunits exhibiting a conformation that is different from that of the B subunit.

The 5-fold pores consist of 5 A/B dimers, with the FG-loops of the five B-subunits oriented towards the pores in a compact conformation, as depicted in Fig. 3.4a. The 3-fold pores are formed by six dimers–3 A/B and 3 C/C–arranged alternately, with 3 FG-loops from each A and C subunit in an extended conformation (Fig. 3.4b). The FG-loop plays a pivotal role in capsid assembly and affects its curvature and mutations in this region can disrupt assembly [172].

We performed molecular dynamics (MD) simulations of the A/B and C/C dimers in vacuum conditions similar to those during sample delivery of the SPI experiment (see Supplementary Section 9 for details). The FG-loop of A and C subunits showed notable conformational changes or movements compared to the FG-loop of B on

a nanosecond timescale (marked in gray in Fig. 3.4c). The dehydration primarily affects the FG-loop of A and C [61, 173], suggesting a strong role for water molecules in stabilizing the extended form of the FG-loop around the 3-fold pore. In addition, mass spectrometry observations hint that a section of the internal RNA stabilizes the A/B dimers of the capsid [174].

Based on these observations, we formulate a hypothesis that due to the high mobility of the FG-loops of A and C under dehydrating conditions, the FG-loops around the 3-fold pore contract upon losing stabilizing waters and the C/C dimer shifts towards the center of the virus. We utilized the positions of A, B, and C subunits from the asymmetric unit of the 2MS2 crystallographic model as a starting point, then adjusted the position of the C subunit (by translation and rotation) to form a new capsid assembly and minimized the energy of the entire capsid model in vacuum conditions. This procedure was iterated until we obtained a stable capsid shell model which also fit our SPI electron density map, shown in Fig. 3.4d. Figure 3.4e shows the full capsid with the modeled pore structure. The left half shows the low-pass filtered electron density map showing a remarkable similarity to the experimental map in Fig. 3.1d.

3.7 Discussion

The structural response of viruses to a dehydrating environment is an important, and somewhat understudied question, limited by the inability to study these systems *in situ* under these conditions. Single particle imaging using XFELs provides a unique opportunity to probe the structures of these viral capsids while they are dehydrating in an aerosol stream. With the use of machine learning tools to classify the whole ensemble of observed particles, one can observe complex conformational trajectories which would be hidden with other ensemble-averaged measurements. The femtosecond XFEL pulses allow one to temporally freeze the structural transitions and observe non-equilibrium, intermediate structures that occur during dehydration.

In this work, we apply this method to MS2 bacteriophage capsids, where we observe 3D structures ranging from a well-hydrated particle with a liquid envelope down to a dehydrated structure, with a different capsid morphology. Not only do we see these endpoints, but also a large number of intermediate conformations which break icosahedral symmetry, providing clear evidence for a site-specific transformation rather than a capsid-wide concerted change. However, it remains an open question how similar the dynamics are for aerosolized viruses at room

temperature and ambient pressure. The success of native mass spectrometry studies under harsher conditions than applied in this work suggest that these dynamics may not be wholly foreign [175].

While this study is limited to a moderate resolution, the large scale changes in this system are already clearly apparent. Upcoming technical improvements promise to push this resolution barrier to sub-nm levels [35, 176]. This work also opens up the possibility of studying this important question for aerosol-transmitted pathogenic viruses.

Acknowledgments: We acknowledge European XFEL in Schenefeld, Germany, for provision of X-ray free-electron laser beamtime, proposal 2734, at SPB/SFX SASE1 and would like to thank the staff for their assistance. This work is supported by the Cluster of Excellence-CUI: Advanced Imaging of Matter' of the Deutsche Forschungsgemeinschaft (DFG) - EXC 2056 - project ID 390715994, the Swedish Research Council (2018-00234 and 2019-06092) and the Carl Tryggers Stiftelse för Vetenskaplig Forskning (CTS 19-227). We thank Ilme Schlichting for useful discussions.

4

AuNP-enhanced Holographic-SPI

≺ The majority of the content in this chapter is adapted from the manuscript titled: Holographic Single-Particle Imaging for Weakly Scattering, Heterogeneous Nanoscale Objects [36], co-authored by Kartik Ayyer.
 ≻

Author Contributions:

K.A. conceived the project. The data generation and reconstruction code was developed by A.M. and K.A. K.A. and A.M. wrote the manuscript.

4.1 Abstract

Single particle imaging (SPI) at X-ray free electron lasers (XFELs) is a technique to determine the 3D structure of nanoscale objects like biomolecules from a large number of diffraction patterns of copies of these objects in random orientations. The technique has been limited to relatively low resolution due to background noise and heterogeneity of the target particles. A recently introduced a reference-enhanced holographic SPI methodology uses strongly scattering holographic references to improve background tolerance and thus, the achievable resolution, at the cost of additional latent variables beyond orientation. Here, we describe an improved reconstruction algorithm based on maximum likelihood estimation, which scales better, enabling fine sampling of latent parameters to reach high resolutions, and much better performance in the low signal limit. Furthermore, we show that structural variations within the target particle are averaged in real space, significantly improving robustness to conformational heterogeneity in comparison to conventional SPI. With these computational improvements, we believe reference-enhanced

4.2 Introduction

Single particle imaging (SPI) experiments leverage X-ray free electron lasers (XFELs) to investigate the structure and dynamics of biological entities in their near-native state [92]. The ultrashort X-ray pulses enable the study of ultrafast structural dynamics in biological samples such as proteins and viruses at room temperature via diffraction before destruction [13], and without the need to freeze samples. Many XFEL pulses with high flux and spatial coherence diffract from unknown target objects one at a time, in random orientations to collect millions of diffraction patterns. These are then computationally aligned and merged to reconstruct the 3D structure of the object [177].

This analysis often broadly follows the following three steps: First, diffraction patterns containing signal from spurious contaminants, multiple particle aggregates and other outliers are identified and removed using some machine learning framework [10, 178]. The rest of the patterns each represent a tomographic slice through the target object's 3D Fourier transform, albeit without the Fourier phases. The second step in the analysis pipeline is to align and average these patterns to obtain the 3D distribution of Fourier magnitudes [4, 7]. Finally, iterative phase retrieval methods are used to recover the structure of the particle from these oversampled magnitudes, possibly with some background subtraction [115, 133, 179, 180].

SPI has been used successfully in imaging samples in the 100-nm size range since they have high scattering cross section in comparison to the background, hence yielding high quality diffraction patterns [8, 151, 180]. However, for smaller particles, signal levels are much lower and extraneous background can severely hinder the alignment process. And while reconstruction algorithms are remarkably tolerant to low signal levels [4, 133, 168], background often poses a fundamental limit on the achievable resolution since the diffraction signal from a compact object falls off very quickly with increasing momentum transfer but the background usually does not [31].

Various sample delivery methods have been used to deliver samples to the X-ray beam focus each balancing the requirements of maximizing efficiency (hit rate) with minimizing background. Aerosol sample delivery has low background signal but has a relatively low particle density, leading to low hit fractions [9, 167]. Liquid-jets and solid substrates can be used as carrier media to increase the hit ratio [12, 181–184] but each hit now also has substantial signal from medium that

obscures signal from the sample and limits orientation determination. With the advent of high repetition rate XFELs [185], even with the low hit rates of aerosol methods, one can still collect millions of patterns in a day [10]. Nevertheless, even here, the background from the carrier gas of the aerosol and from detector false positives still produces sufficient background to limit the resolution to around 2 nm.

Recently, a reference-enhanced SPI [35] technique was introduced, based on the holographic principle. The approach suggests attaching a strongly scattering particle to the target object to form a composite object. The references considered were a spherical gold nanoparticle (AuNP) and a 2D crystal lattice with unit cell size comparable to target object. The total scattered signal is increased for each shot when a reference is attached and the signal now becomes more tolerant to background. A reconstruction algorithm was also developed to analyze the diffraction patterns generated from such a system in order to recover unknown parameters beyond orientation resulting from shot-to-shot variations in the composition of the composite object.

This holographic SPI technique alleviates the problem of high sensitivity to extraneous background, but at the cost of additional computational complexity in recovering the structure from the data. The technique introduces additional degrees of freedom in the composite system, which are unknown parameters for each pattern in diffraction dataset. The algorithm now has to recover not only the unknown orientation of the target object but also these hidden (latent) parameters characterizing the properties of the reference and the relative displacement between the reference and the target object. For the composite system where the reference is a spherical AuNP, the reference can be specified by one parameter: its diameter D.

The previous work also introduced a reference-EMC algorithm [35] which is a modified version of the EMC algorithm [4, 7] that recovers these additional latent parameters and directly reconstructs the target object's complex Fourier transform and not just the intensities. However, as we will discuss in Section 4.3, this method has problems dealing with very weak patterns as well as scaling to fine parameter sampling required to reach a high resolution. In this work, we propose a phase retrieval algorithm for holographic-SPI based on maximum likelihood estimation via pattern search dubbed as MaxLP. MaxLP scales efficiently with sampling of latent parameters and total number of diffraction patterns in comparison with previously introduced *divide* and *concur* approach in the reference-EMC algorithm [186]. Additionally, we observe that it performs much better when the signal level is

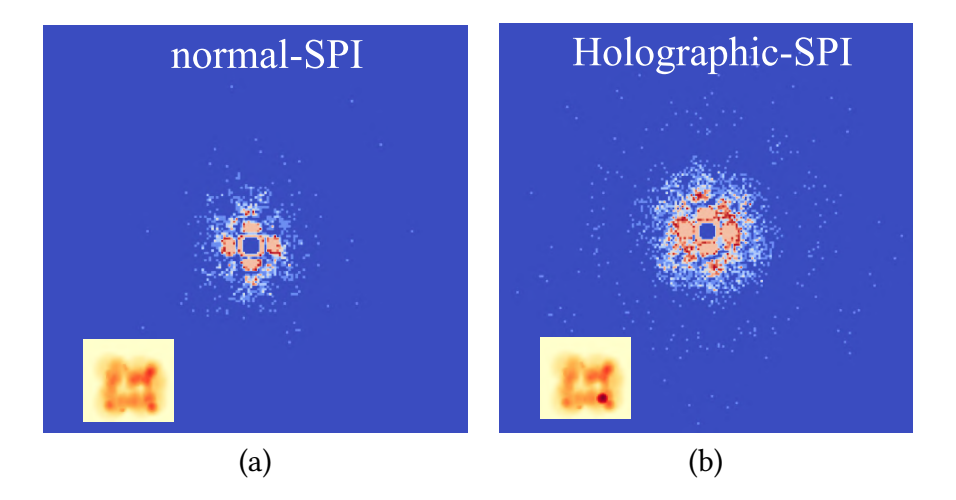


Figure 4.1: **Attached Reference Object.** (a) Simulated diffraction pattern contributed for a random object in a normal single-particle imaging (SPI) case with 4810 photons. (b) Diffraction pattern from the same particle with a small AuNP attached (10,000 photons). If background is present, structural information can be discerned at higher scattering angles in the holographic case. Insets show the true projected electron density of the objects.

low. The algorithm is described in Section 4.3 and its performance is shown with simulated data in Section 4.4.1.

We also discuss the performance of the holographic-SPI method with the MaxLP algorithm in the case where the target object itself is heterogeneous. In conventional SPI, this heterogeneity would have to be classified shot-by-shot before averaging since averaging intensities from variable structures can lead to meaningless results. Here, we show that in our approach, even without classification, we are able to reconstruct the average structure, making the process of handling conformational variations much more tractable. Thus, we find that this combination of the MaxLP algorithm with the holographic SPI experimental setup shows substantial promise in pushing the SPI technique to sub-nm resolution.

4.3 Reconstruction algorithm

In a holographic SPI experiment, the sample of interest (target object) is in the vicinity of a strongly scattering reference, which in this work, we take to be a spherical gold nanoparticle (AuNP). Large number of diffraction patterns of these conjugates are collected in order to reconstruct the 3D structure of the target object. This reconstruction process consists broadly of two steps, the first being the determination of the unknown, or latent, parameters for each pattern, followed

by a step to recover the structure given the data with the estimated parameters, which include the orientation of the object and the relative position and structure of the reference. Fortunately, the structure of the spherical AuNP can be described by just one number, namely its diameter D. For illustrative purposes, we limit ourselves to a two-dimensional object with only one in-plane rotational degree of freedom. Within this space, for a homogeneous reproducible object, we have four latent parameters to solve for: unknown orientation θ , diameter of AuNP d and relative positions of AuNP and target object in x- and y- directions (t_x, t_y) . In the general case, there are three orientational and translational parameters each, but the structure of the problem remains unchanged. The electron density of the composite object $\rho(\mathbf{r})$ is the sum of electron densities of the spherical AuNP $\rho_s(\mathbf{r}, D)$ and the unknown target object $\rho_o(\mathbf{r})$

$$\rho(\mathbf{r}) = \rho_o(\mathbf{r}) + \rho_s(\mathbf{r} - \mathbf{t}, D), \tag{4.1}$$

where ${\bf t}$ is the relative shift of the centers of the two objects and D represents the diameter of spherical AuNP. The total intensity distribution on the far-field detector in each frame is then

$$I(\mathbf{q}, D, \mathbf{t}) = \left| F_o(\mathbf{q}) + F_s(\mathbf{q}, D) e^{2\pi i \mathbf{q} \cdot \mathbf{t}} \right|^2, \tag{4.2}$$

where the F terms represent the Fourier transform of electron densities, $F(\mathbf{q}) = \mathcal{F}[\rho(\mathbf{r})](\mathbf{q})$, and frame-by-frame shifts of the sphere transform to a phase ramp.

The simulated diffraction dataset contains of a large number of patterns defined by Eq. 4.2, each with random D and t parameters and rotated in-plane by a uniform random angle θ . These holographic intensities are then Poisson sampled with a given mean intensity level to generate the simulated photon counts per pixel. In Fig. 4.1, we see the effect of the spherical AuNP attached as a reference to the target object on a simulated pattern for a given set of latent parameters with the same effective incident fluence. In both patterns, the single-frame signal-to-noise ratio (SNR) is very low beyond the first few speckles. In conventional SPI, this is improved by aligning and averaging a large number of patterns as long as this alignment can be performed in the presence of background and sample heterogeneity. For the chosen AuNP size, the conjugates have on average twice as many total scattered photons with much of the excess in the higher order rings which improve the SNR in the presence of background at these resolutions, making hit detection significantly more effective. Larger AuNPs will scatter more strongly, but with lower contrast

along the diffraction rings. The radii and intensity modulations in these rings are relevant to solve for diameter of the AuNP and its relative position. In order to retrieve the target object's structure which is assumed to be common to all the intensities, the first step is to solve for the set of latent parameters for each diffraction pattern and retrieve $F_o(\mathbf{q})$.

A modified version of EMC algorithm (Ref-EMC) was developed for holographic SPI [35]. The conventional EMC algorithm involves three steps in each iteration: Expand, Maximize and Compress which iteratively update the 3D intensity model to one which has a higher-likelihood of generating the observed diffraction patterns. When the reference is attached, the optimal final model is not the intensity distribution of the composite assembly, but rather the complex Fourier transform of just the target object, $F_o(\mathbf{q})$. In the E-step of Ref-EMC, the latent parameter space is grid-sampled and predicted intensities are generated for each sample using the current estimate of $F_o(\mathbf{q})$. In the M-step, the noisy diffraction patterns are compared with these predicted intensities and a probability distribution over parameters for each pattern is calculated. This distribution is then used to update the predicted intensities for each sampled parameter vector. The final C-step needs to recover the optimal $F_o(\mathbf{q})$ consistent with this stack of these intermediate predicted intensities, one for each sampled parameter set. This separate reconstruction problem is somewhat reminiscent of ptychography where multiple intensities are generated from a common object by varying translations [129]. In this case however, the intensities are generated by coherent addition with a reference (Eq. 4.2) rather than by multiplication with a probe function. In Ref. [35], a divide and concur iterative phase retrieval approach was implemented to solve this problem. However, the requirement to generate the intermediate intensities limits scalability of this algorithm. For a finer sampling of diameters and relative shifts, which is necessary for a high resolution, one ends up with many realizations of intermediate intensities which quickly becomes computationally expensive. Additionally, this method is composed of projection operations minimizing a Euclidean error metric. This implicitly assumes a Gaussian error distribution which becomes increasingly incorrect at lower signal levels [127].

4.3.1 Maximum-Likelihood Phase Retrieval

Taking the above mentioned considerations into account, we implement a maximum likelihood estimation strategy using pattern search technique dubbed as Maximum Likelihood Phaser (MaxLP) to retrieve the full $F_o(\mathbf{q})$ of an unknown target object.

The E- and M-steps of the EMC iteration are the same as before, with the only difference that we only use the most likely set of parameters rather than the whole probability distribution. The C-step is changed from the phase-retrieval-like approach using intermediate intensities to a direct search for the most likely complex Fourier amplitudes of the target object given the diffraction data and the current estimate of the latent parameters. The optimization is performed using a pattern search procedure implemented for each model pixel independently. The approach was tested for different intensity signal levels in diffraction datasets with low signal having as few as 2000 photons per pattern. We find that the algorithm is more noise-tolerant with better fidelity at lower signal levels where the previously introduced *divide* and *concur* approach yields poor results.

In addition, the MaxLP approach scales more favorably as the sampling of latent parameters is made finer. The computational complexity of the C-step is now independent of the sampling, while in the previous approach, finer sampling would result in a large number of intermediate intensities from which to perform the "phase retrieval". Since the final resolution is ultimately determined by the accuracy of the estimated latent parameters, this algorithm can be efficiently scaled and the parameters to be refined by local searches.

4.3.2 Single-pixel Behavior

The optimal $F_o(\mathbf{q})$ is determined at every model pixel independently. To illustrate the working of the reconstruction algorithm, we now discuss the behavior for a single pixel detector at a given \mathbf{q} assuming the orientations are known. In holographic- or reference-enhanced-SPI, the measured intensity at a given detector pixel is described by Eqn 4.2. The estimated orientation of the object then relates the detector pixel to some pixel in the Fourier representation of the target object's electron density.

A single model pixel intensity at a fixed \mathbf{q} can be written as

$$I_{\text{pix}} = \left| F_{o,\text{pix}} + F_{s,\text{pix}}(D) e^{2\pi i \mathbf{q}_{\text{pix}} \cdot \mathbf{t}} \right|^2, \tag{4.3}$$

Here F_o is the complex number which we need to solve from the diffraction dataset, I_{pix} , with varying shifts, t and AuNP diameters, D, at the given model pixel from multiple realizations in different patterns.

Figure 4.2 depicts the behavior of the true intensity and measured photon counts for different phase shifts ($\Delta s = \mathbf{q.t}$) between the AuNP and the target object. The photon distribution at a given phase shift value is Poisson distributed with the

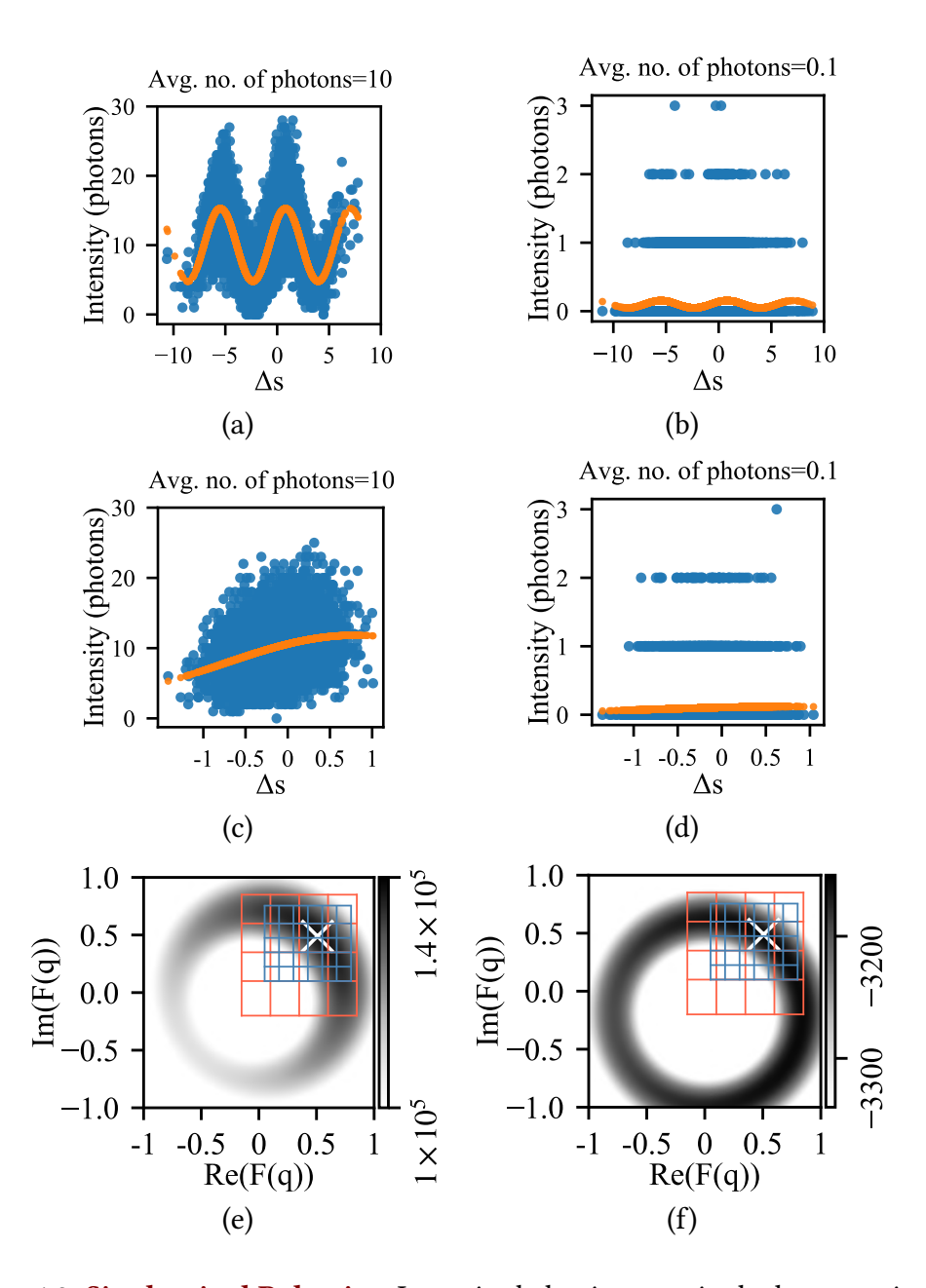


Figure 4.2: **Single-pixel Behavior.** Intensity behavior at a single detector pixel for a holographic-SPI diffraction data. (a)-(d) Average number of photons vs relative phase shifts of gold sphere with respect to the target object. The ideal intensity on the same pixel is represented by the orange line. (e) & (f) Log-likelihood landscapes obtained from diffraction data for case (a) & (d), respectively. The '×' denotes the true value of $F(\mathbf{q})$ maximizing the log-likelihood. The grid lines (1st - *orange* and 2nd - *blue*) depict the size of pattern search grid in consecutive iterations.

mean being the true intensity shown in orange. When the average photon count at the pixel is high enough, the intensity follows a sinusoidal form with respect to the phase shifts, as seen in Fig. 4.2(a). The relative phase, offset and amplitude of this sinusoidal curve tells us the phase and magnitude of the object's Fourier transform at that q. As the range of phase shifts becomes small, one is effectively zooming into the sinusoidal curve for the same amount of average photons (see Fig. 4.2(c)), and the fitting becomes more challenging.

Similarly, when the average photon count on the detector falls, as seen in Fig. 4.2(b), the photon distribution becomes too sparse to immediately see the true intensity and in the hardest case, for smaller phase shifts and low counts the true intensity plot becomes almost flat (Fig. 4.2(d)).

The log-likelihood of such a diffraction dataset at any model pixel can be calculated by

$$Q(F_{o,\text{pix}}) = \sum_{d} K_{\text{pix},d} log(I_{\text{pix},d}) - I_{\text{pix},d},$$
(4.4)

where $I_{\text{pix},d}$ is predicted intensity given by Eq. 4.3 and $K_{\text{pix},d}$ is the number of observed photons in pattern number d. The $K_{\text{pix},d}$! term is neglected since it does not depend upon the model F_o . Figure 4.2(e-f) show this log-likelihood function distribution in the complex plane of $F_{o,\text{pix}}$ for the diffraction pattern data given from Fig. 4.2(a) and (d), respectively. The likelihood has a well behaved landscape with a sharp maxima with different values of real and imaginary part of F_o , when the average photon count is high enough with large shift range. When the average photon count is low with small shifts, the likelihood landscape becomes much flatter along the visible ridge.

Furthermore, this likelihood distribution is independent of the measured photon counts at the neighboring detector pixel. As a result, one can implement an algorithm for the each pixel individually as a maximum-likelihood estimation problem and try to converge for an optimal F_o for each pixel and trivially parallelize the algorithm over all model pixels. Of course, the Fourier transform is oversampled and thus, the model at neighboring pixels are strongly correlated. This information will be taken into account later in Section 4.4.

4.3.3 Finding the most likely solution

The likelihood function given in Eq. 4.4, can not be solved analytically. While one can perform this 2D optimization in the complex plane with many methods, we found that derivative based approaches were not robust, with maximization of

likelihood failing for low photon count cases and small shifts. We found reasonable success with a pattern search approach [187] for two reasons: it could be efficiently parallelized on the graphical processing units (GPUs) and secondly it was quite robust in low signal and small shift cases.

Pattern search optimization is essentially a non-derivative technique that does not require a gradient calculation in its update of parameters. The search begins with a 2D grid of values of **F** (see Fig. 4.2(e-f), orange grid lines). At each iteration, this grid moves to a set of values which best maximizes the likelihood function. If it finds a set of values of **F** which does not have better likelihood then it stays at current value and the grid shrinks and becomes denser with smaller steps between the grid values (blue grid lines). A search is run till a threshold error between the current and the previous estimate is reached.

This is performed for all the model pixels and then the final model is used to get updated latent parameters for the next EMC iteration. The pseudocode for a single iteration is described in Algorithm 1.

4.4 Results

We tested the performance of the algorithm described above on 2D simulated data with a single angular degree of freedom. The target object was a randomly generated agglomeration of small spheres, approximating the electron density distribution of a biological sample. Each diffraction pattern was a Poisson-sampled distribution of scattered photons from a conjugate object consisting of the target attached to a spherical gold nanoparticle (AuNP) reference. The average diameter of the AuNP was roughly 1/5th the size of the target and the contrast was 11 times higher, to reflect the electron density ratio of gold to organic matter. The conjugate objects varied from pattern to pattern in multiple ways. The relative shifts in x- and ydirections between their centers were sampled from a normal distribution with a standard deviation of 1 pixel. The diameter of AuNP was also normally distributed with a mean and standard deviation of 7 and 0.5 pixels, respectively and the target object was 35 pixels across. The intensity distribution from this composite object was rotated in-plane by a uniform random angle before Poisson sampling. The diffraction patterns were collected on a circular detector with a diameter of 185 pixels and a central hole with a 4 pixel radius.

Multiple datasets were simulated with a varying signal levels with 10,000 patterns in each dataset. A common randomly generated object was used as the target in all of the simulations. The signal levels ranged from 2×10^3 to 10^5 photons/frame

Algorithm 1 Pseudocode for one iteration of the MaxLP. The latent parameters are determined as in the EMC algorithm.

```
Input:
F_o(q) \triangleright Current estimate of target object Fourier transform at pixel q
K_{\text{pix},d} \triangleright Dataset: photons at pixel, pix and frame, d
\Omega_d \triangleright Current estimate of latent parameters: \mathbf{t}, D, \theta for each frame d
grid ▷ Square grid of points in the complex plane with unit spacing
function RunIteration(F_o(q), K_{\text{pix},d}, \Omega_d)
     for q in 1..N_{\rm pix} do
           F'_o(q) \leftarrow \text{OptimizePixel}(q, F_o(q), K_{\text{pix}}, \Omega)
     end for
end function
function OptimizePixel(q, F_o, K, \Omega)
     step \leftarrow |F_o|/4
     for n in 1..10 do
          for i in 1..N_{grid} do
                F_i \leftarrow F_o + \operatorname{grid}_i \times \operatorname{step}
                Q_i \leftarrow \text{Likelihood}(K, \Omega) \triangleright (Eq. 4.4)
          end for
          i_{\text{opt}} \leftarrow \operatorname{argmin}_{i} Q_{i}
          \mathbf{if}\ i_{\mathrm{opt}} = 0\ \mathbf{then} \triangleright \mathit{Center\ of\ grid}
                step \leftarrow step / \sqrt{N_{grid}}
          end if
          if step < |F_o| \times 10^{-3} then
                break
          end if
     end for
end function
```

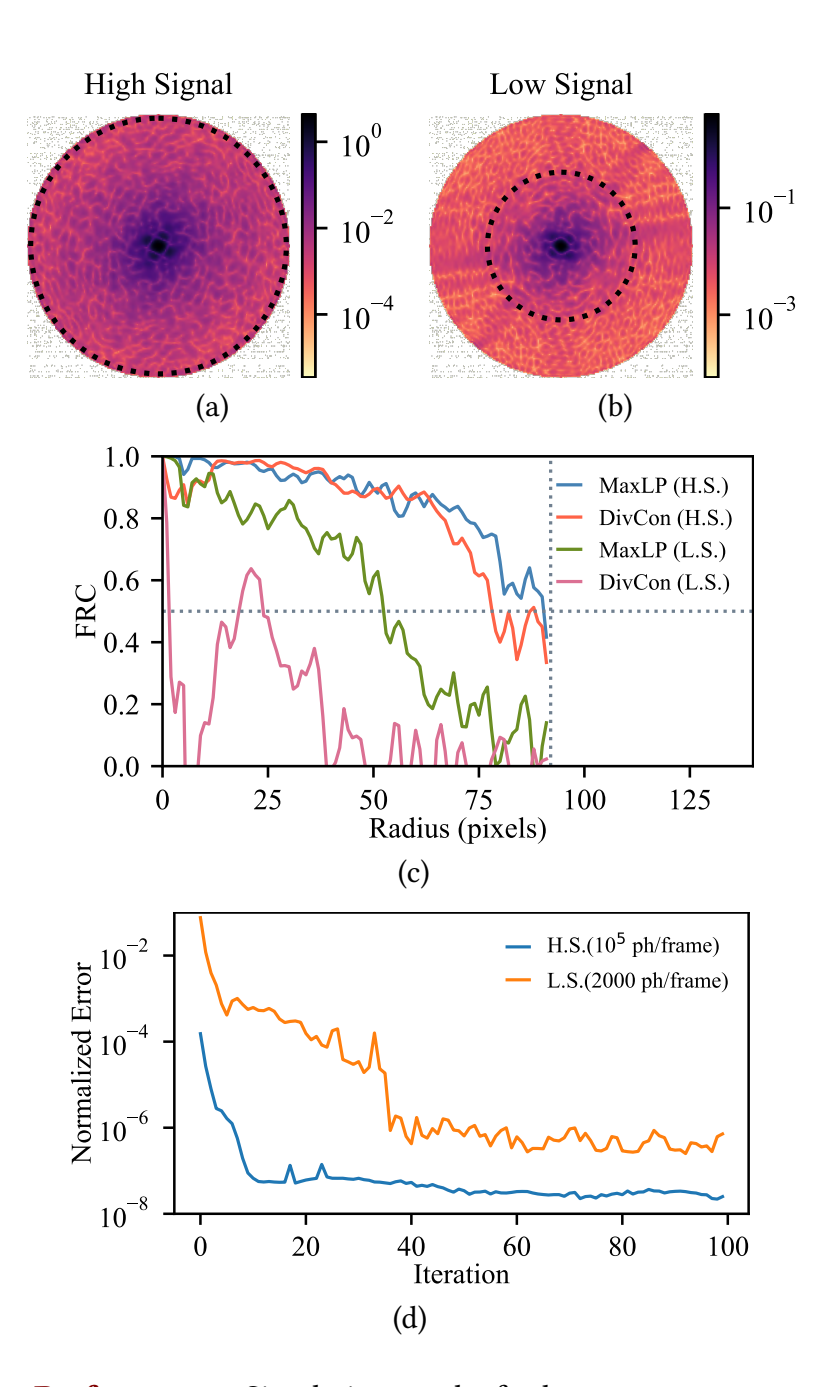


Figure 4.3: **Performance.** Simulation results for homogeneous target object attached to a spherical AuNP as reference. (a) Magnitude of reconstructed Fourier model for high signal diffraction data with MaxLP method (10^5 ph/frame). (b) Same for low signal diffraction data (2000 ph/frame). Both datasets had 10^4 frames. Dashed rings highlight the FRC=0.5 cutoff. (c) Comparison of Fourier ring correlation (FRC) between reconstructions and ground truth with different signal level diffraction data. Maximum-likelihood Phaser (MaxLP), Divide and Concur (DivCon), High Signal (H.S.) and Low Signal (L.S.). (d) Normalized error (difference between successive iterations) vs iteration number showing faster convergence for higher signal levels as observed in conventional SPI as well [4].

at the low and high extremes.

Figure 4.3(a) and (b) depicts the absolute magnitude of the reconstructed complex Fourier model for the highest and lowest signal levels. The algorithm was run for 100 iterations and Fig. 4.3(d) shows the convergence behavior. Convergence is achieved after 15 iterations for the high signal level and 40 iterations for the low signal level, respectively. For each reconstruction, the iteration times ranged from 200 s for the low signal case and 600 s for the high signal case on a single V100 GPU. At the final reconstruction iteration, both Fourier models have a few poorly reconstructed pixels, primarily at low q. This is due to the missing data in the central hole as well as regions where the scattering from the reference is significantly weaker than from the target. The intensity at these pixels is only minimally affected by the frame-to-frame variation in shifts or diameters, resulting in the Fourier phase being poorly constrained. These pixels were filled in using the following approach. First, a support mask was calculated using data from moderate q using the darkfield diffractive imaging approach [188]. This mask was then used as a real-space constraint and the difference map iterative phase retrieval algorithm [115] was used to fill in the missing region as well as obtain a real-space image.

4.4.1 Signal level dependence of reconstruction quality

The fidelity of the reconstructed model is calculated using the Fourier Ring Correlation (FRC) metric, shown in Figure 4.3(c). We compare the performance of MaxLP method with the previously published method of *divide* and *concur* in [35] at low and high signal levels. For high signals, both algorithms perform well, but the *divide* and *concur* approach fails for the low signal case, whereas the MaxLP reconstructs the Fourier model with FRC > 0.5 up to q = 55 pixels. This can be attributed to the MaxLP method correctly accounting for the Poisson noise process rather than the Gaussian noise model implicit in the *divide* and *concur* method.

We then investigate the ability of the algorithm to correctly estimate the latent parameters given the current model. The sampling rate of all the latent parameters is kept identical across all datasets to facilitate comparison. Figure 4.4 shows the error distribution for the diameter of AuNP , in-plane orientation and relative shifts in x- and y- directions, respectively. The sampling of the in-plane orientation is in range of 0 and 180° with step size of 2° . In Fig. 4.4(a) one can see distribution of errors between the retrieved and true in-plane angles for high and low signal level, respectively. The centers are shifted since the reconstruction has an arbitrary overall orientation. As expected, the distribution is narrow for high signal, with

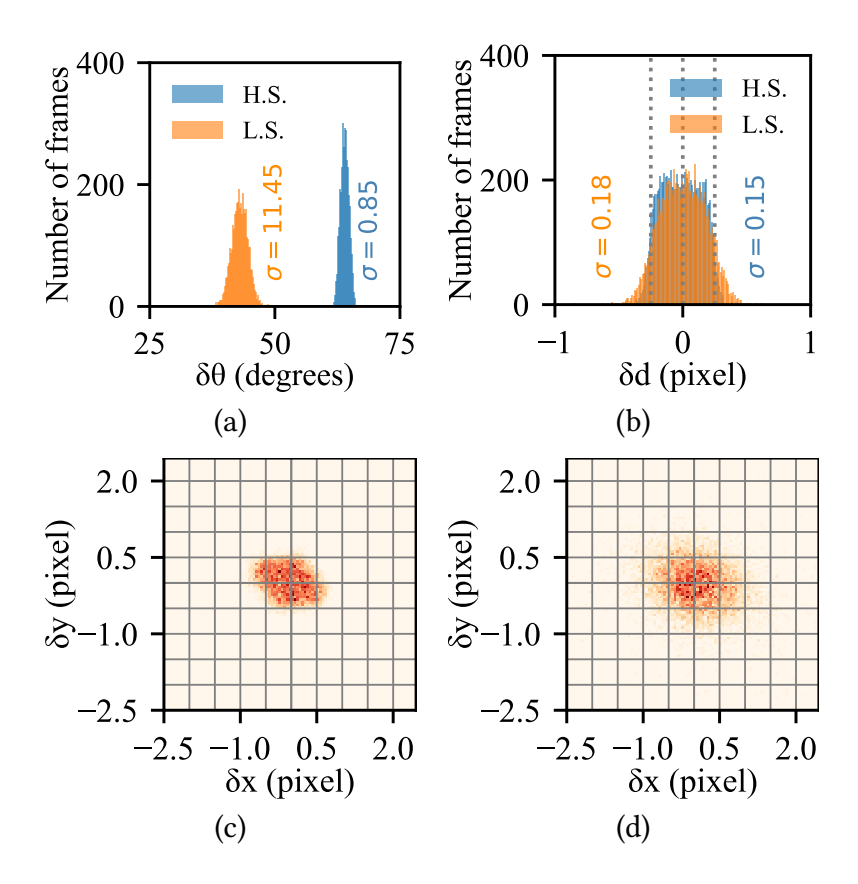


Figure 4.4: Latent Parameters. Error distribution for reconstructed latent parameters for homogeneous target object attached with a spherical AuNP as reference for low (L.S.) and high signal (H.S.) levels. (a) In-plane orientation, (b) diameter of gold sphere, (c) & (d) relative displacements between center of target object and reference in x- and y- direction. The vertical lines in (b) and the grid lines in (c) and (d) show half the sampling rate, which sets a lower bound on the width of the distributions.

 $\sigma=0.85^\circ$ which is below the sampling rate, and significantly broader for low signal with $\sigma=11.4^\circ.$

Similarly, AuNP diameter and x-&y- shifts are sampled with a step size of 0.5 and 1 pixel, respectively. Figure 4.4(b) shows that the diameter of the AuNP for each frame is close to the true values with uncertainties for high and low signal being 0.15 and 0.18 pixels. Even for the lowest signal level, the diameter can be accurately estimated below half the sampling rate, which is consistent with the high precisions which can be obtained in small-angle X-ray scattering. Figure 4.4(c) & (d) show the error distribution of shifts in x- and y- direction for the two signal levels. The error is confined for many of the patterns within half the sampling bin size of 1 pixel. However the error distribution for the low signal case is relatively broad. This is strongly correlated to the error in the inplane orientations. A large error in orientation leads to wrongly estimated shifts because the diffraction pattern is obtained by adding the AuNP to the target object and rotating the entire composite object. The predicted shift values are rotation-corrected using the predicted orientations and then compared with true values.

The behavior of the reconstruction metrics discussed above is evaluated for multiple intermediate signal levels in Fig. 4.5. Figures 4.5(b-d) show the dependence of the latent parameter errors on the signal level. Here we see that beyond 5000 photons/frame, the errors are all below the sampling rate indicated by the dotted red line. Figure 4.5(a) shows the dependence of the resolution on signal level, which depends both on accurate estimation of latent parameters as well as total signal from all the frames in aggregate. Thus, we expect the reconstruction FRC to improve significantly with more patterns beyond this threshold of 5000 photons/frame.

4.4.2 Heterogeneity of target object

Many biological entities have flexible sub-units that can move following a continuous landscape of various conformational states. The study of these conformation changes can help us understand the function of such biomolecules. However, there are significant computational challenges to retrieve conformational states and structure of target object from diffraction data. In conventional SPI, the averaging of patterns from variable structures has an undetermined effect on the retrieved structure. This is because even though the Fourier transform is a linear operator, it's the intensities (squared magnitudes) that are averaged across different frames. In general, the resultant intensity distribution has lower contrast and is not the Fourier transform of any compact object. In some cases with uncorrelated random motion

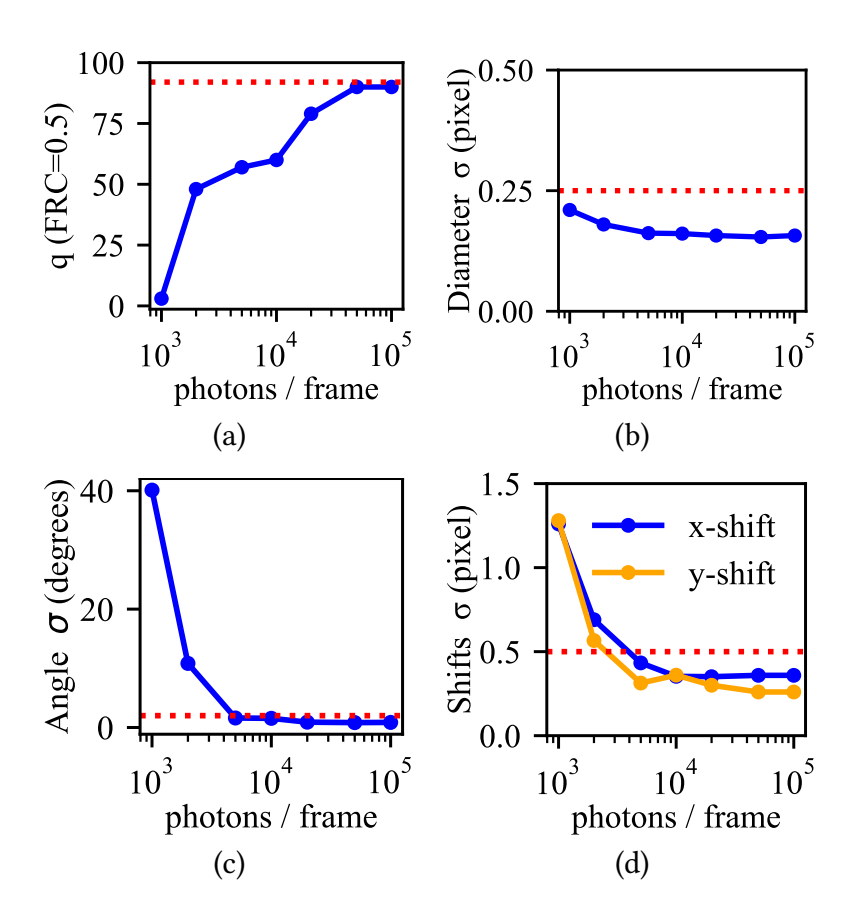


Figure 4.5: **Signal Level Dependence.** Evaluation metrics of Maximum-likelihood phaser (MaxLP) for different photon signal levels. (a) q value when FRC = 0.5 vs number of photons/frame. The horizontal dashed line corresponds to a resolution of 1 real-space pixel. Standard deviation values for (b) diameter errors, (c) orientation errors, and (d) shift errors in x- and y- direction. The horizontal dashed lines in (b)-(d) indicate half the sampling rate.

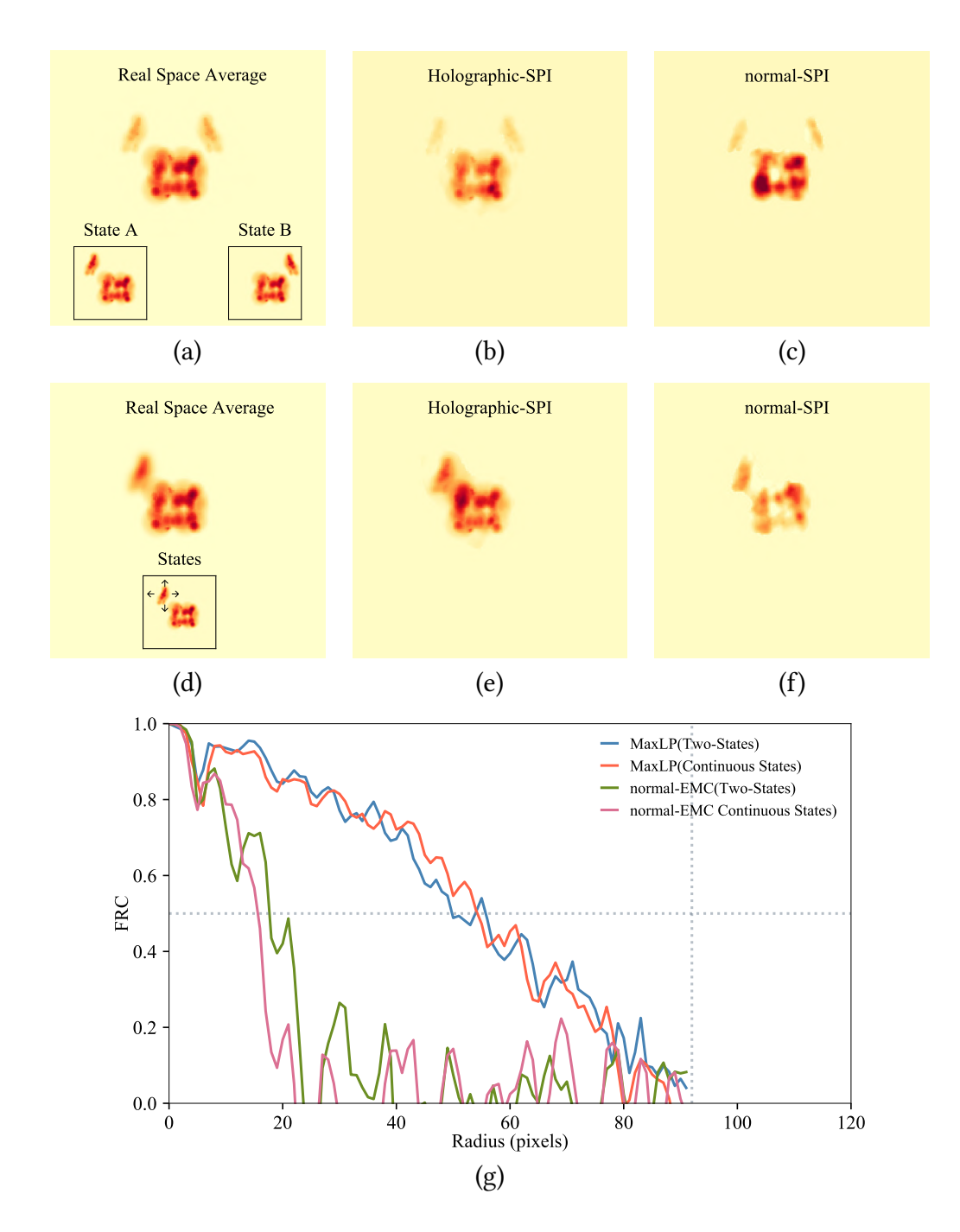


Figure 4.6: **Structural Heterogeneity.** Simulation results for structural heterogeneity in the target object (a) Average structure of target object which exists in one of two discrete states (State A & State B, shown in inset). (b) Reconstructed real-space target object with an AuNP sphere attached using MaxLP. (c) Reconstructed real-space target object without reference attached. (d) Average structure of target object which exists in a continuous distribution of states. Inset shows the target object with random sub-unit where arrow depicts the free direction of motion for sub-unit in each shot. (e) Reconstructed real-space target object with an AuNP sphere attached using MaxLP. (f) Reconstructed real-space target object without reference attached. (g) Comparison of Fourier ring correlation (FRC) between holographic-SPI and normal-SPI for the different scenarios.

of atoms, one could expect the background-subtracted intensities to represent the scattering from the average structure, but this is in no way guaranteed, especially with correlated motions. Thus, extensive computational efforts must be employed to discover a subset of data from a homogeneous ensemble or to solve for additional latent parameters associated with structural variations.

In the current holographic regime, we solve for the complex Fourier transform, which is linearly related to the real-space structure. Thus, we may expect the reconstruction to be that of the average structure. To examine whether this is indeed the case, we perform two computational experiments below where the target object varies from frame to frame but the algorithm still attempts to reconstruct a single structure.

Two-state heterogeneity

We investigate the scenario in which the target object is composed of a homogeneous rigid part (the large unit) and a moving sub-unit that exists in different states shot-to-shot. Without explicitly modifying the MaxLP algorithm or providing any information about such heterogeneity, the algorithm analyzes the diffraction dataset simulated from these target objects. In the first case, the moving sub-unit object exists in two distinct discrete states: State A & State B, as shown in inset of Fig. 4.6(a). The larger sub-unit remains in same position, whereas the smaller sub-unit occupies one of two opposite states about the center of the larger one.

The diffraction patterns are now generated from this heterogeneous ensemble in two ways, one with the AuNP attached and the other with just the target object (as in conventional SPI). In the former case, we still have the shot-to-shot variations in the AuNP diameter and relative position as before, which are recovered with the MaxLP procedure developed above. For the latter case, conventional intensity reconstruction is performed with the EMC algorithm, followed by phase retrieval.

Figure 4.6(b-c) shows the reconstructions from the holographic and normal SPI scenarios. In the holographic case, the reconstruction is an object very similar to the real-space average of structure shown in Fig. 4.6(a). However, in the absence of a reference, as shown in Fig. 4.6(c), the reconstruction after phase retrieval is quite poor. This is also seen in the FRC comparisons with the real-space average in Fig. 4.6(g).

We would like to stress that this result, while expected, is not trivial. First, we are still measuring real-valued intensities and not complex Fourier amplitudes. Secondly, each pattern has a different set of latent variables, leading to different

intensity distributions on the detector. The difference is that the MaxLP algorithm does not average these intensities directly, but rather fits a common complex Fourier transform of the target object to all these intensities, which turns out to reflect the average object over all patterns.

Continuous heterogeneity

The previous example addressed the extreme case of having the moving sub-unit in two diametrically opposite locations. We now investigate a more realistic scenario where the moving sub-unit occupies a continuous local distribution of positions. The displacements are sampled from a normal distribution with $\sigma=0.5$ pixels, as represented by arrows in the inset of Fig. 4.6(d). The dataset consists of diffraction patterns generated from the target object where the smaller sub-unit is in a different position every frame. Figure 4.6(e-f) show the MaxLP and normal SPI reconstructions as before. In the holographic case, the homogeneous part is reconstructed to a good resolution while the wobbling sub-unit part has been reconstructed as a blurry object, as expected in a real-space average. This is in contrast to the normal SPI case, where the resolution of the reconstruction is globally affected due to the averaging in intensity space, leading to loss of contrast at higher q. Once again, the Fig. 4.6(g) shows that the holographic SPI reconstruction compares much more favorably with the average structure.

The critical aspect of this robustness to heterogeneity seems to be the presence of translational latent parameters. For the continuous translation case, one can envision sharpening the small sub-unit reconstruction by choosing the AuNP shifts relative to that sub-unit rather than whole object. However the current method will struggle to solve for a conjugate of two unknown objects with a shot-by-shot variation in their relative position. This is because of the assumption that the signal at any given q is composed of a known reference and the target object, and if part of the object itself is used as the reference, its Fourier transform at high q is not known a priori before sharpening.

4.5 Conclusions

In conventional SPI experiments, the biggest challenge in reaching sub-nm resolutions is to collect a large number of diffraction patterns with sufficiently low background in order to enable orientation determination and averaging. The introduced holography-based imaging methodology overcomes this issue by attaching a

strong scattering object (a reference) to the sample of interest. this significantly improves background tolerance, but adds a large amount of computational complexity by introducing more unknown parameters associated with each pattern defining the conjugate system. In this work, we described an algorithm based on maximum-likelihood estimation using pattern search called MaxLP that enables one to scale the method to high resolution and to weakly scattering objects. The results above show how it significantly outperforms the previously published method in the cases of low signal and without the need for a large number of intermediate average intensity models.

We extended the application of MaxLP to retrieve the structure of the target object for the scenario where it has shot-to-shot structural heterogeneity. Two cases of heterogeneity were investigated: one in which a sub-unit is in two discrete conformational states and one in which the sub-unit is in a continuous distribution of states. In both the cases, the algorithm reconstructs an object that is real space average of structure in all the conformation states, without prior knowledge that the target object was varying from shot-to-shot.

On the contrary, the conventional SPI without an added holographic reference generates an average over the intensities in Fourier space that on phase retrieval yields a poorly reconstructed object not just in the vicinity of the moving sub-unit, but globally due to the delocalized nature of the Fourier transform.

The algorithm can also be applied when the reference is a 2D crystal lattice and the target object is located in one of the unit cells. In such scenarios, one solves for relative shifts between the center of unit cell and target object in each shot and the size of unit cell. In future work, we will explore the possibility of adjusting the xy shifts in order to selectively reconstruct different regions of the particle to varying degrees of sharpness. We also plan to explicitly incorporate structural heterogeneity either as multiple discrete classes [10] or as continuous latent variables [136]. While intensity-space classifications have been performed previously, the holographic approach may enable a more fine-grained approach similar to that applied in cryogenic electron microscopy [171].

Acknowledgments: The authors acknowledge valuable discussions with Tamme Wollweber, Yulong Zhuang, Zhou Shen and Parichita Mazumder. This work is supported by the Cluster of Excellence 'CUI: Advanced Imaging of Matter' of the Deutsche Forschungsgemeinschaft (DFG) - EXC 2056 - project ID 390715994.

5

Lattice-enhanced Holographic-SPI

 \prec The majority of the content in this chapter is adapted from the manuscript titled: *High-background X-ray single particle imaging enabled by holographic enhancement with 2D crystals* (In Preparation), co-authored by Zhou Shen and Kartik Ayyer. \succ

Authors Contributions:

K.A. conceived the project. The data generation and reconstruction code was developed by A.M.. K.A., S.Z. and A.M. analyzed the results and wrote the manuscript.

5.1 Abstract

Biological nano-machines, such as viruses and protein assemblies, derive their function from well-ordered 3D structures. X-ray single particle imaging offers the potential to visualize structures of such nanoscale objects *in situ* at near-atomic resolution. However, high background and radiation damage from long exposures make even detection of these objects impossible at synchrotrons. Here, we introduce a novel experimental technique based on the holographic principle, exploiting a strongly scattering 2D crystal lattice placed near the object. The holographic enhancement from the lattice Bragg peaks allows structure retrieval even in background levels up to 10⁵ times higher than the object signal. This method improves the signal-to-background ratio, supports practical fixed-target sample delivery, and enables high-resolution imaging under near-native conditions. A reconstruction algorithm recovers the structure of the target object along with unknown

experimental parameters, such as orientation, position within the unit cell, and incident fluence. Numerical simulations with *Ribosome* as model shows robustness in varying background levels and exposure time conditions. The approach opens new avenues for high-resolution imaging of biological objects in high-background environments.

5.2 Introduction

Biomolecules, such as viruses and large protein complexes, play an essential role in understanding fundamental life processes, including their functionality and survival mechanisms [189, 190]. The structures of these biological complexes largely determine their functional properties, making the imaging of their architecture and dynamics an essential aspect in structural biology [191].

X-ray single particle imaging (SPI) is a powerful technique for visualizing the structure and ultrafast dynamics of nanoscale entities, such as viruses and inorganic nanoparticles, in near-native environments [8, 10, 132, 135]. Conformational heterogeneity in such systems requires the ability to observe individual particles rather than ensemble averages. Traditional methods like crystallography and cryo-electron microscopy rely on crystallization or shock-freezing—conditions far removed from physiological environments—and thus face inherent limitations [113]. SPI overcomes these challenges by capturing diffraction snapshots from many identical particles before radiation damage sets in [192, 193], enabling 3D structural reconstruction with nanometer-scale resolution [4, 7, 10]. It can also disentangle conformational heterogeneity and track ultrafast dynamics [132, 134–136, 194].

SPI has shown its greatest successes at X-ray free-electron laser sources (XFELs), which provide ultrabright, ultrafast pulses ideally suited for imaging weakly scattering biological particles [10, 76, 169, 177]. However, XFEL access is limited, and optimizing sample delivery to minimize experimental and instrumental background remains a major challenge [167, 176, 195, 196]. Synchrotrons—being more widely available and increasingly brilliant [197–199]—offer an attractive alternative for routine SPI. However, their lower flux per pulse and longer exposure times result in elevated background scattering from substrates, beamline components, and other non-target sources, often overwhelming the already weak signals from biological samples [133, 200]. This slowly varying background makes biomolecular imaging extremely difficult, limiting the applicability of SPI at synchrotrons.

While aerosol-based sample delivery minimizes background at XFELs, adapting it for synchrotron use remains challenging. Fixed-target approaches, though more

practical at synchrotrons, introduce additional substrate scattering that degrades data quality [182–184]. Moreover, current X-ray imaging at synchrotrons is largely limited to larger particles that scatter strongly enough to produce detectable patterns [33, 201]. These challenges—compounded by radiation damage—continue to hinder the dream of SPI of various biomolecules at synchrotrons, underscoring the need for novel experimental configuration and detection strategies to fully unlock their potential.

Here, we propose an experimental strategy to enable high-resolution SPI at synchrotrons by employing a strongly scattering 2D crystal lattice as a holographic reference in a fixed-target setup. This approach adapts "reference-enhanced" holographic SPI, initially developed for XFELs, in which a reference object—such as a gold nanoparticle—was used [35, 36]. In introduced method here, a 2D crystal lattice is fabricated on one side of a thin substrate, producing sharp Bragg peaks, while target object particles, such as ribosomes, are randomly dispersed on the opposite side [202, 203]. The far-field diffraction arises from strong interference between the lattice signal and the weak scattering from the object. The holographic interference significantly enhance the signal-to-background ratio (SBR), even when background noise exceeds the object signal by orders of magnitude up to 10^5 . By integrating Bragg peak intensities, the weak signal of target object can be reliably extracted which exists as modulation on the Bragg peaks. A tailored reconstruction algorithm simultaneously determines the structure of object, in-plane orientation, translation shift within the unit cell, and incident beam fluence, eliminating the need for additional support constraints and minimizing modeling assumptions [36].

Simulations using the ribosome as a model biomolecular complex demonstrate that this lattice-based holographic approach can resolve target structures under conditions of high background scattering, substrate contamination, and variable beam exposure. The method's robustness accommodates the longer exposure times typical of synchrotrons, mitigating challenges such as radiation damage and impractical sample delivery [35]. By leveraging the lattice's coherence and single-shot diffraction patterns, the technique simplifies phase retrieval and enhances signal strength, making it well-suited to synchrotron conditions. This framework broadens the scope of SPI, enabling routine, high-resolution imaging of diverse biomolecular assemblies at synchrotron facilities and establishing a path toward efficient, standardized structural studies.

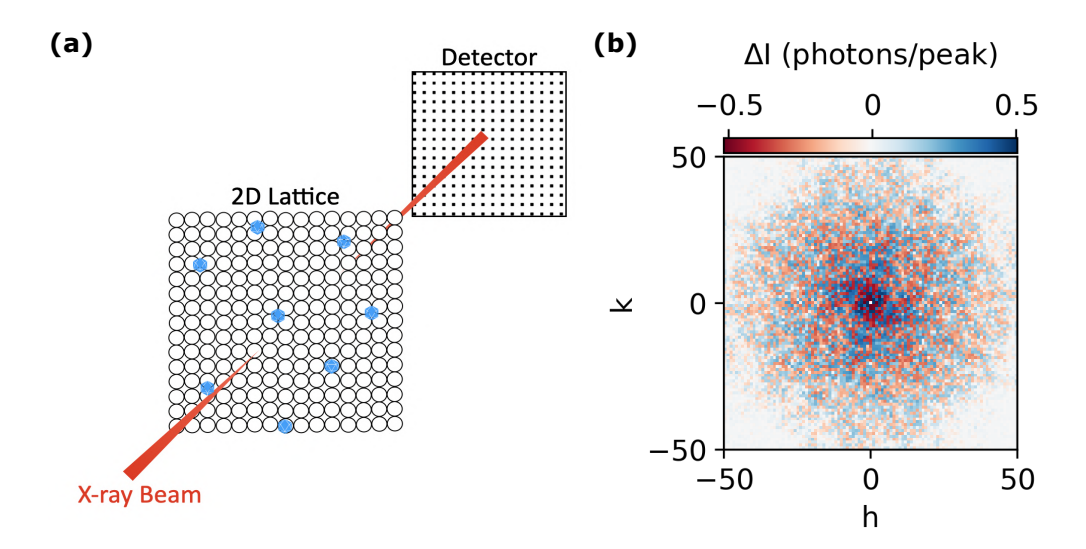


Figure 5.1: **Holographic SPI.** (a) Schematic of the holographic SPI setup. A 2D crystal lattice serves as the *reference*, while Ribosome particles (blue) are the target objects. The lattice is positioned on one side of the substrate, with target particles randomly distributed on the opposite side. The measured far-field diffraction pattern on the detector results from the coherent sum of Bragg peaks from several illuminated unit cells of the lattice and the scattering signal from a single target particle. (b) Far-field intensity modulation shown on a logarithmic scale. These modulations reflect Bragg peaks perturbed by the target object signal within the illumination area. The modulation, ΔI , is defined as the difference between the intensity from the lattice alone, $I = |F_{\rm L}(\mathbf{q})|^2$ and the intensity with both the lattice and the target object $I = |F_{\rm L}(\mathbf{q}) + \varphi \cdot F_o(R^{\top}\mathbf{q})e^{i2\pi\mathbf{q}\cdot\mathbf{s}}|^2$, for a given translation shift within unit cell, in-plane orientation, and incident fluence.

5.3 Problem Formulation

This section describes the mathematical framework used to simulate holographic single particle imaging in a fixed-target configuration using a 2D crystal lattice. The formulation is designed to replicate realistic synchrotron conditions. In this fixed-target setup, the lattice – either patterned onto a chip or self-assembled as a colloidal crystal [203] – on one side of a thin substrate while target object particles such as the Ribosome ([204]; PDB 7NHM, \approx 20 nm in diameter) are randomly dispersed on the opposite side, as shown in the schematic in Fig.5.1(a). This configuration generates structured interference patterns with Bragg Peaks on the detector, that encode information from both the lattice and the target object.

To model this setup, we conduct 2D numerical simulations using synthetic data considering experimental conditions. The electron density of a square lattice, denoted as $\rho_L(\mathbf{r})$, generates sharp Bragg peaks whereas $\rho_o(\mathbf{r})$, represents the pro-

jected electron density of the *Ribosome* as the target object. The total scattering contrast, incorporating a rotated and translated target object within a unit cell of the lattice is then expressed as :

$$\rho(\mathbf{r}) = \rho_L(\mathbf{r}) + \rho_o(R\mathbf{r} - \mathbf{s}),\tag{5.1}$$

where R corresponds to rotation operator for the in-plane orientation (θ) uniformly sampled from $[0,2\pi]$. The vector s denotes the translation shifts of the target object within the unit cell along x- and y- direction, uniformly sampled from [0,1] expressed in fractional coordinate. More broadly, s describes the lateral position of the target object relative to the lattice. For a periodic reference, such as a 2D crystal, s can be interpreted as a shift within the unit cell, reflecting the lattice's translational symmetry.

The corresponding diffracted intensity measured at the detector incorporating a slowly varying background $B(\mathbf{q})$, is given by :

$$I(\mathbf{q}) = \left| F_L(\mathbf{q}) + \varphi F_o(R^{\mathsf{T}} \mathbf{q}) e^{i2\pi \mathbf{q} \cdot \mathbf{s}} \right|^2 + B^2(\mathbf{q}), \tag{5.2}$$

where $F_L = \zeta \cdot \mathcal{F}[\rho_L]$ is the scaled Fourier transform of the lattice, $F_o = \mathcal{F}[\rho_o]$ is the Fourier transform of the target object, and φ is the incident fluence. The strong scattering from the lattice serves as a holographic reference, facilitating signal extraction of target object and translation shifts estimation. It's relative scattering strength compared to the target is controlled by ζ factor (discussed in Section 5.3.1) and plays a critical role in signal retrieval, noise tolerance, and the optimization of reference design.

The phase term, $e^{i2\pi\mathbf{q}\cdot\mathbf{s}}$, encodes the translational shift of the target object within the unit cell, while the background term, $B(\mathbf{q})$, accounts for contributions from the substrate, noise, and beamline scattering — common in synchrotron experiments. Consequently, the observed intensity, incorporating photon counting noise is:

$$I_{\text{obs}}(\mathbf{q}) = \frac{\text{Poisson}(I(\mathbf{q}) \cdot t)}{t} - B^2(\mathbf{q}), \tag{5.3}$$

where $\operatorname{Poisson}(\lambda)$ denotes a Poisson noise distribution with mean λ and t is the exposure time in seconds. In practical experiments, the background $B(\mathbf{q})$ can be estimated from dark measurements — taken without the reference or target particles — or by fitting smooth functions to detector regions away from the Bragg peaks. Accurate background estimation is essential and is assumed to be achievable using standard techniques such as polynomial fitting or blank frame subtraction. The 2D

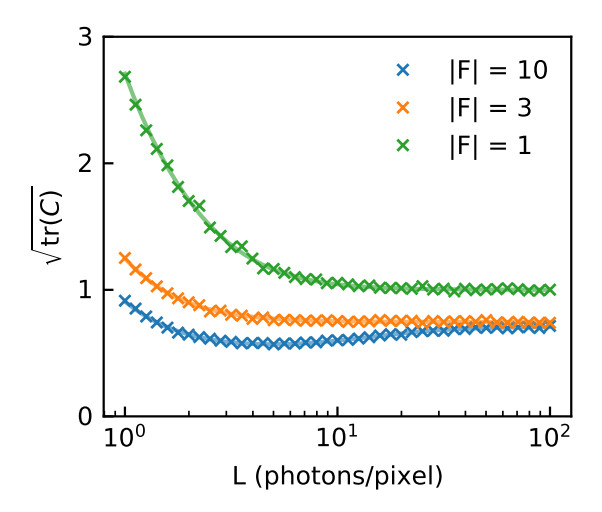


Figure 5.2: Scattering Strength of Lattice. The plot illustrates the uncertainty in estimating the scattering amplitude of $F_o(\mathbf{q})$, quantified by $\sqrt{\text{tr}(C)}$ (the square root of the combined amplitude and phase variances of $F_o(\mathbf{q})$) as a function of the scattering strength of the 2D crystal lattice, with a fixed background $B^2(\mathbf{q})$. Results are shown for three different scattering amplitudes of $F_o(\mathbf{q})$. Solid lines depict analytical estimates based on the inverse curvature of the objective function, while dots represent uncertainties obtained from simulated data through curve fitting.

lattice reference can be experimentally characterized using approaches similar to probe characterization methods commonly employed in ptychography [205].

Eq. 5.2 contains a cross term that plays a key role in determining the SBR. As shown in [35], this term includes a cosine component whose amplitude carries important information about translational shifts. A strong reference improves the robustness of the signal: although it increases the overall noise level, it also makes the signal less sensitive to background. The amplitude of the cross term's fluctuations is crucial—if it's large enough, the relative positions of the target can be extracted from the diffraction patterns. This amplitude also affects the feasibility to reconstruct the complex function $F_o(\mathbf{q})$.

5.3.1 Scattering Strength of Lattice

To quantify the influence of lattice strength on the accuracy of retrieving $F_o(\mathbf{q})$, we performed simulations to analyze how the uncertainty in fitting $F_o(\mathbf{q})$ depends on the strength of the lattice, $F_L(\mathbf{q})$.

In simple terms, one can rewrite Eq. 5.2 as:

$$I = \left| L + Fe^{i\phi} \right|^2 + B^2,\tag{5.4}$$

To characterize the relationship between lattice strength and estimation accuracy, synthetic datasets were generated for different values of F with a fixed value of B, specifically B=3, and F=1,3,10. In each scenario, 10^4 diffracted intensity measurements were produced. Subsequently, F was retrieved through non-linear fitting, and the resulting uncertainties were quantified by computing the covariance matrix, C.

The resulting uncertainty, defined as the square root of the trace of the covariance matrix $\sqrt{\text{tr}(C)}$, was evaluated across a range of lattice strengths L from 1 to 100. Fig. 5.2 reveals distinct regimes depending on the ratio between B and F.

For low scattering amplitudes $|F|^2 \lesssim B$, the uncertainty decreases monotonically with increasing lattice strength. Thus, stronger scattering lattices improve the accuracy of recovering F. For higher scattering amplitudes $|F|^2 \gg B$, an optimal lattice strength emerges around $L \approx B$, beyond which further increases in L reduce accuracy. This suggests that, for large scattering amplitudes of F, matching the lattice strength to the background intensity is advantageous.

Practically, ζ should be experimentally optimized to ensure lattice scattering strength matches or exceeds background noise intensity, maximizing reconstruction fidelity. For our simulation we keep the scattering strength of lattice as large as possible by allocating ζ to be high. This is also suggested [130], where uniformly redundant arrays (URAs) serve as structured references with high and spatially uniform scattering strength. These arrays provide a near-constant scattering strength up to high frequencies, significantly enhancing retrieval.

Given a flux of $1\times 10^{11}\,\mathrm{photons}/\mathrm{\mu m^2/s}$, the simulation with $\mathit{Dragonfly}$ [7] reports $3.56\times 10^5\,\mathrm{photons/sr}$ at a scattering angle corresponding to a resolution of $100\,\mathrm{nm}$ after 1 second of exposure. A 1 $\mu\mathrm{m}$ beam at 8 keV photon energy subtends a solid angle of $2.4\times 10^{-8}\,\mathrm{sr}$ at the position of a Bragg peak. Accordingly, the expected number of photons within such a Bragg peak is 8.54×10^{-3} .

5.3.2 Reconstruction Algorithm

We begin by defining the model intensity, which the reconstruction algorithm fits to the measured diffraction data:

$$I_{\text{calc}}(\mathbf{q}) = \left| F_L(\mathbf{q}) + \varphi F_o(R^{\top} \mathbf{q}) e^{i2\pi \mathbf{q} \cdot \mathbf{s}} \right|^2$$
 (5.5)

The goal of our reconstruction is to estimate four unknown parameters from noisy diffraction measurements: (a) the translational shift of the object, denoted by the 2D vector s, representing the position of the target object within the unit cell along the

x- and y-directions; (b) the incident fluence, φ , which quantifies the total number of photons illuminating the particle and effectively captures the degree of overlap between the particle and the beam; (c) the in-plane orientation of the object, θ ; and the phasing step for (d) the complex-valued Fourier transform of the target object, $F_o(\mathbf{q})$, which upon inverse Fourier transform, yields the real-space electron density, corresponding to a 2D projection of the Ribosome. Each diffraction frame is modeled as a noisy intensity measurement, as described in Eq. 5.3, and is associated with a randomly sampled orientation θ , translation s, and fluence φ . The exposure time, denoted t (in seconds), determines the total photon flux and thereby influences the signal-to-background ratio. Diffraction intensities are recorded on an $N \times N$ detector grid in reciprocal space. The corresponding real-space grid has dimensions 101×101 pixels, with each pixel representing 10Å with a total unit cell size of 100 nm.

To reconstruct \mathbf{s} , φ , and $F_o(\mathbf{q})$, the algorithm minimizes the discrepancy between predicted and measured diffraction intensities. Specifically, at each iteration, we minimize:

$$\mathcal{E} = \sum_{j} \sum_{\mathbf{q}} \left[I_{\text{obs},j}(\mathbf{q}) - I_{\text{calc}}(\mathbf{q}|\mathbf{s}_{j}, \varphi_{j}, \theta_{j}, F_{o}(\mathbf{q})) \right]^{2}$$
(5.6)

where $I_{\rm obs}({\bf q})$ represents the observed intensity, and $I_{\rm calc}({\bf q})$ is the predicted intensity across j frames and ${\bf q}$. This is carried out in an iterative cycle of three key updates through a systematic grid search over the unknown parameters, inspired by the pattern search method in [36]. The search proceeds in two stages: an initial coarse exploration over a broad parameter space, followed by a fine search around the best coarse estimate to refine the solution. While one can perform this 2D optimization in the complex plane with many methods, we found that with a grid search approach, it could be efficiently parallelized on the graphical processing units (GPUs) and secondly it was quite robust in high background limit.

Firstly, the algorithm begins by initializing $F_o(\mathbf{q})$, either with random values or using a circular object estimate sized similarly to the target object, where size estimates may be derived from SAXS studies [206]. For the simulations presented here, $F_o(\mathbf{q})$ is initialized randomly and in-plane orientation θ . To estimate the in-plane translation shifts \mathbf{s} and incident fluence φ , a coarse grid search samples possible values across a broad range and identifies the best candidate by comparing the measured and predicted intensities. A finer "zoomed-in" search then refines this estimate. In practice, each frame has its own shift and fluence, so these computations are repeated frame by frame.

Secondly, given the updated \mathbf{s} and φ , we next solve for the in-plane rotation angle θ . A coarse angular sweep from 0 to 2π locates a region of minimal error, followed by progressively narrower bracket searches around this best angle. We gradually reduce the step size until no significant further improvement is found.

Lastly, with \mathbf{s} , φ and θ fixed, we update each pixel q of $F_o(\mathbf{q})$. The unknown amplitude is treated as a complex number, and we perform a coarse-to-fine grid search on the complex plane to minimize the squared error across all frames. This entire three-step process constitutes one iteration. The algorithm then repeats these parameter updates for multiple iterations (e.g., 100) until convergence or a preset limit is reached.

This coarse-to-fine search approach, although computationally intensive for large experimental datasets, is feasible by leveraging parallelized computation. Future experimental implementations would benefit significantly from GPU acceleration and adaptive optimization algorithms to ensure efficient processing of extensive datasets.

The pseudocode for a single iteration is described in Appendix Section 2.

5.4 Results

We assess the performance of the reconstruction algorithm within the holographic SPI framework using a 2D crystal lattice. This evaluation focuses on both the quality of the reconstructed image and the error distribution in the estimated unknown parameters. Figure 5.3 presents a comprehensive analysis, including signal strength comparisons, reconstruction accuracy, and the precision of parameter estimation.

Figs. 5.3a-b display the ground truth 2D projection of the ribosome electron density and the unit cell of the 2D crystal lattice, modeled as random noise. Figure 5.3c shows the scattering strength as a function of ${\bf q}$ for the 2D lattice ($L=F_L({\bf q})$), the target object ($F=F_o({\bf q})$), and the background ($B({\bf q})$). Notably, the background intensity exceeds that of the target object by many orders of magnitude up to 10^5 , posing a major challenge for conventional SPI techniques, where weak biological signals are often obscured by overwhelming background noise—making structural reconstruction nearly impossible. In contrast, within the conjugated system used here, the lattice signal remains comparable to or even stronger than the background at low ${\bf q}$ values, ensuring the visibility of Bragg peaks. These peaks are modulated by the presence of the target object, allowing detection even in high-noise conditions. This approach relies on two key assumptions: firstly, the modulations introduced by the target object exceed the intrinsic fluctuations of the lattice signal,

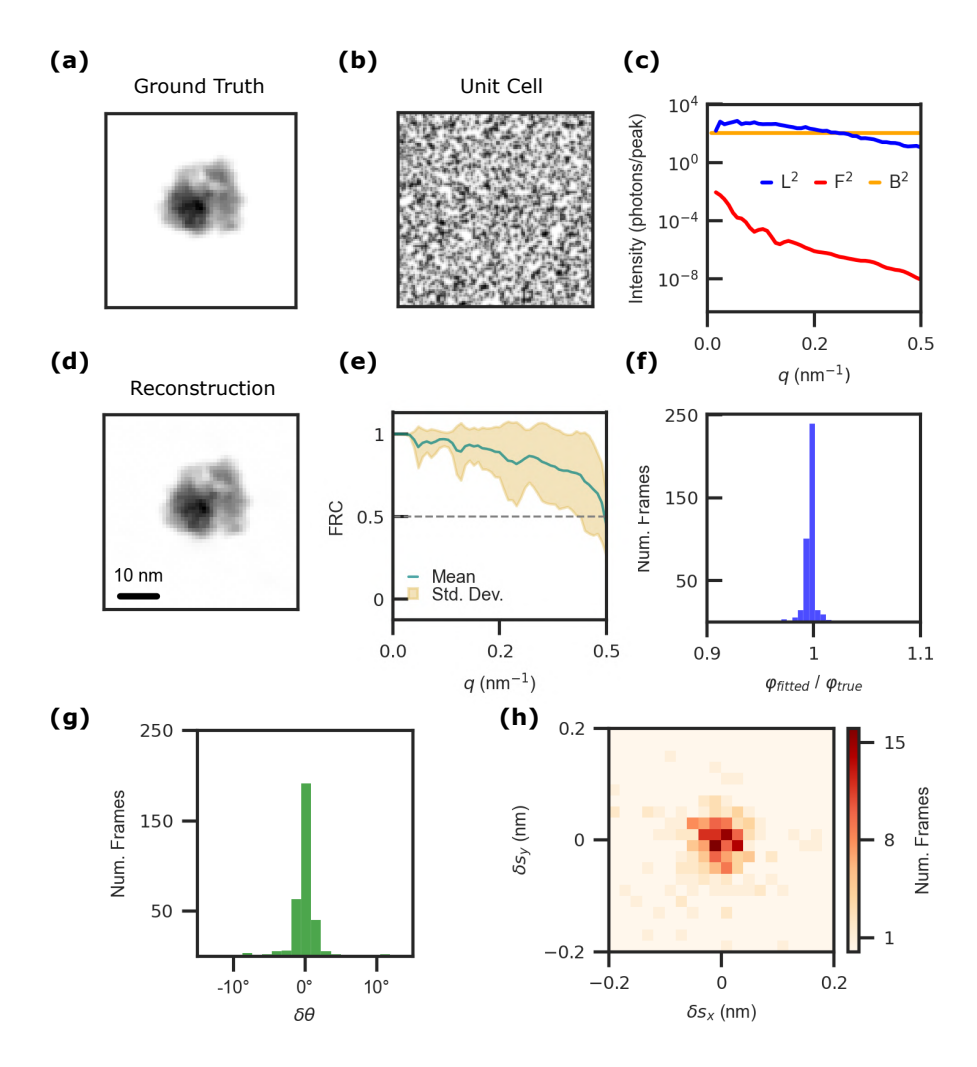


Figure 5.3: **Performance.** (a) Ground truth 2D projection of the Ribosome electron density. (b) Unit cell of the 2D crystal lattice, modeled as random noise. (c) Scattering intensity as a function of q for the 2D lattice (blue), Ribosome target object (red), and background (yellow). The background exceeds the signal of Ribosome by more than 10^5 , while the lattice intensity is comparable to or greater than the background. (d) Reconstructed electron density of the Ribosome (scale bar: 10 nm). (e) Fourier ring correlation (FRC) between the reconstruction and the ground truth $F_o(q)$. Green lines indicate FRC values averaged over 8 random-start reconstructions; the shaded region represents the standard deviation across runs. (f) Ratio of estimated to true incident fluence, φ . (g) Distribution of estimation errors for in-plane orientation angle θ across random runs. (h) Distribution of translational shift errors in the x and y directions for the target object within the unit cell (unit cell size: 100 nm). The performance is evaluated for exposure time t=1.

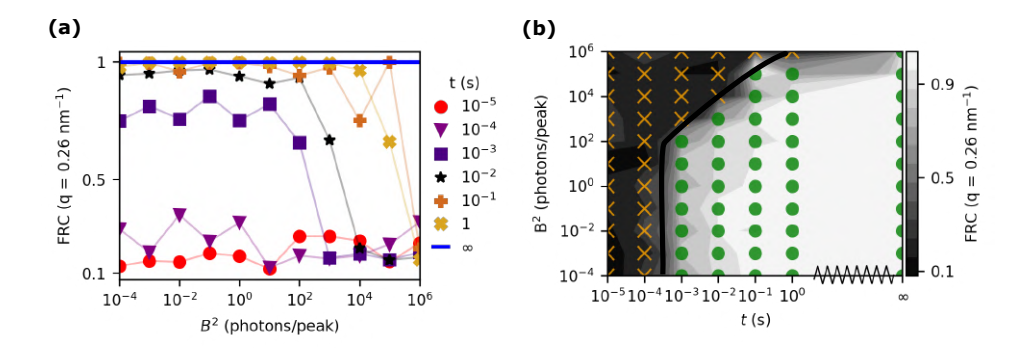


Figure 5.4: **Evaluation of Reconstructions.** (a) Fourier ring correlation (FRC) values at $q=0.26~\mathrm{nm^{-1}}$ vs background B^2 , for various exposure times (t). Each data point represents the maximum FRC value from eight random-start reconstruction runs. The horizontal solid line at FRC = 1 denotes the theoretical limit corresponding to infinite exposure time, $t\to\infty$. (b) Contour plot of FRC values (color scale) as a function of B^2 and t, both on logarithmic scales. Green circles indicate regions where FRC ≥ 0.5 , orange crosses mark regions with 0 < FRC < 0.5, and the black line traces the threshold boundary at FRC = 0.5. The sawtooth pattern along the bottom edge represents the approach to infinite exposure time $t\to\infty$ where FRC reaches 1.

and both the lattice signal and background can be accurately measured.

Fig. 5.3d presents the reconstructed electron density map of the ribosome, demonstrating that the algorithm can successfully recover fine structural details despite the weak and noisy diffraction signal shown in Fig. 5.3c. The reconstruction accurately captures the major features of the target object. Importantly, the coherent interference between the lattice and the target introduces sufficient modulation to enable effective phase retrieval — even in the absence of support constraints or any prior information about the target object.

Fig. 5.3e evaluates the quality of the reconstruction using the Fourier ring correlation (FRC) between the reconstruction and the ground truth, based on eight independent runs with randomized initializations and diffraction datasets. The solid curve shows the mean FRC across runs, while the error bars represent the standard deviation at each q. The FRC consistently exceeds the 0.5 threshold (the half-resolution criterion) across the entire q range, indicating reliable and reproducible reconstructions. The narrow spread of the error bars further highlights the algorithm's robustness to noise and initialization variability. These results correspond to a diffraction dataset with an exposure time of t=1 second.

Panels f-h of Figure 5.3 assess the accuracy of the reconstructed latent parameters: incident fluence (φ) , in-plane orientation (θ) , and translational shifts (t). Results are aggregated across all diffraction frames from eight independent

reconstruction runs, each initialized randomly. Figure 5.3f shows a histogram of the ratio between the estimated and true incident fluence, with a distribution tightly centered around 1—indicating reliable frame-to-frame estimation of beam exposure. Figure 5.3g displays the error distribution in the estimated in-plane orientation. Despite high noise levels, the errors are sharply peaked around 0° , demonstrating consistent and accurate recovery of particle orientation, which is crucial for proper alignment of diffraction frames. Figure 5.3h presents a 2D histogram of translational shift errors within the unit cell. The majority of estimates fall within ± 0.2 nm of the true position in both x and y directions, with regions of highest density indicated by dashed lines. Together, these results highlight the robustness and effectiveness of the method under realistic noise conditions, showing strong resilience to background interference, accurate estimation of experimental parameters, and consistent structural recovery across multiple runs.

The precision in estimating these parameters (θ, s, θ) directly influences the accuracy of particle alignment and subsequent averaging necessary for 2D reconstruction. Thus, the high accuracy demonstrated here ensures minimal error propagation into final reconstructed structures.

To assess the conditions under which our reconstruction algorithm remains effective, we systematically evaluated its performance across a range of background levels, B^2 and exposure time, t. Fig. 5.4a shows the FRC value at $q=0.26~\rm nm^{-1}$ as a function of these parameters. At low exposure times, the weak scattering from both the lattice and the target object fails to generate reliable interference patterns, resulting in reconstruction failure. Fig. 5.4b presents a contour plot of the FRC values at $q=0.26~\rm nm^{-1}$, mapped over logarithmic axes of B^2 and t. The plot reveals a distinct transition boundary (black line) where the FRC drops below 0.5, marking the threshold for reliable reconstruction. The color gradient indicates reconstruction quality, with yellow and red markers denoting specific evaluation points. These results collectively define a practical operating window for successful holographic SPI under varying experimental conditions.

5.5 Discussion

We introduced a holographic SPI technique for synchrotron radiation sources by employing a 2D crystal lattice. The approach addresses significant limitations in imaging biomolecules due to high background and prolonged radiation exposure. Through holographic enhancement from a strongly scattering lattice, the method substantially improves the SBR, making the signal from the target object recoverable

even in scenarios where background scattering exceeds the object signal by several orders of magnitude ($\approx 10^5$).

Numerical simulations, using the ribosome as the target object, validate the robustness and accuracy of the introduced methodology. The lattice reference effectively generates coherent interference with the weak target object signal, allowing the extraction of high-quality diffraction data under conditions that previously rendered SPI impractical at synchrotrons. Moreover, the optimization algorithm reliably reconstructs the electron density of the target object, simultaneously retrieving unknown experimental parameters such as orientation, translation shifts within the unit cell, and incident fluence. Results from multiple independent runs underscore the consistency and reproducibility of the reconstruction outcomes, as quantified by the Fourier ring correlation (FRC), which consistently exceeds the half-resolution criterion.

Importantly, the optimized scattering strength analysis illustrates that an appropriately selected lattice strength is crucial. While choosing stronger lattice scattering generally aids the recovery of weaker signals, optimal lattice strength becomes especially critical when sample signals are relatively weak compared to the background. This insight provides clear guidance for future experimental design, emphasizing the careful tailoring of lattice references to specific experimental conditions and biological samples. Experimentally, the fabrication of tailored 2D lattice structures, potentially employing advanced lithography or colloidal self-assembly techniques, will be a critical step in practically realizing this technique.

In conclusion, our proposed lattice-based holographic SPI framework significantly expands the feasibility of high-resolution single-particle imaging at synchrotrons. By effectively mitigating background and optimizing data acquisition, this approach could enable routine structural characterization of sensitive biological samples, opening new avenues for in situ investigations of biomolecular dynamics under near-native conditions.

Although the current study is limited to 2D numerical simulations, our method naturally extends to 3D reconstructions. Extending would introduce additional latent parameters, including 3D orientations and positions along the beam axis, thereby increasing computational complexity, which still can be handled by the algorithm.

6

Holographic-SPI Experiment

Author Contributions:

Kartik Ayyer conceived the project. Abhishek Mall, with assistance from Parichita Mazumder, prepared the samples. Kartik Ayyer and Abhishek Mall conducted the beamtime experiments with assistance from Tamme Wollweber, Shen Zhou, Parichita Mazumder, and beamline staff. Authors acknowledge MaxIV in Lund, Sweden for provision of beamtimes at NanoMax beamline.

6.1 Abstract

This chapter discusses two synchrotron-based experiments aimed at investigating lattice-enhanced holographic SPI. We utilized 2D crystal reference structures: (i) a self-assembled monolayer of polystyrene nano-spheres and (ii) lithographically patterned crossed gratings — to amplify weak scattering signals from individual biological particles and nanoparticles. By leveraging coherent interference between the structured reference and the sample, modulations in Bragg peak intensities were analyzed to extract structural information from target objects, procedure discussed in Chapter 4 and 5. Despite challenges, particularly in synthesizing high-quality lattices to minimize variations that could overshadow the modulations induced by the target particle, preliminary results demonstrate the feasibility of method and suggest pathways for further optimization.

6.2 Overview

The primary objective of the experiment was to enable SPI at synchrotrons by utilizing coherent amplification from 2D lattices. Conventional SPI is limited by radiation damage and background scattering, which hinder high-resolution structural reconstruction for many biological samples.

Our approach employed crystalline 2D lattices as structured holographic references. When illuminated by a coherent X-ray beam, these lattices generate high-contrast Bragg peaks. The presence of a target object, such as a virus or nanoparticle, induces interference between its scattered wave and the lattice's periodic wavefield, modulating the Bragg peaks. These modulations encode structural information about the object, even in noisy conditions.

The experiments were conducted at the NanoMAX beamline of the MAX IV synchrotron. The first experiment utilized self-assembled monolayer of polystyrene nano-spheres as the reference, while the second employed lithographically patterned crossed gratings. Both experiments aimed to demonstrate reference-enhanced imaging of gold nanoparticles (test objects) and biological samples (primary target objects), assessing the technique's efficacy under realistic synchrotron conditions.

6.3 Samples

Two 2D lattice configurations were tested to be employed as strong scattering *references*:

- 1. **Self-Assembled Polystyrene Nanospheres:** A monolayer of 100 nm and 200 nm diameter polystyrene (PS) nanospheres was self-assembled on a silicon nitride (Si_3N_4) membrane to form a 2D periodic lattice. The opposing membrane face was dispersed with target objects: spherical AuNPs (50 nm and 80 nm), MS2 bacteriophage, and tobacco mosaic virus (TMV).
- 2. Crossed Lithographic Gratings: A pair of orthogonal silicon nitride gratings (100 nm pitch, ~25 nm bar width), fabricated via EUV interference lithography, served as high-quality periodic references. Target Samples included − 80 nm AuNPs, TMV, and virus-like particles (VLPs) − were deposited on a thin membrane situated within the X-ray focal depth, downstream of the crossed gratings.

Each system was designed to maximize coherent interference between the

structured reference and weakly scattering particles, enhancing signal extraction even in the presence of background noise.

The gratings were manufactured by Eulitha and Si_3N_4 were ordered from Norcada.

6.3.1 Synthesis and Deposition

PS Lattice Formation

The self-assembled PS nanosphere monolayers were prepared using a modified air—water interface method, as inspired by techniques reported in [203] and subsequent adaptations. The deposition procedure followed an optimized protocol developed at Brewster Angle Microscope (BAM) provided by Kibron Inc., with final adjustments made based on prior studies [207] The Langmuir-Blodgett (LB) method was used to transfer monolayer colloidal crystals from the air-water interface to the substrate (see Figure 6.1a). The setup was provided by Kibron Inc.

A 1:2 mixture of 2% w/v PS nanosphere suspension (100 nm or 200 nm diameter) and ethanol was used. A total of 30 μ L was transferred dropwise (2 μ L per drop) onto a glass slide positioned above a water surface. Each droplet was allowed to spread slowly and transfer to the water–air interface, avoiding splashing and shockwaves that could disrupt monolayer formation. Drops were dispensed at 2-second intervals to promote even spreading and to facilitate controlled flake growth.

Following deposition, the monolayer was compressed at a controlled rate of 10 mm/min for approximately 35 minutes until fault lines appeared. Compression was then reduced to 2 mm/min or paused during the final transfer onto the Si_3N_4 membrane. This protocol was initially optimized on a silicon wafer before being applied to the Si_3N_4 membrane. Target object particles were dispersed on the opposite side of the membrane (Figure 6.1b). The Si_3N_4 membrane was mounted in a sample holder for fixed-target delivery into the X-ray beam (Figure 6.1c). The quality of the PS nanosphere monolayer was evaluated using scanning electron microscopy (SEM). SEM images of the monolayer, shown in Figure 6.1d-e, depict nanospheres with diameters of 100 nm and 200 nm, respectively. The 200 nm PS monolayer exhibits relatively better ordering compared to the 100 nm monolayer, though both display grain boundaries resulting in small ordered domains.

The air-water interface method is well established for producing high-quality monolayer colloidal crystals with enhanced uniformity and domain size [203, 208]. Incorporating ethanol into the colloidal suspension improves spreading by lowering

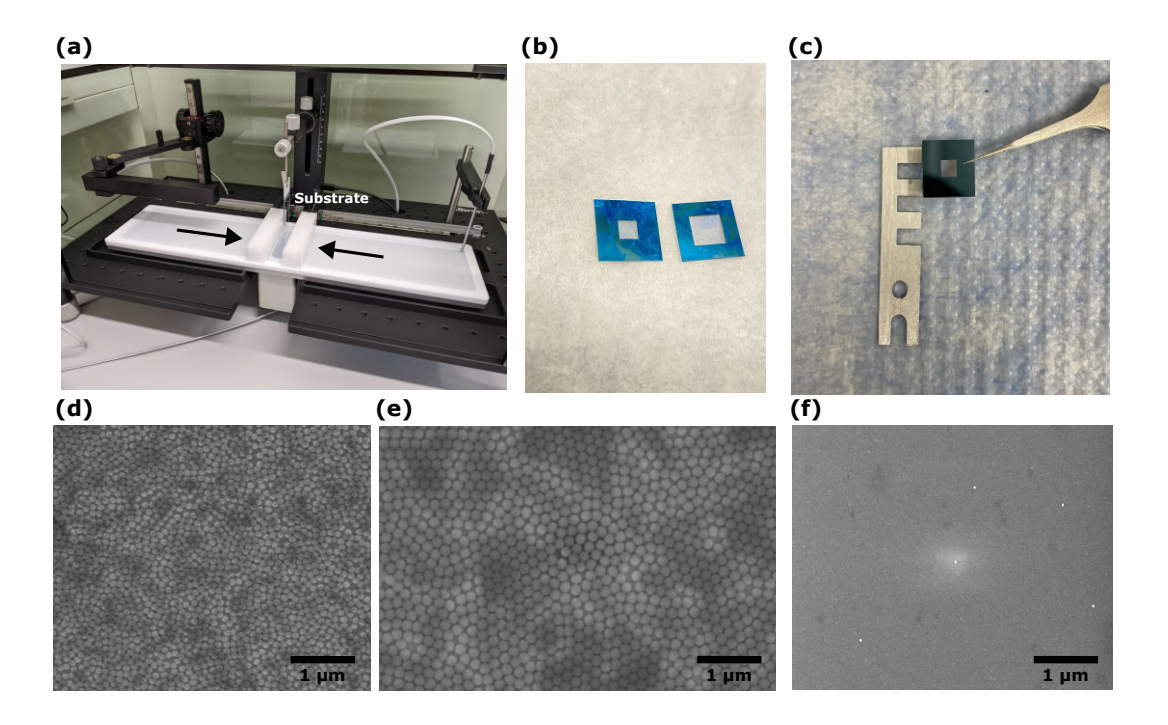


Figure 6.1: **PS Monolayer and Sample Preparation.** (a) Langmuir-Blodgett setup used to form a monolayer of polystyrene (PS) nanospheres at the air—water interface and transfer it onto a Si_3N_4 substrate. (b) Si_3N_4 substrates with varying transparent window sizes, featuring a PS nanosphere monolayer on one side and dispersed target particles on the opposite side. (c) Custom sample holder for mounting the Si_3N_4 substrates, enabling fixed-target delivery of the lattice and target particles into the X-ray beam. (d, e) SEM images of PS nanosphere monolayers with diameters of 100 nm and 200 nm, respectively. (f) SEM image of 80 nm gold nanoparticles (AuNPs).

surface tension [208, 209]. The droplet-by-droplet deposition approach adopted here aligns with best practices for minimizing convective instabilities and enabling controlled self-assembly [210]. Additionally, precise control of the compression rate is critical, as surface pressure directly influences monolayer integrity and defect formation during transfer [211]. The resulting SEM-evaluated film morphologies are consistent with previous reports [212]. These combined refinements setup the protocol of our PS lattice formation for preparing well-ordered nanospheres monolayer.

Deposition of Gold Nanoparticles

AuNPs with diameters of 50 nm and 80 nm were deposited onto the Si_3N_4 membrane side opposite the PS lattice. Prior to deposition, the AuNPs were diluted in MilliQ water to final dilutions of 1:1, 1:100, and 1:1000. To improve dispersion, samples

were sonicated for 30 minutes. Drop-casting was performed by applying a small volume of the suspension directly onto the membrane surface, followed by air drying at ambient conditions.

Among various solvent systems tested, citrate-buffered AuNPs were found to be most compatible, particularly for 50 nm particles. Chloroform-based preparations proved immiscible, and PBS-buffered AuNPs showed reduced adherence or aggregation. Particle density was empirically determined to be approximately 0.42 particles/ μ m² for a 1:10 dilution, based on SEM characterization. Figure 6.1f show SEM image of isolated AuNPs of diameter 80nm deposited on Si₃N₄, illustrating coverage density and particle dispersion.

Deposition of Biological Targets

MS2 bacteriophage, TMV, and virus-like particles (VLPs) were deposited using methods similar to those applied for AuNPs, though the handling of biological targets was subject to more stringent control to prevent degradation. Virus samples were drop-cast from dilute buffer suspensions and allowed to air-dry under clean, low-humidity conditions. Due to their weak scattering contrast and susceptibility to damage or aggregation, their visibility in diffraction data was strongly dependent on experimental noise conditions and background minimization. The SEM and Atomic Force Microscopy (AFM) did not yield high-quality characterization of the biological samples, most likely due to suboptimal dispersion on the substrate.

6.4 Results

Self-Assembled PS Lattice

Approximately 4,770 diffraction patterns were collected over 40 hours using an 8 keV X-ray beam focused to $1\times 1~\mu\text{m}^2$, with the Eiger 1M detector positioned 3.5 m downstream. Each exposure lasted 30 s, with a flux of 9×10^8 photons/s. The primary dataset comprised 200 nm PS lattices with 50 nm and 80 nm AuNPs.

The self-assembled PS lattice produced well-defined Bragg peaks due to high ordering.

A subset of 3,380 patterns (200 nm PS with 80 nm AuNPs) was selected for further analysis.

Figure 6.2 summarizes key characteristics of the collected diffraction data. Panel (a) displays the average background signal, acquired from the beamline setup

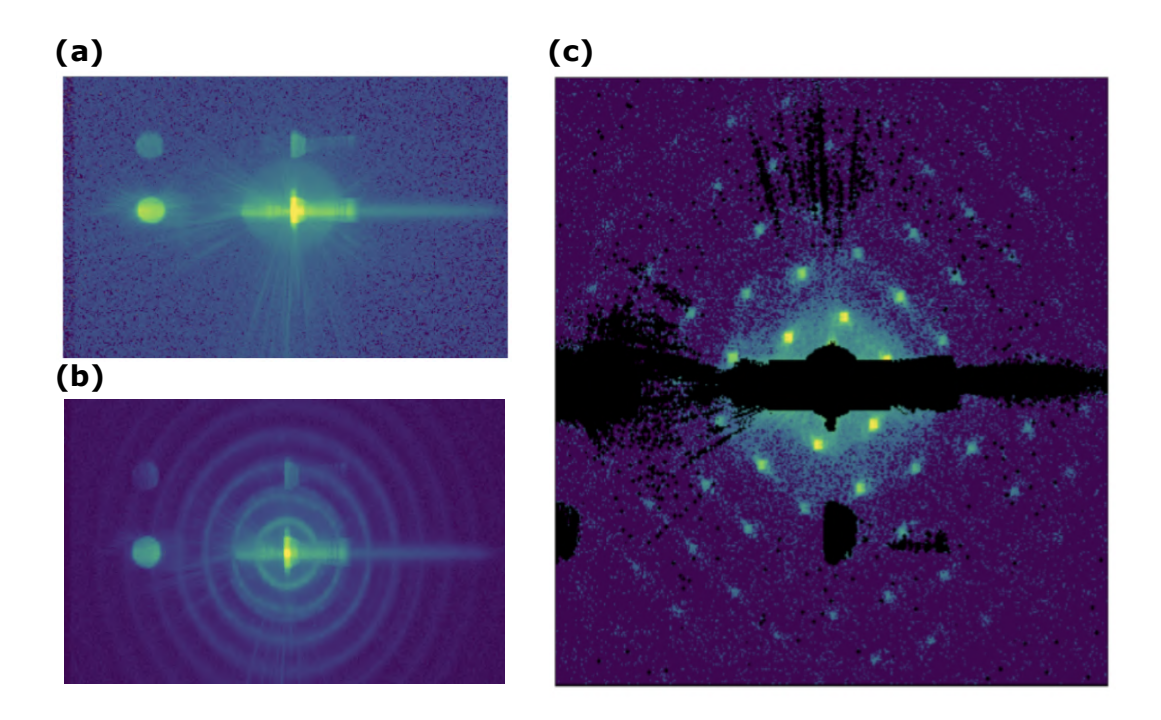


Figure 6.2: **Diffraction Data.** (a) Average scattering background from the beamline and the air-exposed $\mathrm{Si_3N_4}$ window setup without samples. (b) Powder diffraction pattern, obtained by integrating all diffraction images collected from various regions of interest for a 200 nm PS nanosphere lattice. The central spot corresponds to the maximum intensity. (c) Preliminary evaluation of a dataset collected from a 200 nm PS lattice with 80 nm AuNPs as target objects. Single 30-second exposure from a 2D crystal of 200 nm PS nanospheres, showing holographic modulation induced by the AuNPs. Dark regions are masked due to strong background scattering from the beamline.

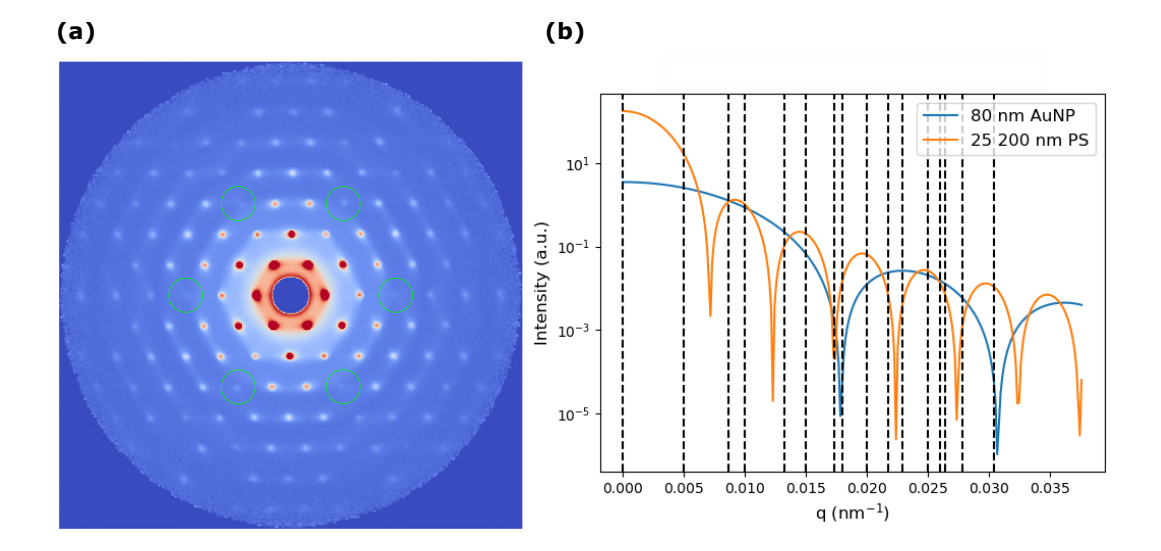


Figure 6.3: **Holographic Enhancement.** (a) Average intensity from 500 aligned diffraction patterns. Holographic interference causes intensity variation between otherwise symmetry-related peaks. This is visually most apparent in weak peaks as shown in green circles. (b) Simulation of 200 nm PS with 80 nm AuNPs as target objects. Intensity vs q for single 80 nm AuNP vs 25 PS spheres (200 nm). The vertical dotted lines are positions of different order of Bragg peaks.

without a sample, highlighting contributions from air scattering and the Si_3N_4 window. This background was subtracted from subsequent measurements.

Panel (b) shows the powder-averaged diffraction pattern of the self-assembled 200 nm PS lattice, revealing a series of well-defined Bragg rings indicative of certain degree of ordering. The central intense spot, which appears overexposed, reflects the direct beam region where no beamstop was used.

In panel (c), a single-exposure diffraction pattern from a 200 nm PS lattice embedded with 80 nm AuNPs exhibits modulations superimposed on the Bragg peaks. These features suggest holographic interference from the AuNPs; however, interpretation was limited by variability in the illuminated domains of PS monolayer. Since the X-ray beam scanned different regions of the monolayer from shot to shot, short range domain boundaries and inhomogeneities in the PS lattice structure introduced inconsistencies that obscured the subtle modulation from the target particles. As a result, many diffraction patterns could not be reliably merged or analyzed to extract a coherent signal from the AuNPs.

A 2D expectation-maximization analysis on this dataset reveals a class of diffraction pattern with 500 patterns aligned showing the signs of modulation present on bragg peaks (Figure 6.3a) . The modulation from the first ring of AuNP sphere resides on the bragg peaks present at that radial distance from the center. This

effect is more prominent on the weak peaks (circled in green, Figure 6.3a).

Figure 6.3b, a preliminary simulation of the experimental setup illustrates the occurrence of modulation due to holographic interference of 2D lattice and AuNP target object. For simplicity, we model 2D lattice of 25 PS spheres stacked together in the interaction region. The radial average depicts the distance from the center where the maxima from reference and target object interfere. The effect is more extractable near the peaks at $q\approx 0.022\ nm^{-1}$.

Crossed Lithographic Gratings

Over 200,000 patterns were collected in 72 hours with exposure times between 0.1–5 s. An improved beamline configuration delivered \sim 50× greater flux than previous experiment, enabling shorter exposures.

Lithographically defined gratings offered nearly 100% diffraction efficiency across frames. Only seam regions in the gratings generated excessive diffuse scattering (Figure 6.4b). Unlike the self-assembled PS spheres, these gratings showed low polydispersity and large coherent domains.

However, frame-to-frame intensity fluctuations arose due to small variations in grating bar widths. These fluctuations obscured modulation signals from weak scatterers such as TMV and VLPs. Hit-finding was successful for AuNPs, but not sensitive enough for biological particles.

Figure 6.4 illustrates these aspects of the crossed grating experimental setup and representative diffraction results. Panel (a) shows a schematic of the beamline configuration with the dual-grating geometry and sample integration. The inset highlights the fixed-target delivery system used for precise sample positioning.

Panel (b) presents an SEM image of one of the lithographically patterned gratings, with a visible stacking fault where two regions intersect and subtle width variations; such defects were the primary source of overshadowing the modulation of the Bragg peaks from the target particles. The inset in (b) quantifies this background in the absence of a sample, demonstrating its minimal impact outside seam areas. Panels (c) and (d) show single-exposure diffraction images from individual AuNPs and AuNP dimers, respectively, collected using the crossed grating configuration. In both cases, distinct diffuse scattering are visible.

However, one difficulty which remains is that we are still highly sensitive to imperfections in the grating "bars". Nominally, the lattice period was 100 nm and the bars were 25 nm. If this was the case, then the 4th order (100/25) peak would be absent. But in Figure 6.5, we see how the grating bar width varies somewhat

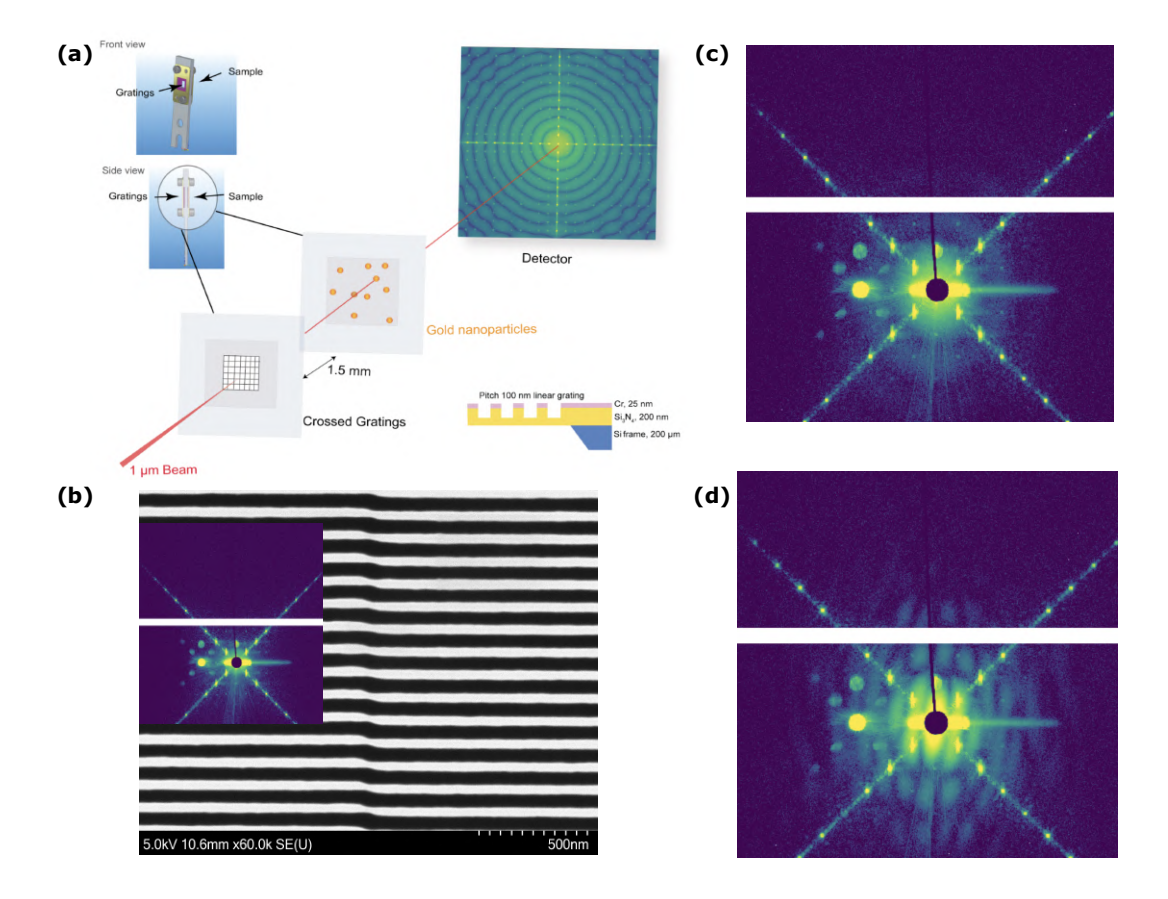


Figure 6.4: Crossed Grating Setup and Diffraction Data. (a) Schematic of the experimental setup: two crossed gratings generate a periodic exit wave that is subsequently modulated by the sample. The inset shows the fixed-target sample delivery configuration and grating specifications. (b) SEM image of one of the EUV interference lithography gratings, highlighting a stacking fault at the intersection of two regions. Inset: average background scattering from the beamline and the air-exposed dual-grating window setup without a sample. (c) Single 10-second exposure showing diffraction from an individual AuNP with crossed gratings. (d) 100-second exposure of an AuNP dimer under the same configuration. In both (c) and (d), the diffuse signal is sufficiently strong to reveal the particles.

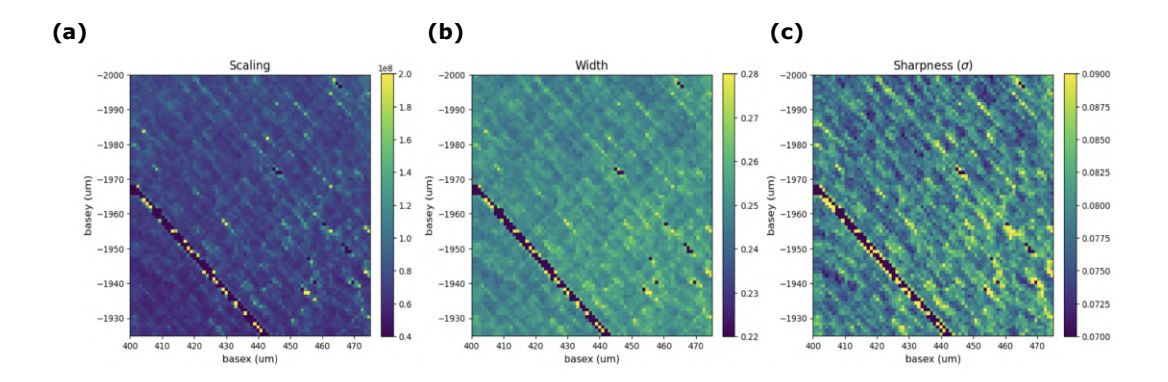


Figure 6.5: **Imperfections in Gratings.** Scan of 2D Grating with empty SiN membrane with exposure time of 2 sec. A total of around 5000 frames were collected for characterizing (a) Brightness scaling (b) Relative bar width (0.25 on average) (c) Sharpness of average profile, which reflects the degree of variations within the focal spot.

randomly over the whole lattice. A necessary improvement in the setup would be to have the X-rays hit the same part of the grating for every frame and only the sample membrane be scanned.

Figure 6.5 presents an analysis of imperfections in a 2D grating patterned on an empty silicon nitride (SiN) membrane. The dataset comprises approximately 5000 frames, acquired under a 2-second exposure time, to characterize key structural and optical features of the grating. Three main parameters are analyzed. (a) Brightness Scaling: It illustrates the variation in detected brightness across the grating, which may arise due to non-uniform illumination, fabrication defects, or material inconsistencies. (b) Relative Bar Width: The average relative width of the grating bars is found to be around 0.25, indicating the periodic spacing and uniformity of the grating lines. Deviations from this average provide insight into fabrication tolerances and alignment precision but can also introduce fluctuations in scattered signal from these artefacts. (c) Sharpness of Average Profile: It quantifies the focus quality and local uniformity within the grating pattern. Reduced sharpness suggests local deformations or imperfections in the grating or membrane, which can impact optical performance. Together, these metrics help assess the structural integrity and optical uniformity of the fabricated grating, critical for high-precision applications.

These fluctuations became significant from frame to frame as we scanned both the grating and the sample simultaneously. Diffraction measurements with a fixed reference and a scanned sample would be more effective for accurately characterizing the reference signal in each frame, thereby minimizing the prominent variations observed when moving across the grating.

6.5 Discussion

These experiments collectively validate the feasibility of lattice-enhanced holographic SPI at synchrotron sources. In the experiment with PS nanosphere lattices, interference between the PS lattice Bragg peaks and AuNPs confirmed coherent enhancement. The results demonstrated that the modulation amplitude is sensitive to both the particle size and its location within the unit cell.

Additionally, the experiment involving crossed gratings yielded significantly higher data quality. However, intrinsic imperfections in the grating structure introduced modulations unrelated to the sample, which hindered the detection of weakly scattering viruses.

In our current experiment, both the lattice and the sample were scanned simultaneously, which introduced unwanted variation from the uncertainties in reference structure. To mitigate this, future implementations in sample delivery should fix the lattice and scan across dispersed side with the sample, thereby minimizing modulation artifacts arising from spatial inhomogeneities within the reference. It is critical that the modulation signal from the target object exceeds the signal introduced by lattice uncertainty or imperfections.

In well-characterized gratings, such variations could be nearly negligible. Computationally, however, the reference used here could be modeled using Markov Chain Monte Carlo (MCMC) methods as discussed in [134]; however, these models can become unstable or intractable if too many free parameters need to be evaluated for characterization.

To improve the method's viability, we recommend the following:

- To reduce structural noise originating from different regions on the reference, fix the illuminated reference region across exposures. This can be achieved by maintaining a fixed reference along the beam path while scanning only the dispersed samples.
- Improve the quality of holographic reference through fabrication, if possible, to minimize intensity fluctuations from defects or disorders. This was observed to be an improvement when transitioning from PS monolayers to 2D gratings. A high-quality grating with fewer structural uncertainties will help ensure that any extraneous signals remain smaller than the Bragg peak modulations from the target particle.

With these improvements, lattice-enhanced SPI could become a practical tool

at synchrotron facilities for biomolecular imaging, allowing for the determination of 3D structures of biological macromolecules under near-native conditions.

Summary and Outlook

In this dissertation, we have applied SPI methodologies and developed novel experimental configuration to investigate the structure and dynamics of nanoscale systems under a range of experimental conditions. In Chapter 3, we presented the first observation of aerosolization-induced morphological changes in MS2 bacteriophage capsids, revealing an incoherent buckling transition that likely serves to protect viral capsids from dehydration [132]. In Chapter 4, we introduced a maximum-likelihood phasing algorithm (MaxLP) for gold nanoparticle (AuNP)—enhanced holographic SPI approach, demonstrating sub-nanometer resolution reconstructions even in the low-signal, heterogeneous data regime [35]. Finally, in Chapter 5 and Chapter 6, we extended holographic SPI to synchrotron sources by employing a 2D crystal lattice as a strongly scattering reference, enabling high-resolution imaging under extreme background conditions — up to five orders of magnitude stronger than the sample signal. We demonstrated the experimental feasibility using two lattice reference examples.

Together, these studies advance both the experimental and computational capabilities of SPI, significantly broadening its applicability across biological, materials, and aerosol science.

Structural Dynamics of Viral Capsids

Using SPI in combination with machine learning techniques, we directly visualized a novel compact capsid conformation and intermediate morphologies of the MS2 bacteriophage under dehydration stress (Chapter 3). Machine learning—based classification of hundreds of thousands of diffraction patterns enabled mapping of a continuous structural landscape, revealing that a single 19-residue loop under-

goes localized destabilization, triggering an incoherent buckling transition. These findings provide the experimental observation of shape transitions in icosahedral viruses and highlight the potential of integrating SPI with unsupervised deep learning approaches to resolve subtle conformational heterogeneity [134, 136].

AuNP-Enhanced Holographic SPI

In Chapter 4, we addressed the fundamental resolution and signal-to-background limitations of conventional SPI by attaching a strongly scattering gold nanoparticle (AuNP) to a target object mimicking a biological object. To enable robust structure recovery under low-signal conditions, we developed the MaxLP algorithm, which combines maximum-likelihood estimation with a pattern search strategy to jointly recover object Fourier amplitudes and latent experimental parameters—including particle orientation, AuNP size, and relative shift. MaxLP performs reliably even at photon counts as low as \sim 2,000 photons per frame. Simulations demonstrated that MaxLP outperforms previous divide-and-concur approaches in the low-signal regime and naturally converges to the ensemble-average structure in the presence of conformational heterogeneity [35, 171].

Lattice-Enhanced Holographic SPI

Chapter 5 and Chapter 6 extended holographic SPI to synchrotron beamlines by introducing a fixed-target configuration with a fabricated 2D crystal lattice serving as a periodic reference. The sharp Bragg peaks generated by the lattice enhance interference with weak biomolecular scattering, enabling recovery of particle signals even when the background intensity exceeds the object signal by a factor of 10⁵. We developed an iterative grid-search optimization algorithm that jointly retrieves the target object's electron density, orientation, in-unit-cell shift, and fluence. Under realistic exposure and noise conditions, this approach achieved reproducible reconstructions with Fourier ring correlation (FRC) values exceeding the 0.5 threshold [36]. We experimentally demonstrate by utilizing 2D crystal reference structures: (i) a self-assembled monolayer of polystyrene nano-spheres and (ii) lithographically patterned crossed gratings — to amplify weak scattering signals from individual biological particles and nanoparticles. By leveraging coherent interference between the structured reference and the sample, modulations in Bragg peak intensities were analyzed to extract structural information from target objects.

Ongoing upgrades at XFELs and fourth-generation synchrotrons promise enhanced spatial coherence and increased per-pulse flux, opening the door to subnanometer resolution in SPI [213, 214]. In the viral system discussed in Chapter 3, femtosecond pump-probe schemes could capture real-time capsid dynamics through hydration, offering molecular-timescale insight into hydration-driven structural transitions with a controlled pump. Similarly, incorporating AuNP or lattice references into time-resolved SPI experiments could reveal ultrafast conformational pathways in proteins.

While spherical AuNPs and 2D crystal lattices are simplistic choice of references, future work should explore optimized holographic references—such as uniformly redundant arrays (URAs) or tailored nanofabricated masks — that provide broadband, high-angle scattering [130]. These engineered references could maximize phase-contrast modulation while minimizing parasitic background, extending SPI to smaller or more weakly scattering biomolecules.

Our preliminary demonstration that MaxLP recovers real-space averages in the presence of heterogeneity (Chapter 4) suggests a path toward continuous conformational mapping without the need for discrete classification. By embedding additional latent variables into the MaxLP framework — similar to the continuous latent models used in cryoDRGN [171] — it may be possible to reconstruct structural ensembles directly from diffraction data, enabling better resolution for dynamic molecular states.

The ability to image dehydrating viruses under near-ambient conditions has direct implications for understanding airborne pathogen stability and transmission. Extending the MS2 study to clinically relevant viruses such influenza and SARS-CoV-2 could uncover fundamental mechanisms of aerosol viability and inform public health strategies.

The lattice-enhanced holographic SPI method developed in Chapter 5 and Chapter 6 offers a practical blueprint for routine biological imaging at widely accessible synchrotron beamlines. The integration of high-throughput fixed-target stages with embedded lattices—possibly — could enable automated, large-scale SPI experiments across diverse biomolecules. Currently 2D simulation demonstration has shown it's potential, extending introduced algorithm to 3D problem could be enable GPU-acceleration.

Widespread adoption of holographic SPI will also depend on the development of robust, open-source software implementing MaxLP and related algorithms. These tools should feature user-friendly interfaces and seamless integration with existing SPI workflows such as Dragonfly [7]. The collaborative development of bench-

mark datasets and standardized validation protocols will be critical for ensuring cross-platform reproducibility and accelerating community-wide progress.

In summary, the techniques developed in this thesis unlock new capabilities for imaging nanoscale systems under previously inaccessible conditions. By combining machine learning, holographic references and advanced reconstruction algorithms, we have laid the groundwork for a new era of SPI — one in which dynamic, heterogeneous and weakly scattering biological assemblies can be visualized at near-atomic resolution in their native environments. The challenges ahead—from reference design to time-resolved implementations—present rich opportunities for innovation at the intersection of physics, biology and data science.

Supplementary

≺ This chapter provides additional methodological details on data analysis, and supporting figures that expand upon the results presented in Chapter 3 of this dissertation. The content herein is intended to offer deeper technical insight and ensure reproducibility of the work described.
 ≻

8.1 Sample Preparation.

E. coli strain C-3000 (*ATCC 15597*) was cultured in volumes of 50 ml at 37°C with shaking at 150 rpm. Shaking was reduced to 90 rpm when the exponential growth phase was reached, and the culture was infected with $100\,\mu\text{L}$ MS2 ($2.9\,\text{mg}\,\text{mL}^{-1}$, $\varepsilon_{280}=3.86\,\text{mg}\,\text{mL}^{-1}$) (*ATCC 15597-B1*) and $100\,\mu\text{L}$ CaCl₂ (1 M). Incubation was stopped when the cells were lysed (c. 3 hours). One milliliter of the lysate and $800\,\mu\text{L}$ CaCl₂ was used to infect $400\,\text{mL}$ of exponential phase growth culture of E. coli. Incubation was carried out with shaking at 90 rpm until the cells were lysed (ca. 5 hours). The lysate was precipitated using 10% (w/v) PEG 6000 and 0.5 M NaCl over 48 hours at $4\,^{\circ}\text{C}$.

After precipitation, the suspension was centrifuged at $10\,000\,\mathrm{g}$ for 30 min. The pellet was re-suspended in $30\,\mathrm{mL}$ 0.01 M Tris, pH 7.5 (containing 0.1 M NaCl, 0.1 mM MgCl₂, and 0.01 mM EDTA). Stirring was carried out for 1 hour at room temperature until complete re-suspension. Next, the suspension was incubated at $37\,^\circ\mathrm{C}$ with shaking at 120 rpm after adding 1.5 mg lysozyme, $300\,\mu\mathrm{L}$ MgCl₂ (1 M), and $10\,\mu\mathrm{L}$ Benzonase. After incubation, the suspension was centrifuged at $8000\,\mathrm{g}$ for 30 min. The supernatant was precipitated using 10% (w/v) PEG 6000 and 0.5 M

NaCl and incubated at $4\,^{\circ}\text{C}$ overnight. The suspension was centrifuged at $27\,000\,\text{g}$ for 30 min, and the pellet was re-suspended in Tris buffer. The re-suspension was applied to a sucrose gradient (15-50%) and centrifuged at $40\,000\,\text{g}$ for 18 h at $4\,^{\circ}\text{C}$. The sucrose in the collected band fractions was removed by repetitive concentration and dilution steps with Tris buffer using an Amicon Ultra Centrifugal Filter (100 kDa cutoff).

Prior to cryo-EM grid preparation and sample injection at the XFEL, the Tris buffer of the sample was exchanged to a buffer containing 0.2 mM sodium citrate and 5 mM ammonium acetate using a PD Minitrap G-25 column (Cytiva). The sample concentration was adjusted to $\sim 2\times 10^{15}$ particles/mL (or \sim 12 mg/mL) for both experiments.

8.2 Cryo-EM structure determination

An aliquot (3 μ L) of MS2 virions was deposited onto freshly glow-discharged, 300 mesh R2/2 Quantifoil grids, followed by 3 s of blotting at 4°C and 95% humidity using a Vitrobot Mark IV instrument (ThermoFisher Scientific). The blotted grid was plunge-frozen into a 37:63 (v/v) liquid ethane/propane mixture. Images were acquired using a Talos Arctica microscope (ThermoFisher Scientific) operated at 200 kV and equipped with a Falcon 3EC detector (ThermoFisher Scientific). A total of 861 movies were recorded using the EPU software (ThermoFisher Scientific) in integration mode at a nominal magnification of \times 92,000, yielding a final pixel size of 1.58 Ų. Each movie had a total dose of 36e-/Ų over 39 frames.

Image processing was performed using cryoSPARC [5]. Drift and beam-induced motions were corrected using patch motion correction, and the contrast transfer function (CTF) was estimated using patch CTF estimation. The micrographs were inspected and curated using the manually curated exposures job, from which 622 micrographs were accepted for further processing. Blob picking was used to pick 60,861 particles, of which 47,546 remained after two rounds of 2D classification. Two classes out of four from *ab initio* reconstruction and heterogeneous refinement (C1 symmetry) had apparent density for both the capsid and the A protein. The particles from these two classes (22,592) were selected for homogenous refinement (C1), where a 4.9 Å resolution map was obtained as estimated by the Fourier shell correlation (FSC) = 0.143 criterion (see Fig. 8.1).

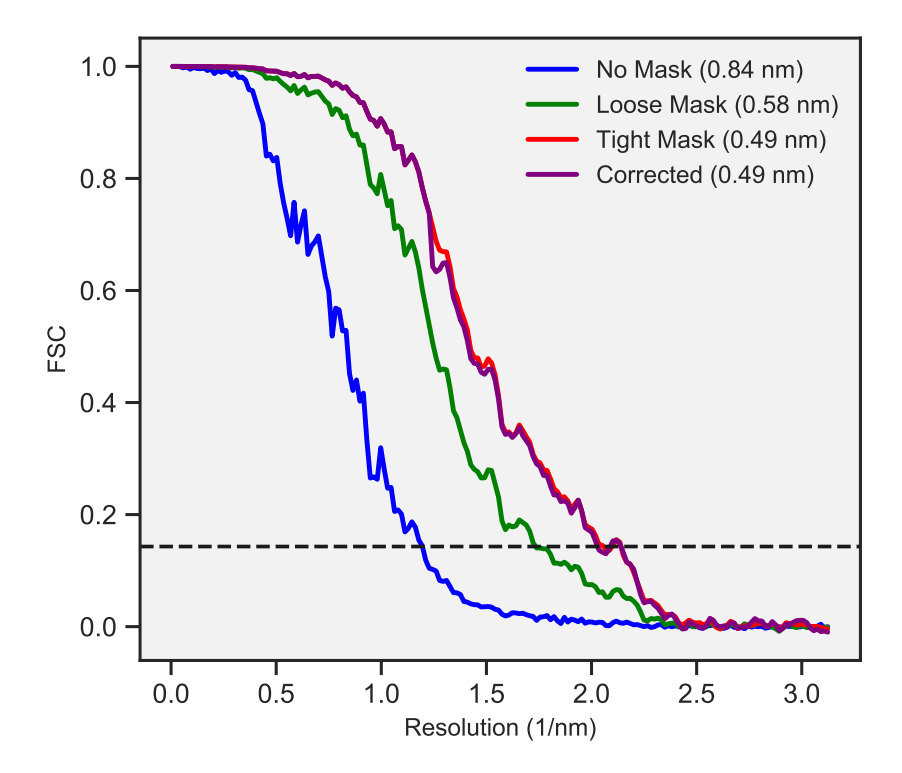


Figure 8.1: **FSC Curve.** FSC curve of the cryo-EM reconstruction generated using cryoSPARC [5] for the cryo-EM reconstruction of the MS2 capsid from the same batch as used for the X-ray SPI experiment. The average resolution of 0.49 nm was estimated based on FSC = 0.143 threshold [6] (black dashed line).

8.3 Classification, Discrete Heterogeneity and Polymorphism

8.3.1 Classification

The first step of data classification was the generation of average two-dimensional (2D) classes in the detector plane from the full diffraction dataset using the 2D classification procedure implemented in Dragonfly [7, 10]. This process employs a modified EMC algorithm to classify all frames into a specified number of averages (models, termed classes in Dragonfly). We began by classifying the dataset into 50 2D classes. Examples of these classes are shown in Fig. 8.2a. The 2D classes corresponding to very weak hits (pink dashed grid) were excluded at this stage.

To obtain the training dataset, a bootstrapping method was employed by running the 2D EMC reconstruction 100 times, each with 100 models, using a random subset of 20% of the frames (from 170 355 diffraction frames) each time, resulting in 10 000 2D intensity models. Size filtering was then applied to the dataset by fitting a spherical object Fourier model to the radial average of the intensity, resulting in a size distribution of 2D intensity models (Fig. 8.2b). By comparing the 2D models and their locations in the distribution, we qualitatively divided the space into three groups, as shown in Fig. 8.2b. In the figure, red denotes icosahedral, blue denotes octahedral, and green denotes contaminants, including outliers and dimers. The corresponding example samples of 2D intensities for different groups are shown in Fig. 8.2c. The top row shows the classes with panel gaps and detector artefacts, which have fitted diameters greater than 40 nm in the distribution. Among all dataset models, 2558 were icosahedral corresponding to 79 771 diffraction frames. These icosahedral 2D intensity models were used for training the β -VAE.

8.3.2 Discrete Heterogeneity

The 2D classification also yielded some interesting structures which had a different symmetry than the icosahedral objects. Figure 8.3a shows some of the 2D intensity averages with reasonable intensity contrast. Note that since intensities are always non-negative, the averages from diverse aggregates and contaminants typically generate low-contrast models. The insets show the projected electron densities resulting from 2D phase retrieval. Only patterns belonging to classes like the "Icosahedral" class were selected for Fig. 3.1d.

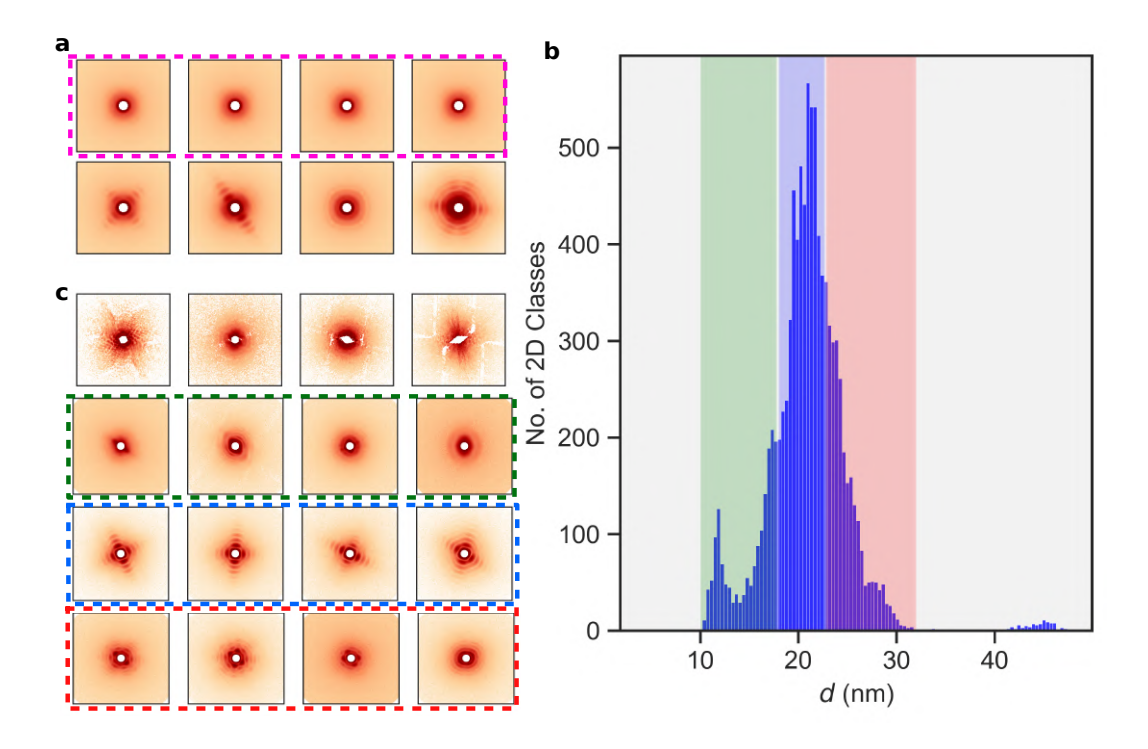


Figure 8.2: **Classification.** (a) Examples from the 50 2D intensity models obtained from the initial EMC classification. (Dashed pink grid) Models rejected prior to generating the training dataset for the β -VAE. (Bottom row) Examples of the 2D intensity models used for the dataset generation. (b) Histogram of the fitted diameters for the 2D intensity classes dataset (10,000 classes). Different structure types are manually marked in the distribution as icosahedral (red), octahedral (blue), and others, including dimers, outliers, etc. (green). (c) The corresponding examples of 2D intensity models for each structure class. (Top row) Examples of classes with panel gaps and detector artifacts, which had fitted diameters > 40 nm.

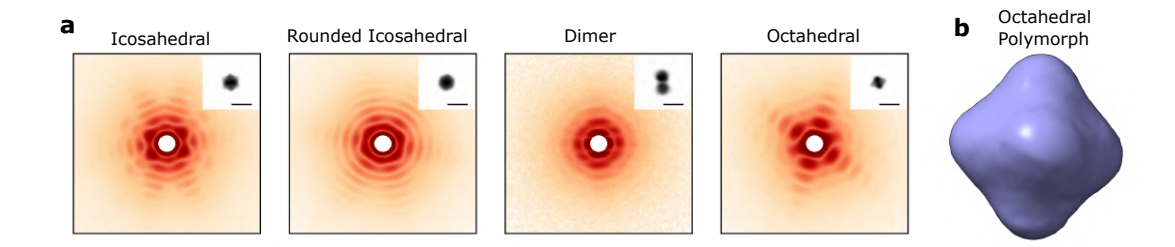


Figure 8.3: **Discrete Heterogeneity.** (a) Examples from the diffraction dataset of 2D intensity models and corresponding electron density projections (inset) via phase retrieval; the scale bar is 30 nm. (b) 3D structure of the MS2 capsid reconstructed from the octahedral data.

8.3.3 Polymorphism

Along with the rounded icosahedra and dimers, we also obtain patterns with clear octahedral structure. The 3D structure of the octahedral particle was reconstructed without any imposed symmetry from $11\,626$ patterns. The reconstructed electron density at $6.1\,\mathrm{nm}$ resolution is shown in Fig. $8.3\mathrm{b}$ and is 1.53 times lower in volume than the icosahedral structure. MS2 capsids have been reported to assemble with octahedral packing and T=3 quasi-symmetry [146, 215]. The primary distinction between icosahedral and octahedral structures lies in the presence of four-fold contacts rather than five-fold contacts, potentially resulting in curved interfaces. The octahedral packing results from the fusion of two coat-protein subunits [216]. These capsids have been reported to disassemble and reassemble into the octahedral structure during crystallisation [146]. To the best of our knowledge, this is the first observation of octahedral MS2 capsids without mutation or different buffer conditions.

8.4 Phase retrieval

The electron densities were reconstructed through a 3D iterative phase retrieval method applied to the full-resolution intensity volume of the MS2 bacteriophage. The procedure was almost identical to the pipeline discussed in [133]. Fig. 1d illustrates the reconstructed electron density obtained for a dehydrated phage. In Fig. 8.4, the phase retrieval transfer function (PRTF) metric, evaluating the reproducibility of retrieved phases based on 128 independent phasing runs for both icosahedral and octahedral structure of MS2 capsid.

The electron density reconstruction from the background-subtracted intensity

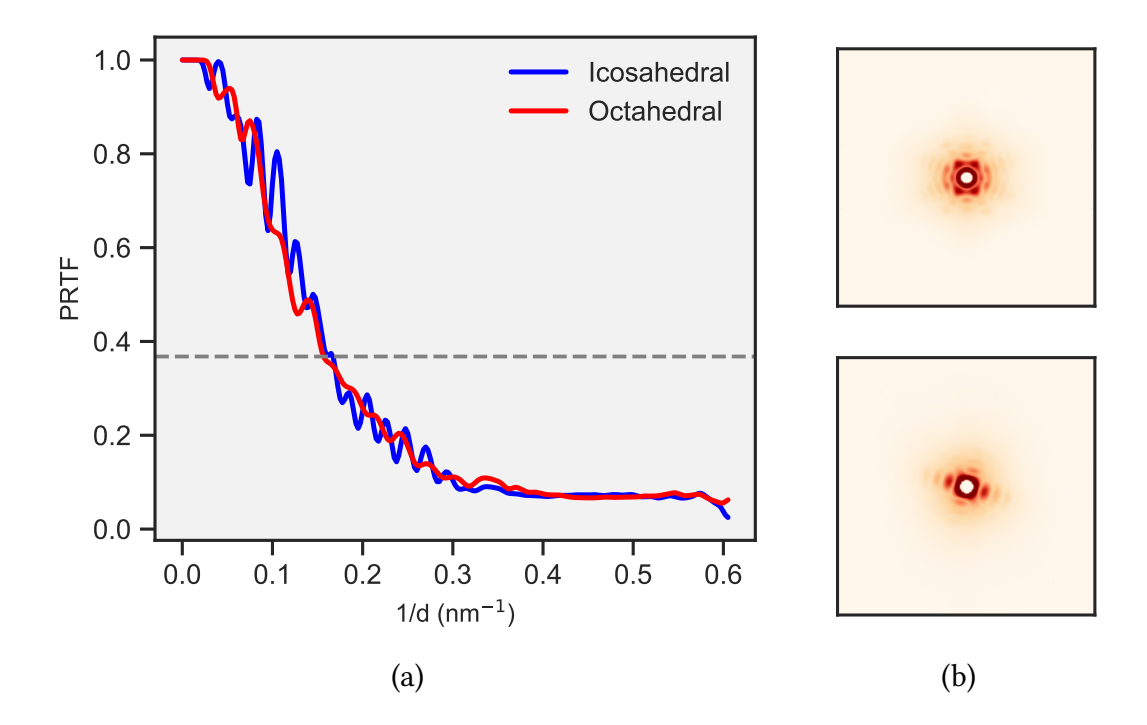


Figure 8.4: **Phase retrieval transfer function (PRTF).** (a) Smoothed phase retrieval transfer function (PRTF) vs q. The solid lines represent the azimuthal average PRTF conventionally used to determine the resolution of the structure. The typical 1/e cutoff is shown in gray. The resolution at the cutoff for both capsid structures was estimated to be ≈ 6.1 nm. (b) Slice at 001-plane through the Fourier volume of the MS2 capsid for icosahedral (top) and octahedral (bottom) structures retrieved using Dragonfly [7]. Fig. 3.1d & Fig. 8.3b shows the corresponding phased electron density.

distribution involved a hybrid approach employing the error reduction (ER) algorithm and the difference map (DM) algorithm. Each phasing run consisted of 400 iterations, comprising 100 ER iterations followed by 200 DM iterations, and concluding with 100 additional ER iterations. The support was updated after each iteration using a smoothing and thresholding procedure, with the strongest $40\,000$ voxels retained in the support.

The phase retrieval process for the reconstructed Fourier volumes by the decoder network for various trajectory points involved 16 random model starts. The number of voxels for the support was determined based on the estimated diameter size and fringe counts in the 3D Fourier volumes. The electron density maps were visualised with radial colouring to depict structural variations.

The density map, crystal structure and SPI densities were visualised using the Chimera software [217].

8.5 Architecture and Training of β -VAE

The β -VAE consisted of an *encoder* and a *decoder* neural network, to encode information into a lower dimension and retrieve it back respectively. The encoder encodes diffraction data (in this case, 2D intensity models) generating a low-dimensional latent vector, Z, for each input pattern \mathbf{X} . The encoder parameterises this distribution with a mean $\mu(\mathbf{X})$ and a variance $\sigma(\mathbf{X})$. During training, this distribution is sampled from a normal distribution $\mathcal{N}(\mu(\mathbf{X}), \sigma(\mathbf{X}))$ before being passed to the decoder, which introduces stochasticity, improving robustness and ensuring smoothness of the latent space.

The network was trained and optimised by minimising a loss function, combining mean square error as a reconstruction loss and Kullback-Leibler (KL) divergence loss as a regularization term, which discourages a too-sharp latent space. In our case, the optimized β -VAE had $\beta=0.5$, with the latent space dimension of Z=2.

8.5.1 Pre-processing

The initial 2D intensities from Dragonfly have dimensions of 503×503 pixels. Preprocessing steps were applied to enhance relevant features and reduce computational redundancy. Given the highly sampled nature of the data and minimal scattering signal at high q, the size was reduced to 171×171 through downsampling and cropping. Additionally, background normalisation was performed by subtracting the mean at high q and dividing by the mean at low q. Considering that diffraction patterns of compactly supported objects are primarily dominated by low q signal, to appropriately weight higher q shape information, the 2D intensities were divided by the radial average intensity over the whole dataset before inputting them into the network. This weighting was then reverted when generating the 3D Fourier volumes. This approach optimises computational efficiency by focusing solely on relevant information in the diffraction data, where distinctive features are evident.

8.5.2 Network Parameters

The encoder network consists of a series of convolutional layers, specifically three Conv2d layers that increase in channel depth from 8 to 32, followed by a sequence of linear layers reducing the dimensionality to a latent space dimension Z. Conversely, the decoder utilizes a symmetrical setup starting from the latent dimension Z, expanding through linear layers, and then upscaling spatial dimensions through

three ConvTranspose3d layers, ultimately reconstructing the input data. Other optimized hyperparameters of the β -VAE include a batch size of 32 and a learning rate of 10^{-4} and weight decay of 10^{-5} for Adam optimizer [218]. The architecture parameters of the β -VAE are detailed in Table 8.1.

8.5.3 Training performance

The β -VAE was trained over a total of 2000 epochs. Fig. 8.5(a) depicts the generative performance of the β -VAE on 2D intensity data at the final epoch. The majority of prominent features are successfully reconstructed in the output, indicating high-quality reconstruction performance. This highlights the effectiveness of the deep learning model in capturing the fundamental attributes inherent in the input data.

Fig. 8.5(b) illustrates the loss of the β -VAE over the final 1000 epochs, during which the orientation was updated every 20^{th} epoch before terminating the training. This approach was adopted because the loss stabilized with no significant changes observed. These stable training dynamics suggest efficient convergence of the VAE and optimization of orientation estimates for each 2D intensity model.

8.5.4 Choosing β and latent space dimensions

Figure 8.5(c) illustrates the VAE training to determine the optimal value of β . The process involved training multiple VAE networks across a range of β values from 0 to 10. The optimal value was chosen based on achieving the minimal loss. The selection of $\beta=0.5$ strikes a balance between smooth disentanglement in the latent space and preservation of reconstruction quality, providing sufficient regularization to prevent overfitting.

Similarly, for latent space dimension Z>2, there was a reduction in MSE loss; however, this improvement did not reveal any new or distinctive features in the latent space. Conversely, Z=2 seemed to effectively encapsulate the variations in the dataset.

Figure 8.5(d) shows the latent space representation color-coded by $\sigma = \sqrt{\sigma_1^2 + \sigma_2^2}$. The low standard deviation values suggest that the network can effectively extract and learn significant features, which are closely correlated and can be accurately reconstructed with minimal uncertainty.

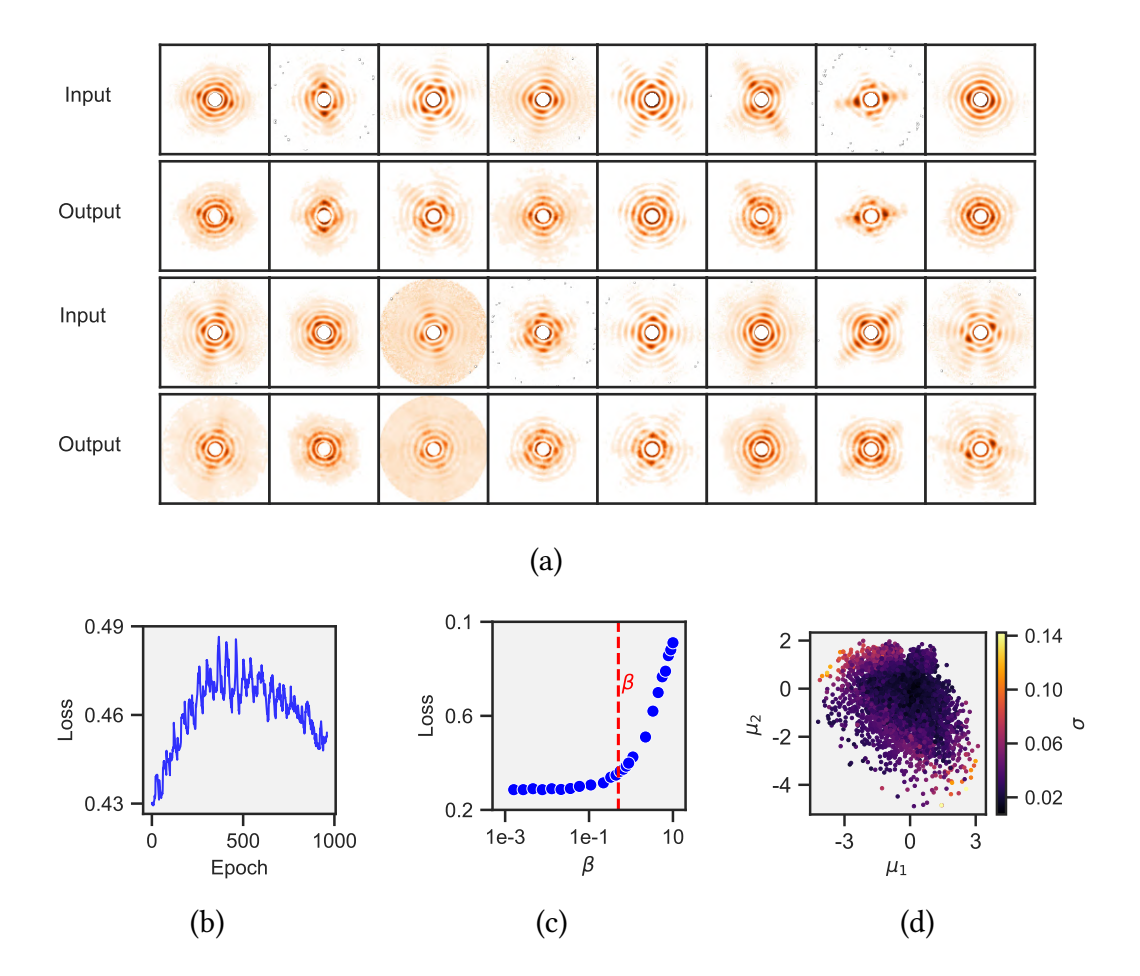


Figure 8.5: **Training of** β **-VAE**. (a) Comparison between input 2D intensity data and the corresponding output (reconstruction) by β -VAE. (b) Loss evolution during β -VAE training exhibited a decline over the 1000 epochs. However, the decrease was not significant later in training, prompting the decision to terminate further training. The depicted loss encompasses both the Mean Squared Error (MSE) loss for reconstruction and the Kullback-Leibler (KL) divergence loss. (c) β -VAE Loss versus β values. The plot illustrates a rise in loss as β values increase. The optimal trade-off between minimizing loss and providing sufficient regularization occurred at $\beta=0.5$ (red dashed line). (d) Latent space representation of the β -VAE color labeled with $\sigma=\sqrt{\sigma_1^2+\sigma_2^2}$.

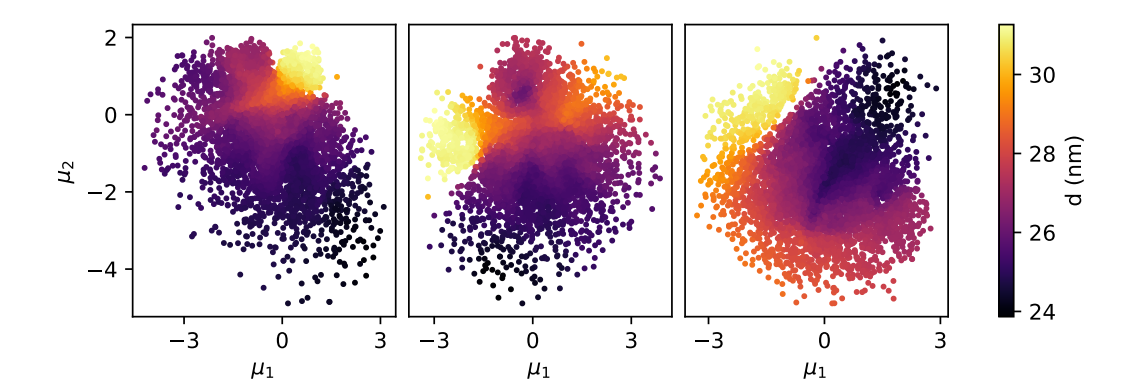


Figure 8.6: Latent Space. Latent space representation of the β -VAE for different random initializations of weight and bias parameters. The low-dimensional embedding varies due to the random start, converging to nearby minima. However, it maintains the same information for shape and size variations.

8.5.5 Stability for different random initialization

Figure 8.6 shows the latent space representation of the β -VAE for three different random initializations of weights and biases. Specifically, random seeds of 42, 61, and 99 were used, respectively. Although the low-dimensional embeddings appear different due to these random initializations, the latent space consistently captures similar information regarding shape and size variation across all three cases. This demonstrates the robustness of the β -VAE in retrieving information from diffraction data despite variations in initial conditions.

8.6 Particle Size Determination

We utilized spherical particle fitting on the Fourier volumes reconstructed by the decoder network of β -VAE. This process involved computing the radial average of the volumes and fitting them with the Fourier model of a spherical particle. This analysis yielded an estimation of the diameter of the MS2 phages during shape-phase transition. The Fourier model for a spherical particle is described by the function S(q,d):

$$S(q) \propto d^6 \left(\frac{\sin(\pi q d) - \pi q d \cdot \cos(\pi q d)}{(\pi q d)^3} \right)^2$$
 (8.1)

where d denotes the diameter of the particle and q is defined with the crystallography convention. The size distribution of MS2 bacteriophage is shown in Fig. 8.7.

Network	Layer	Output Size	Weights	Bias
Encoder	Conv2d (1, 8)	$H/3 \times W/3 \times 8$	$5 \times 5 \times 1 \times 8$	8
	Conv2d (8, 16)	$H/9 \times W/9 \times 16$	$5 \times 5 \times 8 \times 16$	16
	Conv2d (16, 32)	$H/27 \times W/27 \times 32$	$5 \times 5 \times 16 \times 32$	32
	Linear	128	800×128	128
	Linear	64	128×64	64
	Linear	8	64×8	8
	Linear (mean)	Z	$8 \times Z$	Z
	Linear (log variance)	Z	$8 \times Z$	Z
Decoder	Linear	64	$Z \times 64$	64
	Linear	$128 \times 5 \times 5 \times 5$	$64 \times 128 \times 5 \times 5 \times 5$	128
	ConvTranspose3d (128, 64)	$H/3 \times W/3 \times D/3 \times 64$	$5 \times 5 \times 5 \times 128 \times 64$	0
	ConvTranspose3d (64, 32)	$H \times W \times D \times 32$	$5 \times 5 \times 5 \times 64 \times 32$	0
	ConvTranspose3d (32, 1)	$H\times W\times D\times 1$	$7\times7\times7\times32\times1$	0

Table 8.1: Architecture of β -VAE

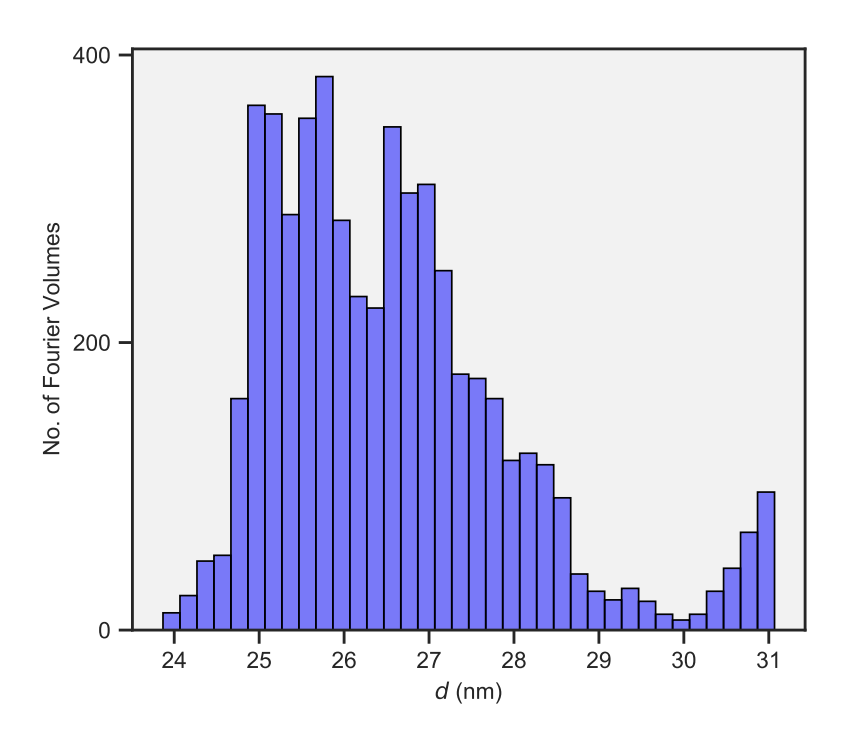


Figure 8.7: **Particle Size Distribution.** Histogram depicting the particle size distribution, represented by fitted diameter values, d (nm). These values were obtained through spherical particle model fitting on the Fourier volumes reconstructed using the decoder network of the optimized β -VAE.

8.7 Local Orientation Optimizer

The Local optimizer updates the orientation (Ω) every 20^{th} epoch during training. To monitor the convergence of orientation estimates, we assess the Root Mean Square Deviation (RMSD) between estimates at consecutive update steps (Fig. 8.8). Convergence is quantified by the measured angle, denoted as Θ , between orientations represented by quaternions at consecutive update steps. Θ is calculated as

$$\Theta = \arccos\left(2\cdot(\mathbf{q}_1\cdot\mathbf{q}_2)^2 - 1\right) \tag{8.2}$$

where \mathbf{q}_1 and \mathbf{q}_2 are the normalized quaternions representing orientations.

The RMSD is computed over these angles to measure the average deviation between orientations across update steps of the Local Optimizer. It is determined as

$$RMSD = \sqrt{\frac{1}{n} \sum_{i=1}^{n} \Theta_i^2}$$
 (8.3)

where n is the number of data samples and Θ_i is the angle between orientations for data sample i at two consecutive epochs.

8.8 Performance of VAE on simulated data

In order to test the VAE architecture on a simulated dataset with similar characteristics, 5000 2D intensity images were generated from heterogeneous particles in random orientations. The particles were uniform density icosahedra of variable size and *roundness*, where the latter was implemented by smoothing and thresholding a faceted icosahedron.

The VAE with 2 dimensional latent space was trained for 500 epochs and terminated as the loss reached a minimal, stable value that no longer changed across epochs. Fig. 8.9(a) illustrates the reconstruction performance of the VAE on simulated 2D intensity data at the final epoch. The majority of features were successfully reconstructed, and the VAE effectively captured the inherent varying features in the input data. Fig. 8.9(b) displays the latent space representation learned by the VAE on the simulated data. The red points correspond to the reconstructed data sample shown in Fig. 8.9(a).

Fig. 8.9(c) presents the distribution of roundness and size parameters used to generate diffraction patterns from the icosahedral particles. This distribution reflects continuous variation in shape and roundness which is controlled by σ .

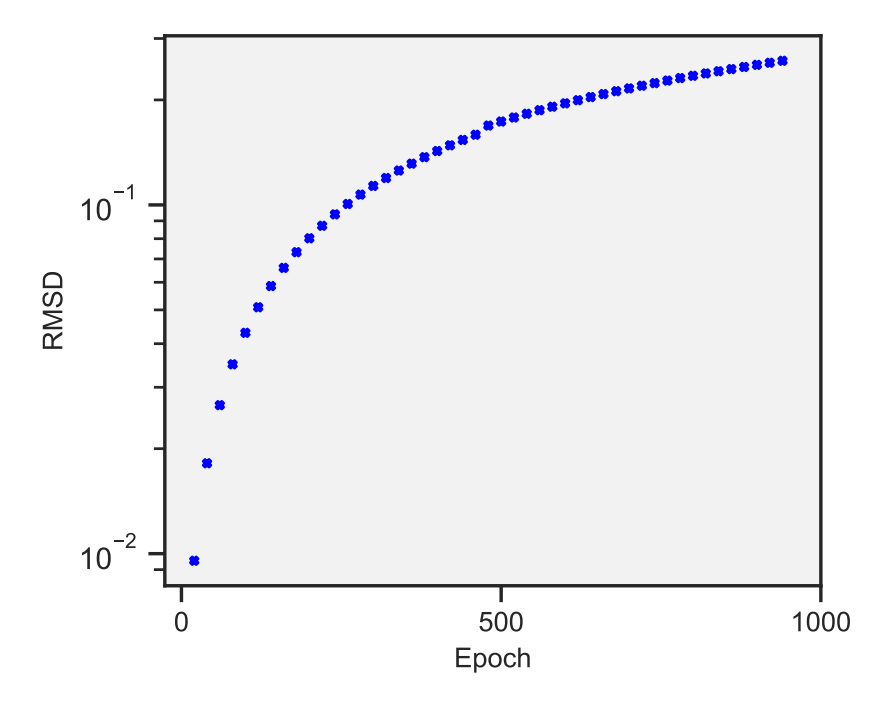


Figure 8.8: **Root mean square deviation (RMSD).** Root mean square deviation (RMSD) vs Epoch. The RMSD values were evaluated between the orientation estimates at two consecutive updates of the Local Optimizer. The update is performed every 20^{th} epoch of the training.

Fig. 8.9(d) and (e) show the latent space representation learned by the VAE, with data points colored by the ground truth roundness and size, respectively. The latent space effectively captures the relationships between these parameters.

The pseudocode for a single epoch is described in Appendix Section 1.

8.9 MD Simulation

We employed the Gromacs package [219] for our simulations, utilising the OPLS-AA force field [61] to investigate the A/B and C/C dimers in vacuum conditions. The initial configurations were based on the 2MS2 PDB structure [45]. To achieve a total charge of +10e for the dimers, we protonated specific aspartic and glutamic acid residues within each subunit [174], adhering to a well-established protocol [61]. Subsequently, the structures underwent a steepest descent energy minimisation followed by a brief equilibration at 300K, without the application of periodic boundary conditions or pressure coupling, to simulate vacuum conditions. Protein dynamics were monitored over a 20 ns period, with all parameters maintained in alignment with the established protocol [61].

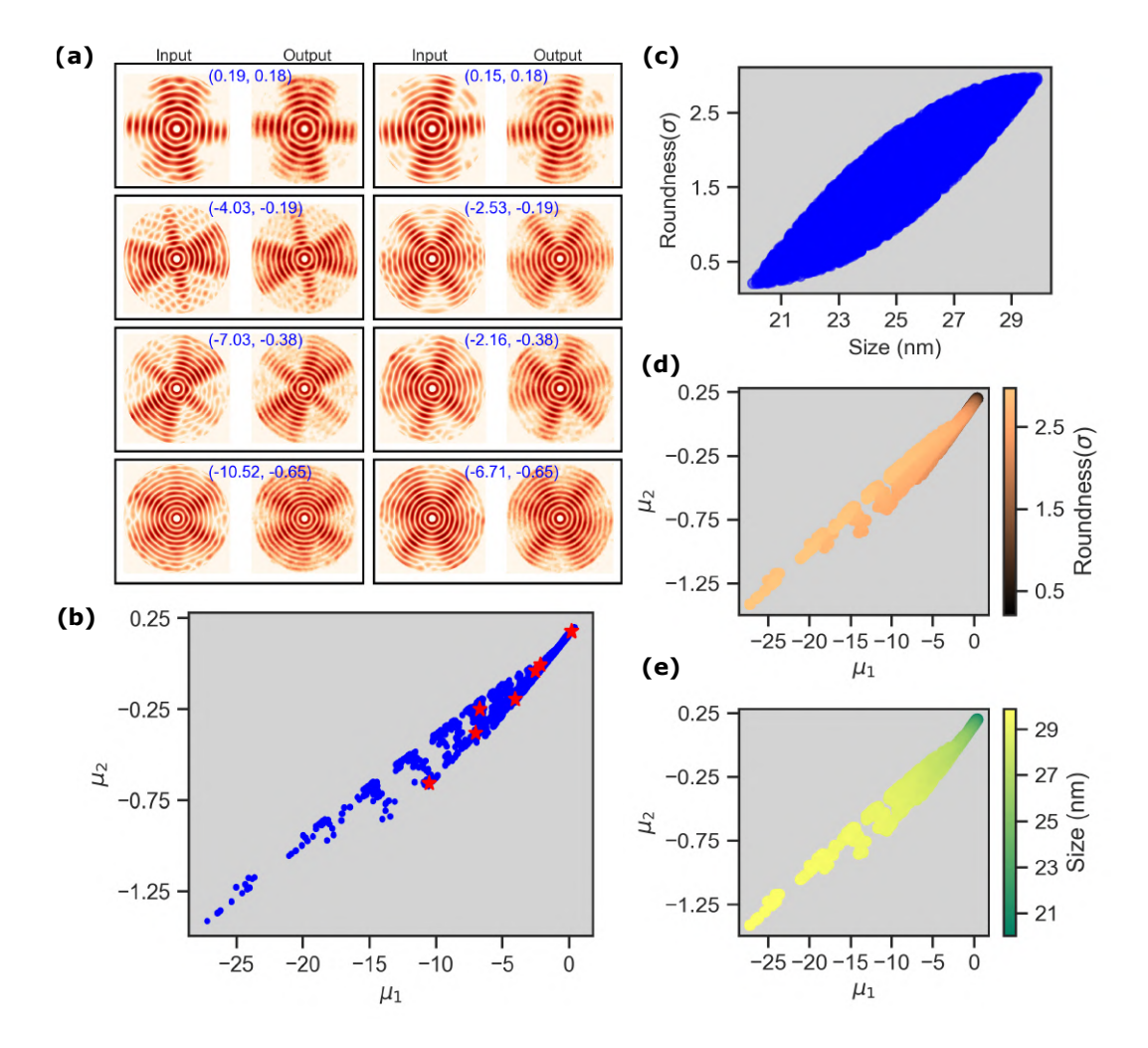


Figure 8.9: **Simulated Dataset.** (a) Comparison between the input 2D intensity data and the corresponding VAE reconstruction on the simulated dataset. (b) Latent space representation of the VAE; the red points indicate the data sample shown in (a), with coordinates provided in the inset. (c) Ground truth distribution of size and roundness parameters used to generate the simulated dataset of icosahedra particles. (d, e) Latent space representations of VAE color-coded by roundness and size, respectively.

Appendix

 \prec This chapter provides additional methodological details on developed code that expands upon the results presented in Chapters 3 and 5 of this dissertation. The content herein is intended to offer deeper technical insight and support reproducibility of the described work. \succ

9.1 Training VAE on Simulated Data

Algorithm 2 outlines the training procedure for VAE on simulated diffraction data that captures shape and size variations of an icosahedral object (see Supplementary Section 8). The training begins by loading 2D diffraction class averages and their corresponding orientations, represented as quaternions. During preprocessing, each intensity image is rescaled and normalized, producing input suitable for the VAE.

The VAE comprises an encoder that maps each input image and its orientation vector to a latent distribution in a low-dimensional space (Z), and a decoder that reconstructs a 3D volume from a sample drawn from this distribution. For each mini-batch, the reconstructed volume is symmetrized using Friedel symmetry, and the input data is subsequently reconstructed by slicing these volumes at known orientations.

The training loss \mathcal{L} is composed of two terms: The squared error term, denoted \mathcal{L}_{SE} , measures the difference between input and reconstructed images, while the Kullback–Leibler divergence, \mathcal{L}_{KL} , regularizes the latent distribution. A standard β -VAE with $\beta=1$ is used. This training process yields a generative model that

captures meaningful latent variations in the diffraction data. When applied to experimental datasets, algorithmic modifications were introduced, as described in Chapter 3.

```
Algorithm 2 Training VAE on Simulated Data
Require: Diffraction frames I, orientations \Omega
Ensure: Trained VAE
   function PreprocessData
       Load 2D intensities I and orientations \Omega
       Apply scaling and normalization
       return (I_{input}, \Omega)
   end function
   function VAE(latent dims)
       Define Encoder: (I_b, \Omega_b) \to \mu, \sigma
       Sample latent variable: z \sim \mathcal{N}(\mu, \sigma^2)
       Define Decoder: z \to \hat{V} (3D volume)
       return VAE model
   end function
   procedure TrainVAE
       (I_{\text{input}}, \Omega) \leftarrow \text{PreprocessData}
       Initialize VAE with latent space \mathbb{R}^{latent\_dims}
       Set optimizer (Adam) and computation device
       Define slicing planes from orientations \Omega
       for epoch = 1 to N_{\text{epochs}} do
           for all batches (I_b, \Omega_b) do
                z \leftarrow \mathbf{Encoder}(I_b, \Omega_b)
                \hat{V} \leftarrow \mathbf{Decoder}(z)
                Apply Friedel symmetry: \hat{V}_{	ext{sym}}
                Project to 2D: \hat{I}_b \leftarrow \text{Slice}(\hat{V}_{\text{sym}}, \Omega_b)
                Compute loss:
                                     \mathcal{L} = \|I_b - \hat{I}_b\|^2 + \mathcal{L}_{\text{KL}}
                Backpropagate and update weights
           end for
           if epoch mod 10 = 0 then
                Save model checkpoint and current outputs
           end if
       end for
       return Trained VAE
   end procedure
```

9.2 Grid Search Optimization

The pseudocode in Algorithms 3 through 6 describes an iterative optimization routine for reconstructing the Fourier transform of the target object from simulated diffraction data in scenario of lattice-enhanced holographic-SPI detailed in Chapter 5. The process begins by initializing a random complex object f_{obj} and a random set of in-plane orientations θ_i for each frame. These parameters along with translational shifts (**s**) and incident fluence (φ) are then refined over multiple iterations using a modular pipeline of independent optimization stages.

The optimization cycle comprises three main stages. First, the *Parameter Optimizer* (Algorithm 4) estimates translation shifts ${\bf s}$ and incident fluence φ by minimizing the error between the calculated and observed intensities across a coarse 3D grid, followed by local refinement (fine grid search). Second, the *Orientation Optimizer* (Algorithm 5) searches for the best in-plane rotation angle θ for each frame using a coarse-to-fine grid strategy that first explores a broad parameter range, then refines the search in a smaller, high-resolution grid. Finally, the *Object Optimizer* (Algorithm 6) reconstructs the object's Fourier transform f_{obj} by optimizing the real and imaginary components of each pixel, minimizing intensity mismatch across frames.

This iterative optimization framework, managed by the *Optimization Runner* (Algorithm 3), updates all parameters in a loop, gradually improving the estimates at each step. The grid-based approach, combined with hierarchical refinement, allows for robust convergence even under noisy input data, making the method well-suited for practical imaging scenarios.

Algorithm 3 Optimization Runner

```
procedure Initialize(config_file)
   Load Hyperparameters
   Initialize random fobj
   Initialize random angles \theta_i \sim \mathcal{U}(0, 2\pi)
end procedure
procedure RUN OPTIMIZATION(num_iter)
   for i=1 to num_iter do
        (s,\varphi) \leftarrow \text{Parameter Optimizer(fobj},\theta).\text{Optimize params()}
        \theta \leftarrow \text{Orientation Optimizer(fobj},s,\varphi).\text{Optimize orientation()}
        fobj \leftarrow \text{Object Optimizer}(s,\varphi,\theta).\text{Solve()}
        end for
        return Optimized parameters and fobj
end procedure
```

Algorithm 4 Parameter Optimizer

```
procedure Initialize(I_{obs}, f_{obj}, \theta)
    Define grid (h, k)
end procedure
function Grid Search((h, k), f_{\text{obj}}, I_{\text{obs}}, (\mathbf{s}, \varphi) ranges)
    Form grid of \mathbf{s}, \varphi
    Compute I<sub>calc</sub>, Error
    Return Optimal \mathbf{s}^*, \varphi^*, Error*
end function
function Analyze Frame(I_{obs}, (h, k), \theta)
    GRID SEARCH: Coarse grid
    while error change > \varepsilon do
         Fine search
         GRID SEARCH
    end while
    return Optimal \mathbf{s}, \varphi, Error
end function
function Optimize Params
    for each frame i do
         ANALYZE FRAME
    end for
    return \mathbf{s}_i, \varphi_i
end function
```

Algorithm 5 Orientation Optimizer

```
procedure Initialize(\varphi, \mathbf{s}, f_{\mathrm{obj}}, I_{\mathrm{obs}})

Define grid (h,k)

end procedure

function optimize orientation

for each frame i do

Coarse search over \theta \in [0,2\pi]

Fine search over \theta until \Delta \theta < 10^{-4}

end for

return Optimal \theta_i

end function
```

```
Algorithm 6 Object Optimizer
```

```
procedure Initialize(s, \varphi, \theta, I_{obs})
    Define grid (h, k)
    Define coarse search ranges for \Re(f_{\text{obj}}) and \Im(f_{\text{obj}})
end procedure
function Compute Error Grid(\Re, \Im, I_{obs})
    Form grid of f_{\text{guess}} = \Re + i \Im
    Compute \; I_{\rm calc}
    Return \sum (I_{\rm calc} - I_{\rm obs})^2
end function
function Solve
    for each (h, k) do
         Coarse search
         Fine search
    end for
    return Optimized f_{obj}
end function
```

Bibliography

- [1] A. M. Brown, "Development of visual sensitivity to light and color vision in human infants: A critical review," *Vision research*, vol. 30, no. 8, pp. 1159–1188, 1990.
- [2] C. A. Brownell, S. Zerwas, and G. B. Ramani, "so big": The development of body self-awareness in toddlers," *Child development*, vol. 78, no. 5, pp. 1426–1440, 2007.
- [3] J. A. Taylor and R. B. Ivry, "The role of strategies in motor learning," *Annals of the New York Academy of Sciences*, vol. 1251, no. 1, pp. 1–12, 2012.
- [4] N.-T. D. Loh and V. Elser, "Reconstruction algorithm for single-particle diffraction imaging experiments," *Physical Review E*, vol. 80, no. 2, p. 026705, 2009.
- [5] A. Punjani, J. L. Rubinstein, D. J. Fleet, and M. A. Brubaker, "cryosparc: algorithms for rapid unsupervised cryo-em structure determination," *Nature methods*, vol. 14, no. 3, pp. 290–296, 2017.
- [6] P. B. Rosenthal and R. Henderson, "Optimal determination of particle orientation, absolute hand, and contrast loss in single-particle electron cryomicroscopy," *Journal of molecular biology*, vol. 333, no. 4, pp. 721–745, 2003.
- [7] K. Ayyer, T.-Y. Lan, V. Elser, and N. D. Loh, "Dragonfly: an implementation of the expand–maximize–compress algorithm for single-particle imaging," *Journal of applied crystallography*, vol. 49, no. 4, pp. 1320–1335, 2016.
- [8] T. Ekeberg, M. Svenda, C. Abergel, F. R. N. C. Maia, V. Seltzer, J.-M. Claverie, M. Hantke, O. Jönsson, C. Nettelblad, G. van der Schot, et al., "Three-dimensional reconstruction of the giant mimivirus particle with an x-ray free-electron laser," Phys. Rev. Lett., vol. 114, p. 098102, Mar 2015.

- [9] A. Munke, J. Andreasson, A. Aquila, S. Awel, K. Ayyer, A. Barty, R. J. Bean, P. Berntsen, J. Bielecki, S. Boutet, *et al.*, "Coherent diffraction of single rice dwarf virus particles using hard x-rays at the linac coherent light source," *Scientific Data*, vol. 3, p. 160064, Aug 2016. Data Descriptor.
- [10] K. Ayyer, P. L. Xavier, J. Bielecki, Z. Shen, B. J. Daurer, A. K. Samanta, S. Awel, R. Bean, A. Barty, M. Bergemann, *et al.*, "3d diffractive imaging of nanoparticle ensembles using an x-ray laser," *Optica*, vol. 8, pp. 15–23, Jan 2021.
- [11] P. Emma, R. Akre, J. Arthur, R. Bionta, C. Bostedt, J. Bozek, A. Brachmann, P. Bucksbaum, R. Coffee, F.-J. Decker, *et al.*, "First lasing and operation of an ångstrom-wavelength free-electron laser," *nature photonics*, vol. 4, no. 9, pp. 641–647, 2010.
- [12] H. N. Chapman, P. Fromme, A. Barty, T. A. White, R. A. Kirian, A. Aquila, M. S. Hunter, J. Schulz, D. P. DePonte, U. Weierstall, *et al.*, "Femtosecond x-ray protein nanocrystallography," *Nature*, vol. 470, no. 7332, pp. 73–77, 2011.
- [13] H. N. Chapman, A. Barty, M. J. Bogan, S. Boutet, M. Frank, S. P. Hau-Riege, S. Marchesini, B. W. Woods, S. Bajt, W. H. Benner, *et al.*, "Femtosecond diffractive imaging with a soft-x-ray free-electron laser," *Nature Physics*, vol. 2, pp. 839–843, Dec 2006.
- [14] X.-C. Bai, G. McMullan, and S. H. Scheres, "How cryo-em is revolutionizing structural biology," *Trends in biochemical sciences*, vol. 40, no. 1, pp. 49–57, 2015.
- [15] E. H. Egelman, "The current revolution in cryo-em," *Biophysical journal*, vol. 110, no. 5, pp. 1008–1012, 2016.
- [16] J. A. Brito and M. Archer, "Structural biology techniques: X-ray crystallography, cryo-electron microscopy, and small-angle x-ray scattering," in *Practical approaches to biological inorganic chemistry*, pp. 375–416, Elsevier, 2020.
- [17] S. K. Burley, H. M. Berman, G. J. Kleywegt, J. L. Markley, H. Nakamura, and S. Velankar, "Protein data bank (pdb): the single global macromolecular structure archive," *Protein crystallography: methods and protocols*, pp. 627–641, 2017.
- [18] W. Kühlbrandt, "The resolution revolution," Science, vol. 343, no. 6178, pp. 1443–1444, 2014.

- [19] Q. Teng, *Structural biology: practical NMR applications*. Springer Science & Business Media, 2012.
- [20] H. Frauenfelder and B. McMahon, "Dynamics and function of proteins: the search for general concepts," *Proceedings of the National Academy of Sciences*, vol. 95, no. 9, pp. 4795–4797, 1998.
- [21] R. M. Daniel, R. V. Dunn, J. L. Finney, and J. C. Smith, "The role of dynamics in enzyme activity," *Annual review of biophysics and biomolecular structure*, vol. 32, no. 1, pp. 69–92, 2003.
- [22] J. L. Miller, "Cryoelectron microscopy pioneers win chemistry nobel," *Physics Today*, vol. 70, no. 12, pp. 22–24, 2017.
- [23] P. Tian, Femtosecond phase-coherent spectroscopy. Princeton University, 2003.
- [24] P. Portin, "The birth and development of the dna theory of inheritance: sixty years since the discovery of the structure of dna," *Journal of genetics*, vol. 93, pp. 293–302, 2014.
- [25] A. M. Davis, S. J. Teague, and G. J. Kleywegt, *Application and limitations of X-ray crystallographic data in structure-guided ligand and drug design.* The Royal Society of Chemistry, 2007.
- [26] A. Srivastava, T. Nagai, A. Srivastava, O. Miyashita, and F. Tama, "Role of computational methods in going beyond x-ray crystallography to explore protein structure and dynamics," *International journal of molecular sciences*, vol. 19, no. 11, p. 3401, 2018.
- [27] N. Chayen, T. Boggon, A. Cassetta, A. Deacon, T. Gleichmann, J. Habash, S. Harrop, J. Helliwell, Y. Nieh, M. Peterson, *et al.*, "Trends and challenges in experimental macromolecular crystallography," *Quarterly reviews of biophysics*, vol. 29, no. 3, pp. 227–278, 1996.
- [28] B.-G. Han, A. Avila-Sakar, J. Remis, and R. M. Glaeser, "Challenges in making ideal cryo-em samples," *Current Opinion in Structural Biology*, vol. 81, p. 102646, 2023.
- [29] M.-E. Mäeots and R. I. Enchev, "Structural dynamics: review of time-resolved cryo-em," *Biological Crystallography*, vol. 78, no. 8, pp. 927–935, 2022.

- [30] R. Neutze, R. Wouts, D. van der Spoel, E. Weckert, and J. Hajdu, "Potential for biomolecular imaging with femtosecond x-ray pulses," *Nature*, vol. 406, no. 6797, pp. 752–757, 2000.
- [31] I. Poudyal, M. Schmidt, and P. Schwander, "Single-particle imaging by x-ray free-electron lasers—how many snapshots are needed?," *Structural Dynamics*, vol. 7, no. 2, p. 024102, 2020.
- [32] A. Bellisario, F. R. Maia, and T. Ekeberg, "Noise reduction and mask removal neural network for x-ray single-particle imaging," *Applied Crystallography*, vol. 55, no. 1, pp. 122–132, 2022.
- [33] Z. Sun, J. Fan, H. Li, and H. Jiang, "Current status of single particle imaging with x-ray lasers," *Applied Sciences*, vol. 8, no. 1, p. 132, 2018.
- [34] X. Ou, X. Chen, X. Xu, L. Xie, X. Chen, Z. Hong, H. Bai, X. Liu, Q. Chen, L. Li, *et al.*, "Recent development in x-ray imaging technology: Future and challenges," *Research*, 2021.
- [35] K. Ayyer, "Reference-enhanced x-ray single-particle imaging," *Optica*, vol. 7, no. 6, pp. 593–601, 2020.
- [36] A. Mall and K. Ayyer, "Holographic single-particle imaging for weakly scattering, heterogeneous nanoscale objects," *Physical Review Applied*, vol. 19, no. 5, p. 054027, 2023.
- [37] B. Alberts, A. Johnson, J. Lewis, M. Raff, K. Roberts, and P. Walter, "Molecular motors," in *Molecular Biology of the Cell. 4th edition*, Garland Science, 2002.
- [38] C. I. Branden and J. Tooze, *Introduction to protein structure*. Garland Science, 2012.
- [39] D. S. Goodsell, *The machinery of life*. Springer, 2009.
- [40] H. Flechsig and A. S. Mikhailov, "Simple mechanics of protein machines," *Journal of the Royal Society Interface*, vol. 16, no. 155, p. 20190244, 2019.
- [41] J. D. Perlmutter and M. F. Hagan, "Mechanisms of virus assembly," *Annual review of physical chemistry*, vol. 66, no. 1, pp. 217–239, 2015.
- [42] D. L. Caspar and A. Klug, "Physical principles in the construction of regular viruses," in *Cold Spring Harbor symposia on quantitative biology*, vol. 27, pp. 1–24, Cold Spring Harbor Laboratory Press, 1962.

- [43] M. Sevvana, T. Klose, and M. G. Rossmann, "Principles of virus structure," *Encyclopedia of virology*, p. 257, 2021.
- [44] K. Valegård, L. Liljas, K. Fridborg, and T. Unge, "The three-dimensional structure of the bacterial virus ms2," *Nature*, vol. 345, no. 6270, pp. 36–41, 1990.
- [45] R. Golmohammadi, K. Valegård, K. Fridborg, and L. Liljas, "The refined structure of bacteriophage ms2 at 2·8 å resolution," *Journal of molecular biology*, vol. 234, no. 3, pp. 620–639, 1993.
- [46] Ó. Rolfsson, S. Middleton, I. W. Manfield, S. J. White, B. Fan, R. Vaughan, N. A. Ranson, E. Dykeman, R. Twarock, J. Ford, et al., "Direct evidence for packaging signal-mediated assembly of bacteriophage ms2," Journal of molecular biology, vol. 428, no. 2, pp. 431–448, 2016.
- [47] P. G. Stockley, S. J. White, E. Dykeman, I. Manfield, O. Rolfsson, N. Patel, R. Bingham, A. Barker, E. Wroblewski, R. Chandler-Bostock, *et al.*, "Bacteriophage ms2 genomic rna encodes an assembly instruction manual for its capsid," *Bacteriophage*, vol. 6, no. 1, p. e1157666, 2016.
- [48] A. Zlotnick, "To build a virus capsid: an equilibrium model of the self assembly of polyhedral protein complexes," *Journal of molecular biology*, vol. 241, no. 1, pp. 59–67, 1994.
- [49] N. Ban, P. Nissen, J. Hansen, P. B. Moore, and T. A. Steitz, "The complete atomic structure of the large ribosomal subunit at 2.4 å resolution," *Science*, vol. 289, no. 5481, pp. 905–920, 2000.
- [50] V. Ramakrishnan, "The ribosome emerges from a black box," *Cell*, vol. 159, no. 5, pp. 979–984, 2014.
- [51] H. F. Noller, "Rna structure: reading the ribosome," *Science*, vol. 309, no. 5740, pp. 1508–1514, 2005.
- [52] T. A. Steitz, "A structural understanding of the dynamic ribosome machine," *Nature reviews Molecular cell biology*, vol. 9, no. 3, pp. 242–253, 2008.
- [53] S. Sun, V. B. Rao, and M. G. Rossmann, "Genome packaging in viruses," *Current Opinion in Structural Biology*, vol. 20, no. 1, pp. 114–120, 2010.

- [54] M. G. Mateu, "Assembly, stability and dynamics of virus capsids," *Archives of biochemistry and biophysics*, vol. 531, no. 1-2, pp. 65–79, 2013.
- [55] H. Frauenfelder, S. G. Sligar, and P. G. Wolynes, "The energy landscapes and motions of proteins," *Science*, vol. 254, no. 5038, pp. 1598–1603, 1991.
- [56] K. Dill and S. Bromberg, *Molecular driving forces: statistical thermodynamics in biology, chemistry, physics, and nanoscience.* Garland Science, 2010.
- [57] K. Henzler-Wildman and D. Kern, "Dynamic personalities of proteins," *Nature*, vol. 450, no. 7172, pp. 964–972, 2007.
- [58] D. D. Boehr, R. Nussinov, and P. E. Wright, "The role of dynamic conformational ensembles in biomolecular recognition," *Nature chemical biology*, vol. 5, no. 11, pp. 789–796, 2009.
- [59] V. Ovchinnikov, M. Karplus, and E. Vanden-Eijnden, "Free energy of conformational transition paths in biomolecules: The string method and its application to myosin vi," *The Journal of chemical physics*, vol. 134, no. 8, 2011.
- [60] A. K. Jana and E. R. May, "Structural and dynamic asymmetry in icosahedrally symmetric virus capsids," *Current opinion in virology*, vol. 45, pp. 8–16, 2020.
- [61] M. N. Brodmerkel, E. De Santis, C. Uetrecht, C. Caleman, and E. G. Marklund, "Stability and conformational memory of electrosprayed and rehydrated bacteriophage ms2 virus coat proteins," *Current Research in Structural Biology*, vol. 4, pp. 338–348, 2022.
- [62] K. Toropova, G. Basnak, R. Twarock, P. G. Stockley, and N. A. Ranson, "The three-dimensional structure of genomic rna in bacteriophage ms2: implications for assembly," *Journal of molecular biology*, vol. 375, no. 3, pp. 824–836, 2008.
- [63] M. J. Roossinck, "Lifestyles of plant viruses," Philosophical Transactions of the Royal Society B: Biological Sciences, vol. 365, no. 1548, pp. 1899–1905, 2010.
- [64] A. Korostelev, S. Trakhanov, M. Laurberg, and H. F. Noller, "Crystal structure of a 70s ribosome-trna complex reveals functional interactions and rearrangements," *Cell*, vol. 126, no. 6, pp. 1065–1077, 2006.

- [65] M. Valle, A. Zavialov, J. Sengupta, U. Rawat, M. Ehrenberg, and J. Frank, "Locking and unlocking of ribosomal motions," *Cell*, vol. 114, no. 1, pp. 123–134, 2003.
- [66] R. Nussinov and C.-J. Tsai, "Allostery in disease and in drug discovery," *Cell*, vol. 153, no. 2, pp. 293–305, 2013.
- [67] J. S. Fraser, H. Van Den Bedem, A. J. Samelson, P. T. Lang, J. M. Holton, N. Echols, and T. Alber, "Accessing protein conformational ensembles using room-temperature x-ray crystallography," *Proceedings of the National Academy of Sciences*, vol. 108, no. 39, pp. 16247–16252, 2011.
- [68] M. Karplus and J. A. McCammon, "Molecular dynamics simulations of biomolecules," *Nature structural biology*, vol. 9, no. 9, pp. 646–652, 2002.
- [69] R. O. Dror, R. M. Dirks, J. Grossman, H. Xu, and D. E. Shaw, "Biomolecular simulation: a computational microscope for molecular biology," *Annual review of biophysics*, vol. 41, no. 1, pp. 429–452, 2012.
- [70] R. Mould, "Röntgen and the discovery of x-rays," *The British journal of radiology*, vol. 68, no. 815, pp. 1145–1176, 1995.
- [71] M. von Laue, "Concerning the detection of x-ray interferences," *Nobel lecture*, vol. 13, 1915.
- [72] W. H. Bragg and W. L. Bragg, "The reflection of x-rays by crystals," *Proceedings of the Royal Society of London. Series A, Containing Papers of a Mathematical and Physical Character*, vol. 88, no. 605, pp. 428–438, 1913.
- [73] R. Machlett, "An improved x-ray tube for diffraction analysis," *Journal of Applied Physics*, vol. 13, no. 6, pp. 398–401, 1942.
- [74] H. Winick, *Synchrotron radiation sources: a primer*, vol. 1. World Scientific, 1994.
- [75] C. Pellegrini, A. Marinelli, and S. Reiche, "The physics of x-ray free-electron lasers," *Reviews of Modern Physics*, vol. 88, no. 1, p. 015006, 2016.
- [76] J. Spence, "Xfels for structure and dynamics in biology," *IUCrJ*, vol. 4, no. 4, pp. 322–339, 2017.
- [77] D. Attwood, *Soft x-rays and extreme ultraviolet radiation: principles and applications.* Cambridge university press, 2000.

- [78] J. Hajdu, "Single-molecule x-ray diffraction," *Current opinion in structural biology*, vol. 10, no. 5, pp. 569–573, 2000.
- [79] H. Mimura, H. Yumoto, S. Matsuyama, Y. Sano, K. Yamamura, Y. Mori, M. Yabashi, Y. Nishino, K. Tamasaku, T. Ishikawa, *et al.*, "Efficient focusing of hard x rays to 25nm by a total reflection mirror," *Applied Physics Letters*, vol. 90, no. 5, 2007.
- [80] Z. Huang and K.-J. Kim, "Review of x-ray free-electron laser theory," *Physical Review Special Topics—Accelerators and Beams*, vol. 10, no. 3, p. 034801, 2007.
- [81] M. Papka, P. Messina, R. Coffey, and C. Drugan, "Argonne leadership computing facility 2011 annual report: Shaping future supercomputing.," tech. rep., Argonne National Lab.(ANL), Argonne, IL (United States), 2012.
- [82] J. Biasci, J. Bouteille, N. Carmignani, J. Chavanne, D. Coulon, Y. Dabin, F. Ewald, L. Farvacque, L. Goirand, M. Hahn, *et al.*, "A low-emittance lattice for the esrf," *Synchrotron Radiation News*, vol. 27, no. 6, pp. 8–12, 2014.
- [83] H. Kamitsubo, "Spring-8 program," *Synchrotron Radiation*, vol. 5, no. 3, pp. 162–167, 1998.
- [84] K. Balewski, M. Bieler, J. Keil, A. Kling, G. Sahoo, and R. Wanzenberg, "Petra iii upgrade," in *Proceedings of 2nd International Particle Accelerator Conference (IPAC11)*, San Sebastian, Spain, pp. 4–9, 2011.
- [85] D. Svergun, E. Shtykova, V. Volkov, and L. Feigin, "Small-angle x-ray scattering, synchrotron radiation, and the structure of bio-and nanosystems," *Crystallography Reports*, vol. 56, pp. 725–750, 2011.
- [86] E. Nogales and S. H. Scheres, "Cryo-em: a unique tool for the visualization of macromolecular complexity," *Molecular cell*, vol. 58, no. 4, pp. 677–689, 2015.
- [87] B. W. J. McNeil and N. R. Thompson, "X-ray free-electron lasers," *Nature Photonics*, vol. 4, no. 12, pp. 814–821, 2010.
- [88] C. Pellegrini, "The history of x-ray free-electron lasers," *The European Physical Journal H*, vol. 37, no. 5, pp. 659–708, 2012.
- [89] R. Bonifacio and L. D. S. Souza, "Tuning and slippage optimization in a high-gain fel with a waveguide," *Nuclear Instruments and Methods in Physics Research Section A: Accelerators, Spectrometers, Detectors and Associated Equipment*, vol. 276, no. 1-2, pp. 394–398, 1989.

- [90] A. Barty, C. Caleman, A. Aquila, N. Timneanu, L. Lomb, T. A. White, J. Andreasson, D. Arnlund, S. Bajt, T. R. Barends, *et al.*, "Self-terminating diffraction gates femtosecond x-ray nanocrystallography measurements," *Nature photonics*, vol. 6, no. 1, pp. 35–40, 2012.
- [91] I. Schlichting, "Serial femtosecond crystallography: the first five years," *IUCrJ*, vol. 2, pp. 246–255, Mar 2015.
- [92] A. Aquila, A. Barty, C. Bostedt, S. Boutet, G. Carini, D. DePonte, P. Drell, S. Doniach, K. Downing, T. Earnest, *et al.*, "The linac coherent light source single particle imaging road map," *Structural Dynamics*, vol. 2, no. 4, p. 041701, 2015.
- [93] C. Bostedt, S. Boutet, D. M. Fritz, Z. Huang, H. J. Lee, H. T. Lemke, A. Robert, W. F. Schlotter, J. J. Turner, and G. J. Williams, "Linac coherent light source: The first five years," *Rev. Mod. Phys.*, vol. 88, p. 015007, Mar 2016.
- [94] J. N. Galayda *et al.*, "The lcls-ii: A high power upgrade to the lcls," *9th IPAC*, p. 18, 2018.
- [95] H. Weise, W. Decking, *et al.*, "Commissioning and first lasing of the european xfel," *Proc. FEL* '17, pp. 9–13, 2017.
- [96] Y. Shi, "A glimpse of structural biology through x-ray crystallography," *Cell*, vol. 159, no. 5, pp. 995–1014, 2014.
- [97] A. Banari, A. K. Samanta, A. Munke, T. Laugks, S. Bajt, K. Grünewald, T. C. Marlovits, J. Küpper, F. R. Maia, H. N. Chapman, *et al.*, "Advancing timeresolved structural biology: latest strategies in cryo-em and x-ray crystallography," *Nature Methods*, pp. 1–16, 2025.
- [98] J. Drenth, *Principles of protein X-ray crystallography*. Springer Science & Business Media, 2007.
- [99] S. E. Ealick, "Advances in multiple wavelength anomalous diffraction crystallography," *Current opinion in chemical biology*, vol. 4, no. 5, pp. 495–499, 2000.
- [100] A. Wlodawer, W. Minor, Z. Dauter, and M. Jaskolski, "Protein crystallography for non-crystallographers, or how to get the best (but not more) from published macromolecular structures," *The FEBS journal*, vol. 275, no. 1, pp. 1–21, 2008.

- [101] P. Nogly, T. Weinert, D. James, S. Carbajo, D. Ozerov, A. Furrer, D. Gashi, V. Borin, P. Skopintsev, K. Jaeger, *et al.*, "Retinal isomerization in bacteri-orhodopsin captured by a femtosecond x-ray laser," *Science*, vol. 361, no. 6398, p. eaat0094, 2018.
- [102] Y. Shi, K. Yin, X. Tai, H. DeMirci, A. Hosseinizadeh, B. G. Hogue, H. Li, A. Ourmazd, P. Schwander, I. A. Vartanyants, C. H. Yoon, A. Aquila, and H. Liu, "Evaluation of the performance of classification algorithms for XFEL single-particle imaging data," *IUCr*7, vol. 6, pp. 331–340, Mar 2019.
- [103] E. Nogales, "The development of cryo-em into a mainstream structural biology technique," *Nature Methods*, vol. 13, no. 1, pp. 24–27, 2016.
- [104] Y. Cheng, "Single-particle cryo-em at crystallographic resolution," *Cell*, vol. 161, no. 3, pp. 450–457, 2015.
- [105] M. Chen, J. M. Bell, X. Shi, S. Y. Sun, Z. Wang, and S. J. Ludtke, "A complete data processing workflow for cryo-et and subtomogram averaging," *Nature methods*, vol. 16, no. 11, pp. 1161–1168, 2019.
- [106] B. L. Nannenga and T. Gonen, "Microed opens a new era for biological structure determination," *Current opinion in structural biology*, vol. 40, pp. 128–135, 2016.
- [107] J. Frank, "Advances in the field of single-particle cryo-electron microscopy over the last decade," *Nature protocols*, vol. 12, no. 2, pp. 209–212, 2017.
- [108] J. A. Mindell and N. Grigorieff, "Accurate determination of local defocus and specimen tilt in electron microscopy," *Journal of structural biology*, vol. 142, no. 3, pp. 334–347, 2003.
- [109] C. J. Russo and L. A. Passmore, "Ultrastable gold substrates for electron cryomicroscopy," *Science*, vol. 346, no. 6215, pp. 1377–1380, 2014.
- [110] S. H. Scheres, "Relion: Implementation of a bayesian approach to cryo-em structure determination," *Journal of Structural Biology*, vol. 180, no. 3, pp. 519–530, 2012.
- [111] G. Tang, L. Peng, P. R. Baldwin, D. S. Mann, W. Jiang, I. Rees, and S. J. Ludtke, "Eman2: an extensible image processing suite for electron microscopy," *Journal of structural biology*, vol. 157, no. 1, pp. 38–46, 2007.

- [112] K. J. Gaffney and H. N. Chapman, "Imaging atomic structure and dynamics with ultrafast x-ray scattering," *Science*, vol. 316, no. 5830, pp. 1444–1448, 2007.
- [113] M. M. Seibert, T. Ekeberg, F. R. Maia, M. Svenda, J. Andreasson, O. Jönsson, D. Odić, B. Iwan, A. Rocker, D. Westphal, *et al.*, "Single mimivirus particles intercepted and imaged with an x-ray laser," *Nature*, vol. 470, no. 7332, pp. 78–81, 2011.
- [114] J. R. Fienup, "Phase retrieval algorithms: a comparison," *Applied optics*, vol. 21, no. 15, pp. 2758–2769, 1982.
- [115] V. Elser, "Phase retrieval by iterated projections," $\mathcal{J}OSA$ A, vol. 20, no. 1, pp. 40–55, 2003.
- [116] K. A. Nugent, "Coherent methods in the x-ray sciences," *Advances in Physics*, vol. 59, no. 1, pp. 1–99, 2010.
- [117] M. Sutton, "A review of x-ray intensity fluctuation spectroscopy," *Comptes Rendus Physique*, vol. 9, no. 5, pp. 657–667, 2008. Synchrotron x-rays and condensed matter.
- [118] E. F. Garman, "Radiation damage in macromolecular crystallography: what is it and why should we care?," *Biological Crystallography*, vol. 66, no. 4, pp. 339–351, 2010.
- [119] J. M. Holton, "A beginner's guide to radiation damage," *Synchrotron Radiation*, vol. 16, no. 2, pp. 133–142, 2009.
- [120] M. Suga, F. Akita, K. Hirata, G. Ueno, H. Murakami, Y. Nakajima, T. Shimizu, K. Yamashita, M. Yamamoto, H. Ago, *et al.*, "Native structure of photosystem ii at 1.95 å resolution viewed by femtosecond x-ray pulses," *Nature*, vol. 517, no. 7532, pp. 99–103, 2015.
- [121] I. McNulty, J. Kirz, C. Jacobsen, E. H. Anderson, M. R. Howells, and D. P. Kern, "High-resolution imaging by fourier transform x-ray holography," *Science*, vol. 256, no. 5059, pp. 1009–1012, 1992.
- [122] S. Eisebitt, J. Lüning, W. Schlotter, M. Lörgen, O. Hellwig, W. Eberhardt, and J. Stöhr, "Lensless imaging of magnetic nanostructures by x-ray spectroholography," *Nature*, vol. 432, no. 7019, pp. 885–888, 2004.

- [123] T. Gorkhover, A. Ulmer, K. Ferguson, M. Bucher, F. R. Maia, J. Bielecki, T. Ekeberg, M. F. Hantke, B. J. Daurer, C. Nettelblad, *et al.*, "Femtosecond x-ray fourier holography imaging of free-flying nanoparticles," *Nature Photonics*, vol. 12, no. 3, pp. 150–153, 2018.
- [124] P. Thibault, M. Dierolf, A. Menzel, O. Bunk, C. David, and F. Pfeiffer, "High-resolution scanning x-ray diffraction microscopy," *Science*, vol. 321, no. 5887, pp. 379–382, 2008.
- [125] J. M. Rodenburg and H. M. Faulkner, "A phase retrieval algorithm for shifting illumination," *Applied physics letters*, vol. 85, no. 20, pp. 4795–4797, 2004.
- [126] A. M. Maiden and J. M. Rodenburg, "An improved ptychographical phase retrieval algorithm for diffractive imaging," *Ultramicroscopy*, vol. 109, no. 10, pp. 1256–1262, 2009.
- [127] P. Thibault and M. Guizar-Sicairos, "Maximum-likelihood refinement for coherent diffractive imaging," *New Journal of Physics*, vol. 14, no. 6, p. 063004, 2012.
- [128] K. Giewekemeyer, P. Thibault, S. Kalbfleisch, A. Beerlink, C. M. Kewish, M. Dierolf, F. Pfeiffer, and T. Salditt, "Quantitative biological imaging by ptychographic x-ray diffraction microscopy," *Proceedings of the National Academy of Sciences*, vol. 107, no. 2, pp. 529–534, 2010.
- [129] F. Pfeiffer, "X-ray ptychography," *Nature Photonics*, vol. 12, no. 1, pp. 9–17, 2018.
- [130] S. Marchesini, S. Boutet, A. E. Sakdinawat, M. J. Bogan, S. Bajt, A. Barty, H. N. Chapman, M. Frank, S. P. Hau-Riege, A. Szöke, *et al.*, "Massively parallel x-ray holography," *Nature photonics*, vol. 2, no. 9, pp. 560–563, 2008.
- [131] M. Van Heel and M. Schatz, "Fourier shell correlation threshold criteria," *Journal of structural biology*, vol. 151, no. 3, pp. 250–262, 2005.
- [132] A. Mall, A. Munke, Z. Shen, P. Mazumder, J. Bielecki, A. Estillore, C. Kim, R. Letrun, J. Lübke, S. Rafie-Zinedine, *et al.*, "Observation of aerosolization-induced morphological changes in viral capsids," *arXiv preprint arXiv:2407.11687*, 2024.
- [133] K. Ayyer, A. J. Morgan, A. Aquila, H. DeMirci, B. G. Hogue, R. A. Kirian, P. L. Xavier, C. H. Yoon, H. N. Chapman, and A. Barty, "Low-signal limit

- of x-ray single particle diffractive imaging," *Optics Express*, vol. 27, no. 26, pp. 37816–37833, 2019.
- [134] Z. Shen, P. L. Xavier, R. Bean, J. Bielecki, M. Bergemann, B. J. Daurer, T. Ekeberg, A. D. Estillore, H. Fangohr, K. Giewekemeyer, *et al.*, "Resolving nonequilibrium shape variations among millions of gold nanoparticles," *ACS Nano*, vol. 18, no. 24, pp. 15576–15589, 2024.
- [135] Z. Shen, M. Samoli, O. Erdem, J. Bielecki, A. K. Samanta, A. Estillore, C. Kim, Y. Kim, J. Koliyadu, R. Letrun, *et al.*, "Direct observation of the exciton polaron by serial femtosecond crystallography on single cspbbr _3 quantum dots," *arXiv preprint arXiv:2502.02343*, 2025.
- [136] Y. Zhuang, S. Awel, A. Barty, R. Bean, J. Bielecki, M. Bergemann, B. J. Daurer, T. Ekeberg, A. D. Estillore, H. Fangohr, *et al.*, "Unsupervised learning approaches to characterizing heterogeneous samples using x-ray single-particle imaging," *IUCrJ*, vol. 9, no. 2, pp. 204–214, 2022.
- [137] D. Assalauova, A. Ignatenko, F. Isensee, D. Trofimova, and I. A. Vartanyants, "Classification of diffraction patterns using a convolutional neural network in single-particle-imaging experiments performed at x-ray free-electron lasers," *Applied Crystallography*, vol. 55, no. 3, pp. 444–454, 2022.
- [138] J. Zimmermann, B. Langbehn, R. Cucini, M. Di Fraia, P. Finetti, A. C. LaForge, T. Nishiyama, Y. Ovcharenko, P. Piseri, O. Plekan, *et al.*, "Deep neural networks for classifying complex features in diffraction images," *Physical Review E*, vol. 99, no. 6, p. 063309, 2019.
- [139] J. Zimmermann, F. Beguet, D. Guthruf, B. Langbehn, and D. Rupp, "Finding the semantic similarity in single-particle diffraction images using self-supervised contrastive projection learning," *npj Computational Materials*, vol. 9, no. 1, p. 24, 2023.
- [140] S. Zhou, *Data Heterogeneity in Single Particle Imaging Experiment with X-Ray Free Electron Laser.* PhD thesis, National University of Singapore (Singapore), 2020.
- [141] L. Wu, S. Yoo, A. F. Suzana, T. A. Assefa, J. Diao, R. J. Harder, W. Cha, and I. K. Robinson, "Three-dimensional coherent x-ray diffraction imaging via deep convolutional neural networks," *npj Computational Materials*, vol. 7, no. 1, p. 175, 2021.

- [142] D. P. Kingma and M. Welling, "Auto-encoding variational bayes," *arXiv* preprint arXiv 1312.6114, 2013.
- [143] J. Shenoy, A. Levy, F. Poitevin, and G. Wetzstein, "Amortized pose estimation for x-ray single particle imaging," in *Machine learning for structural biology Workshop*, NeurIPS 2023, 2023.
- [144] J. Shenoy, A. Levy, F. Poitevin, and G. Wetzstein, "Scalable 3d reconstruction from single particle x-ray diffraction images based on online machine learning," *arXiv preprint arXiv:2312.14432*, 2023.
- [145] N. de Martín Garrido, M. A. Crone, K. Ramlaul, P. A. Simpson, P. S. Freemont, and C. H. Aylett, "Bacteriophage ms2 displays unreported capsid variability assembling t= 4 and mixed capsids," *Molecular Microbiology*, vol. 113, no. 1, pp. 143–152, 2020.
- [146] P. Plevka, K. Tars, and L. Liljas, "Crystal packing of a bacteriophage ms2 coat protein mutant corresponds to octahedral particles," *Protein Science*, vol. 17, no. 10, pp. 1731–1739, 2008.
- [147] M. Widom, J. Lidmar, and D. R. Nelson, "Soft modes near the buckling transition of icosahedral shells," *Physical Review E*, vol. 76, no. 3, p. 031911, 2007.
- [148] T. T. Nguyen, R. F. Bruinsma, and W. M. Gelbart, "Elasticity theory and shape transitions of viral shells," *Physical Review E*, vol. 72, no. 5, p. 051923, 2005.
- [149] M. Buenemann and P. Lenz, "Elastic properties and mechanical stability of chiral and filled viral capsids," *Physical Review E*, vol. 78, no. 5, p. 051924, 2008.
- [150] A. Ignatenko, D. Assalauova, S. A. Bobkov, L. Gelisio, A. B. Teslyuk, V. A. Ilyin, and I. A. Vartanyants, "Classification of diffraction patterns in single particle imaging experiments performed at x-ray free-electron lasers using a convolutional neural network," *Machine Learning: Science and Technology*, vol. 2, no. 2, p. 025014, 2021.
- [151] M. Rose, S. Bobkov, K. Ayyer, R. P. Kurta, D. Dzhigaev, Y. Y. Kim, A. J. Morgan, C. H. Yoon, D. Westphal, J. Bielecki, *et al.*, "Single-particle imaging without symmetry constraints at an x-ray free-electron laser," *IUCrJ*, vol. 5, no. 6, pp. 727–736, 2018.

- [152] D. H. Cho, Z. Shen, Y. Ihm, D. H. Wi, C. Jung, D. Nam, S. Kim, S.-Y. Park, K. S. Kim, D. Sung, *et al.*, "High-throughput 3d ensemble characterization of individual core–shell nanoparticles with x-ray free electron laser single-particle imaging," *ACS nano*, vol. 15, no. 3, pp. 4066–4076, 2021.
- [153] D. Hoeing, R. Salzwedel, L. Worbs, Y. Zhuang, A. K. Samanta, J. Lübke, A. D. Estillore, K. Dlugolecki, C. Passow, B. Erk, *et al.*, "Time-resolved single-particle x-ray scattering reveals electron-density gradients as coherent plasmonic-nanoparticle-oscillation source," *Nano Letters*, vol. 23, no. 13, pp. 5943–5950, 2023.
- [154] A. Colombo, S. Dold, P. Kolb, N. Bernhardt, P. Behrens, J. Correa, S. Düsterer, B. Erk, L. Hecht, A. Heilrath, *et al.*, "Three-dimensional femtosecond snapshots of isolated faceted nanostructures," *Science Advances*, vol. 9, no. 8, p. eade5839, 2023.
- [155] S. Dold, T. Reichenbach, A. Colombo, J. Jordan, I. Barke, P. Behrens, N. Bernhardt, J. Correa, S. Düsterer, B. Erk, *et al.*, "Melting, bubble-like expansion and explosion of superheated plasmonic nanoparticles," *arXiv preprint arXiv:2309.00433*, 2023.
- [156] T. Ekeberg, D. Assalauova, J. Bielecki, R. Boll, B. J. Daurer, L. A. Eichacker, L. E. Franken, D. E. Galli, L. Gelisio, L. Gumprecht, *et al.*, "Observation of a single protein by ultrafast x-ray diffraction," *Light: Science & Applications*, vol. 13, no. 1, p. 15, 2024.
- [157] J. J. Thomas, B. Bothner, J. Traina, W. H. Benner, and G. Siuzdak, "Electrospray ion mobility spectrometry of intact viruses," *Spectroscopy*, vol. 18, no. 1, pp. 31–36, 2004.
- [158] N. Martín-González, S. M. G. Darvas, A. Durana, G. A. Marti, D. M. Guérin, and P. J. De Pablo, "Exploring the role of genome and structural ions in preventing viral capsid collapse during dehydration," *Journal of Physics: Condensed Matter*, vol. 30, no. 10, p. 104001, 2018.
- [159] H. Coleman, J. S. Perez, D. K. Schwartz, J. Kaar, R. L. Garcea, and T. W. Randolph, "Effect of mechanical stresses on viral capsid disruption during droplet formation and drying," *Colloids and Surfaces B: Biointerfaces*, vol. 233, p. 113661, 2024.

- [160] M. A. Lauffer and I. J. Bendet, "The hydration of viruses," in *Advances in virus* research, vol. 2, pp. 241–287, Elsevier, 1954.
- [161] V. E. COSSLETT and R. MARKHAM, "Structure of turnip yellow mosaic virus crystals in the electron microscope," *Nature*, vol. 161, pp. 250–252, Feb 1948.
- [162] J. Bernal and C. Carlisle, "Unit cell measurements of wet and dry crystalline turnip yellow mosaic virus," *Nature*, vol. 162, no. 4108, pp. 139–140, 1948.
- [163] Y. G. Kuznetsov, A. Malkin, R. Lucas, M. Plomp, and A. McPherson, "Imaging of viruses by atomic force microscopy," *Journal of General Virology*, vol. 82, no. 9, pp. 2025–2034, 2001.
- [164] Y. G. Kuznetsov and A. McPherson, "Atomic force microscopy in imaging of viruses and virus-infected cells," *Microbiology and molecular biology reviews*, vol. 75, no. 2, pp. 268–285, 2011.
- [165] A. P. Mancuso, A. Aquila, L. Batchelor, R. J. Bean, J. Bielecki, G. Borchers, K. Doerner, K. Giewekemeyer, R. Graceffa, O. D. Kelsey, *et al.*, "The single particles, clusters and biomolecules and serial femtosecond crystallography instrument of the european xfel: Initial installation," *Journal of synchrotron radiation*, vol. 26, no. 3, pp. 660–676, 2019.
- [166] B. Henrich, J. Becker, R. Dinapoli, P. Goettlicher, H. Graafsma, H. Hirsemann, R. Klanner, H. Krueger, R. Mazzocco, A. Mozzanica, et al., "The adaptive gain integrating pixel detector agipd a detector for the european xfel," Nuclear Instruments and Methods in Physics Research Section A: Accelerators, Spectrometers, Detectors and Associated Equipment, vol. 633, pp. S11–S14, 2011.
- [167] J. Bielecki, M. F. Hantke, B. J. Daurer, H. K. N. Reddy, D. Hasse, D. S. D. Larsson, L. H. Gunn, M. Svenda, A. Munke, J. A. Sellberg, *et al.*, "Electrospray sample injection for single-particle imaging with x-ray lasers," *Science Advances*, vol. 5, no. 5, p. eaav8801, 2019.
- [168] H. T. Philipp, K. Ayyer, M. W. Tate, V. Elser, and S. M. Gruner, "Solving structure with sparse, randomly-oriented x-ray data," *Optics express*, vol. 20, no. 12, pp. 13129–13137, 2012.
- [169] K. Giewekemeyer, A. Aquila, N.-T. Loh, Y. Chushkin, K. Shanks, J. Weiss, M. Tate, H. Philipp, S. Stern, P. Vagovic, et al., "Experimental 3d coherent

- diffractive imaging from photon-sparse random projections," *IUCrJ*, vol. 6, no. 3, pp. 357–365, 2019.
- [170] B. J. Daurer, K. Okamoto, J. Bielecki, F. R. N. C. Maia, K. Mühlig, M. M. Seibert, M. F. Hantke, C. Nettelblad, W. H. Benner, M. Svenda, *et al.*, "Experimental strategies for imaging bioparticles with femtosecond hard X-ray pulses," *IUCrJ*, vol. 4, pp. 251–262, May 2017.
- [171] E. D. Zhong, T. Bepler, B. Berger, and J. H. Davis, "Cryodrgn: reconstruction of heterogeneous cryo-em structures using neural networks," *Nature methods*, vol. 18, no. 2, pp. 176–185, 2021.
- [172] C.-Z. Ni, R. Syed, R. Kodandapani, J. Wickersham, D. S. Peabody, and K. R. Ely, "Crystal structure of the ms2 coat protein dimer: implications for rna binding and virus assembly," *Structure*, vol. 3, no. 3, pp. 255–263, 1995.
- [173] M. R. Perkett, D. T. Mirijanian, and M. F. Hagan, "The allosteric switching mechanism in bacteriophage ms2," *The Journal of chemical physics*, vol. 145, no. 3, 2016.
- [174] T. W. Knapman, V. L. Morton, N. J. Stonehouse, P. G. Stockley, and A. E. Ashcroft, "Determining the topology of virus assembly intermediates using ion mobility spectrometry–mass spectrometry," *Rapid communications in mass spectrometry*, vol. 24, no. 20, pp. 3033–3042, 2010.
- [175] S. Tamara, M. A. den Boer, and A. J. R. Heck, "High-resolution native mass spectrometry," *Chemical Reviews*, vol. 122, no. 8, pp. 7269–7326, 2022. PMID: 34415162.
- [176] T. V. Yenupuri, S. Rafie-Zinedine, L. Worbs, M. Heymann, J. Schulz, J. Bielecki, and F. R. Maia, "Helium-electrospray improves sample delivery in x-ray single-particle imaging experiments," *Scientific Reports*, vol. 14, no. 1, p. 4401, 2024.
- [177] E. Sobolev, S. Zolotarev, K. Giewekemeyer, J. Bielecki, K. Okamoto, H. K. Reddy, J. Andreasson, K. Ayyer, I. Barak, S. Bari, *et al.*, "Megahertz single-particle imaging at the european xfel," *Communications Physics*, vol. 3, no. 1, pp. 1–11, 2020.
- [178] C. H. Yoon, P. Schwander, C. Abergel, I. Andersson, J. Andreasson, A. Aquila, S. Bajt, M. Barthelmess, A. Barty, M. J. Bogan, et al., "Unsupervised classifica-

- tion of single-particle x-ray diffraction snapshots by spectral clustering," *Opt. Express*, vol. 19, pp. 16542–16549, Aug 2011.
- [179] J. R. Fienup, "Reconstruction of an object from the modulus of its fourier transform," *Optics letters*, vol. 3, no. 1, pp. 27–29, 1978.
- [180] I. V. Lundholm, J. A. Sellberg, T. Ekeberg, M. F. Hantke, K. Okamoto, G. van der Schot, J. Andreasson, A. Barty, J. Bielecki, P. Bruza, *et al.*, "Considerations for three-dimensional image reconstruction from experimental data in coherent diffractive imaging," *IUCrJ*, vol. 5, pp. 531–541, Sep 2018.
- [181] R. G. Sierra, H. Laksmono, J. Kern, R. Tran, J. Hattne, R. Alonso-Mori, B. Lassalle-Kaiser, C. Glöckner, J. Hellmich, D. W. Schafer, *et al.*, "Nanoflow electrospinning serial femtosecond crystallography," *Acta Crystallographica Section D*, vol. 68, pp. 1584–1587, Nov 2012.
- [182] M. S. Hunter, B. Segelke, M. Messerschmidt, G. J. Williams, N. A. Zatsepin, A. Barty, W. H. Benner, D. B. Carlson, M. Coleman, A. Graf, *et al.*, "Fixed-target protein serial microcrystallography with an x-ray free electron laser," *Scientific reports*, vol. 4, p. 6026, 2014.
- [183] D. Nam, C. Kim, Y. Kim, T. Ebisu, M. Gallagher-Jones, J. Park, S. Kim, S. Kim, K. Tono, M. Yabashi, T. Ishikawa, and C. Song, "Fixed target single-shot imaging of nanostructures using thin solid membranes at sacla," *Journal of Physics B: Atomic, Molecular and Optical Physics*, vol. 49, no. 3, p. 034008, 2016.
- [184] C. Seuring, K. Ayyer, E. Filippaki, M. Barthelmess, J.-N. Longchamp, P. Ringler, T. Pardini, D. H. Wojtas, M. A. Coleman, K. Dörner, *et al.*, "Femtosecond x-ray coherent diffraction of aligned amyloid fibrils on low background graphene," *Nature Communications*, vol. 9, no. 1, p. 1836, 2018.
- [185] W. Decking, S. Abeghyan, P. Abramian, A. Abramsky, A. Aguirre, C. Albrecht, P. Alou, M. Altarelli, P. Altmann, K. Amyan, V. Anashin, M. Mommerz, L. Monaco, C. Montiel, M. Moretti, I. Morozov, P. Morozov, D. Mross, *et al.*, "A mhz-repetition-rate hard x-ray free-electron laser driven by a superconducting linear accelerator," *Nature Photonics*, pp. 391–397, May 2020.
- [186] S. Gravel and V. Elser, "Divide and concur: A general approach to constraint satisfaction," *Physical Review E*, vol. 78, no. 3, p. 036706, 2008.

- [187] V. Torczon, "On the convergence of pattern search algorithms," *SIAM Journal on optimization*, vol. 7, no. 1, pp. 1–25, 1997.
- [188] A. V. Martin, N. Loh, C. Y. Hampton, R. G. Sierra, F. Wang, A. Aquila, S. Bajt, M. Barthelmess, C. Bostedt, J. D. Bozek, et al., "Femtosecond dark-field imaging with an x-ray free electron laser," *Optics express*, vol. 20, no. 12, pp. 13501– 13512, 2012.
- [189] A. Nasir and G. Caetano-Anollés, "A phylogenomic data-driven exploration of viral origins and evolution," *Science advances*, vol. 1, no. 8, p. e1500527, 2015.
- [190] S. Srihari, C. H. Yong, A. Patil, and L. Wong, "Methods for protein complex prediction and their contributions towards understanding the organisation, function and dynamics of complexes," *FEBS letters*, vol. 589, no. 19, pp. 2590–2602, 2015.
- [191] W. F. Dean and A. L. Mattheyses, "Illuminating cellular architecture and dynamics with fluorescence polarization microscopy," *Journal of Cell Science*, vol. 137, no. 20, 2024.
- [192] H. N. Chapman, C. Caleman, and N. Timneanu, "Diffraction before destruction," *Philosophical Transactions of the Royal Society B: Biological Sciences*, vol. 369, no. 1647, p. 20130313, 2014.
- [193] R. Neutze and J. Hajdu, "Femtosecond time resolution in x-ray diffraction experiments," *Proceedings of the National Academy of Sciences*, vol. 94, no. 11, pp. 5651–5655, 1997.
- [194] S. Dold, T. Reichenbach, A. Colombo, J. Jordan, I. Barke, P. Behrens, N. Bernhardt, J. Correa, S. Düsterer, B. Erk, *et al.*, "Melting, bubblelike expansion, and explosion of superheated plasmonic nanoparticles," *Physical Review Letters*, vol. 134, no. 13, p. 136101, 2025.
- [195] F.-Z. Zhao, B. Zhang, E.-K. Yan, B. Sun, Z.-J. Wang, J.-H. He, and D.-C. Yin, "A guide to sample delivery systems for serial crystallography," *The FEBS Journal*, vol. 286, no. 22, pp. 4402–4417, 2019.
- [196] T. You, J. Bielecki, and F. R. Maia, "Impact of gas background on xfel single-particle imaging," *arXiv preprint arXiv:2411.16259*, 2024.

- [197] J. Helliwell, "Synchrotron radiation and crystallography: the first 50 years," *Acta Crystallographica Section A: Foundations of Crystallography*, vol. 54, no. 6, pp. 738–749, 1998.
- [198] R. Neutze and K. Moffat, "Time-resolved structural studies at synchrotrons and x-ray free electron lasers: opportunities and challenges," *Current opinion in structural biology*, vol. 22, no. 5, pp. 651–659, 2012.
- [199] R. Khubbutdinov, A. Menushenkov, and I. Vartanyants, "Coherence properties of the high-energy fourth-generation x-ray synchrotron sources," *Synchrotron Radiation*, vol. 26, no. 6, pp. 1851–1862, 2019.
- [200] M. Stransky, Z. Shen, Z. Jurek, C. Fortmann-Grote, R. Bean, R. Santra, B. Ziaja, A. P. Mancuso, *et al.*, "Water layer and radiation damage effects on the orientation recovery of proteins in single-particle imaging at an x-ray free-electron laser," *Scientific reports*, vol. 13, no. 1, pp. 1–11, 2023.
- [201] Y. Chushkin and F. Zontone, "Prospects for coherent x-ray diffraction imaging at fourth-generation synchrotron sources," *IUCrJ*, vol. 12, no. 3, 2025.
- [202] N. Vogel, M. Retsch, C.-A. Fustin, A. del Campo, and U. Jonas, "Advances in colloidal assembly: the design of structure and hierarchy in two and three dimensions," *Chemical reviews*, vol. 115, no. 13, pp. 6265–6311, 2015.
- [203] X. Ye, J. Huang, Y. Zeng, L.-X. Sun, F. Geng, H.-J. Liu, F.-R. Wang, X.-D. Jiang, W.-D. Wu, and W.-G. Zheng, "Monolayer colloidal crystals by modified air-water interface self-assembly approach," *Nanomaterials*, vol. 7, no. 10, p. 291, 2017.
- [204] C. Crowe-McAuliffe, V. Murina, K. J. Turnbull, M. Kasari, M. Mohamad, C. Polte, H. Takada, K. Vaitkevicius, J. Johansson, Z. Ignatova, *et al.*, "Structural basis of abcf-mediated resistance to pleuromutilin, lincosamide, and streptogramin a antibiotics in gram-positive pathogens," *Nature Communications*, vol. 12, no. 1, p. 3577, 2021.
- [205] P. Thibault, M. Dierolf, O. Bunk, A. Menzel, and F. Pfeiffer, "Probe retrieval in ptychographic coherent diffractive imaging," *Ultramicroscopy*, vol. 109, no. 4, pp. 338–343, 2009.
- [206] T. Li, A. J. Senesi, and B. Lee, "Small angle x-ray scattering for nanoparticle research," *Chemical reviews*, vol. 116, no. 18, pp. 11128–11180, 2016.

- [207] A. Taylor, Motheye Smart Windows: Bio-inspired, temperature-responsive glazing for passive regulation of building temperature with the ability to self-clean. PhD thesis, UCL (University College London), 2017.
- [208] E. Sirotkin, J. D. Apweiler, and F. Y. Ogrin, "Macroscopic ordering of polystyrene carboxylate-modified nanospheres self-assembled at the waterair interface," *Langmuir*, vol. 26, no. 13, pp. 10677–10683, 2010.
- [209] X. Ye and L. Qi, "Recent advances in fabrication of monolayer colloidal crystals and their inverse replicas," *Science China Chemistry*, vol. 57, pp. 58–69, 2014.
- [210] A. K. S. Kumar, Y. Zhang, D. Li, and R. G. Compton, "A mini-review: How reliable is the drop casting technique?," *Electrochemistry Communications*, vol. 121, p. 106867, 2020.
- [211] S. Huang, K. Minami, H. Sakaue, S. Shingubara, and T. Takahagi, "Effects of the surface pressure on the formation of langmuir- blodgett monolayer of nanoparticles," *Langmuir*, vol. 20, no. 6, pp. 2274–2276, 2004.
- [212] A. Chandramohan, N. V. Sibirev, V. G. Dubrovskii, M. C. Petty, A. J. Gallant, and D. A. Zeze, "Model for large-area monolayer coverage of polystyrene nanospheres by spin coating," *Scientific reports*, vol. 7, no. 1, p. 40888, 2017.
- [213] J. N. Galayda *et al.*, "The lcls-ii project," *Proceedings of IPAC*, vol. 2014, p. 935, 2014.
- [214] C. G. Schroer, I. Agapov, W. Brefeld, R. Brinkmann, Y.-C. Chae, H.-C. Chao, M. Eriksson, J. Keil, X. Nuel Gavaldà, R. Röhlsberger, *et al.*, "Petra iv: the ultralow-emittance source project at desy," *Synchrotron Radiation*, vol. 25, no. 5, pp. 1277–1290, 2018.
- [215] P. Plevka, K. Tars, and L. Liljas, "Structure and stability of icosahedral particles of a covalent coat protein dimer of bacteriophage ms2," *Protein Science*, vol. 18, no. 8, pp. 1653–1661, 2009.
- [216] D. S. Peabody and F. Lim, "Complementation of rna binding site mutations in ms2 coat protein heterodimers," *Nucleic acids research*, vol. 24, no. 12, pp. 2352–2359, 1996.
- [217] E. F. Pettersen, T. D. Goddard, C. C. Huang, G. S. Couch, D. M. Greenblatt, E. C. Meng, and T. E. Ferrin, "Ucsf chimera—a visualization system for exploratory

- research and analysis," *Journal of computational chemistry*, vol. 25, no. 13, pp. 1605–1612, 2004.
- [218] D. P. Kingma and J. Ba, "Adam: A method for stochastic optimization," *arXiv* preprint arXiv:1412.6980, 2014.
- [219] Lindahl, Abraham, Hess, and van der Spoel, "Gromacs 2020.7 manual," Feb. 2022.